



HAL
open science

Vertex dynamics simulations of subgrain growth in Al-Mn binary alloys : Effect of crystallographic orientation

Adish Majumdar

► **To cite this version:**

Adish Majumdar. Vertex dynamics simulations of subgrain growth in Al-Mn binary alloys : Effect of crystallographic orientation. Other. Ecole Nationale Supérieure des Mines de Saint-Etienne, 2013. English. NNT : 2013EMSE0689 . tel-00862402

HAL Id: tel-00862402

<https://theses.hal.science/tel-00862402>

Submitted on 16 Sep 2013

HAL is a multi-disciplinary open access archive for the deposit and dissemination of scientific research documents, whether they are published or not. The documents may come from teaching and research institutions in France or abroad, or from public or private research centers.

L'archive ouverte pluridisciplinaire **HAL**, est destinée au dépôt et à la diffusion de documents scientifiques de niveau recherche, publiés ou non, émanant des établissements d'enseignement et de recherche français ou étrangers, des laboratoires publics ou privés.

NNT : 2013 EMSE 0689

THÈSE

présentée par

Adhish MAJUMDAR

pour obtenir le grade de

Docteur de l'École Nationale Supérieure des Mines de Saint-Étienne

Spécialité : Sciences et Génie des Matériaux

VERTEX DYNAMICS SIMULATIONS OF SUBGRAIN GROWTH IN
AL-0.1%MN BINARY ALLOYS : EFFECT OF CRYSTALLOGRAPHIC
ORIENTATION

soutenue à Saint-Etienne, le 16 mai 2013

Membres du jury

Président :	Claude ESLING	Professeur, Université de Lorraine, Metz
Rapporteurs :	Anne-Laure HELBERT	Maître de Conférence, Université Paris-Sud XI
	Roland LOGE	Chargé de Recherche, Mines ParisTech
Examineur :	Indradev SAMAJDAR	Professeur, IIT Bombay, Mumbai, Inde
Directeurs de thèse :	Julian DRIVER	Directeur de Recherche, ENSM-SE
	Claire MAURICE	Chargée de Recherche, ENSM-SE

Spécialités doctorales :
 SCIENCES ET GENIE DES MATERIAUX
 MECANIQUE ET INGENIERIE
 GENIE DES PROCEDES
 SCIENCES DE LA TERRE
 SCIENCES ET GENIE DE L'ENVIRONNEMENT
 MATHEMATIQUES APPLIQUEES
 INFORMATIQUE
 IMAGE, VISION, SIGNAL
 GENIE INDUSTRIEL
 MICROELECTRONIQUE

Responsables :
 K. Wolski Directeur de recherche
 S. Drapier, professeur
 F. Gruy, Maître de recherche
 B. Guy, Directeur de recherche
 D. Graillot, Directeur de recherche
 O. Roustant, Maître-assistant
 O. Boissier, Professeur
 J.C. Pinoli, Professeur
 A. Dolgui, Professeur

EMSE : Enseignants-chercheurs et chercheurs autorisés à diriger des thèses de doctorat (titulaires d'un doctorat d'État ou d'une HDR)

AVRIL	Stéphane	PR2	Mécanique et ingénierie	CIS
BATTON-HUBERT	Mireille	PR2	Sciences et génie de l'environnement	FAYOL
BENABEN	Patrick	PR1	Sciences et génie des matériaux	CMP
BERNACHE-ASSOLLANT	Didier	PR0	Génie des Procédés	CIS
BIGOT	Jean Pierre	MR(DR2)	Génie des Procédés	SPIN
BILAL	Essaid	DR	Sciences de la Terre	SPIN
BOISSIER	Olivier	PR1	Informatique	FAYOL
BORBELY	Andras	MR(DR2)	Sciences et génie de l'environnement	SMS
BOUCHER	Xavier	PR2	Génie Industriel	FAYOL
BRODHAG	Christian	DR	Sciences et génie de l'environnement	FAYOL
BURLAT	Patrick	PR2	Génie Industriel	FAYOL
COLLOT	Philippe	PR0	Microélectronique	CMP
COURNIL	Michel	PR0	Génie des Procédés	DIR
DARRIEULAT	Michel	IGM	Sciences et génie des matériaux	SMS
DAUZERE-PERES	Stéphane	PR1	Génie Industriel	CMP
DEBAYLE	Johan	CR	Image Vision Signal	CIS
DELAFOSSÉ	David	PR1	Sciences et génie des matériaux	SMS
DESRAYAUD	Christophe	PR2	Mécanique et ingénierie	SMS
DOLGUI	Alexandre	PR0	Génie Industriel	FAYOL
DRAPIER	Sylvain	PR1	Mécanique et ingénierie	SMS
FEILLET	Dominique	PR2	Génie Industriel	CMP
FOREST	Bernard	PR1	Sciences et génie des matériaux	CIS
FORMISYN	Pascal	PR0	Sciences et génie de l'environnement	DIR
FRACZKIEWICZ	Anna	DR	Sciences et génie des matériaux	SMS
GARCIA	Daniel	MR(DR2)	Génie des Procédés	SPIN
GERINGER	Jean	MA(MDC)	Sciences et génie des matériaux	CIS
GIRARDOT	Jean-jacques	MR(DR2)	Informatique	FAYOL
GOEURIOT	Dominique	DR	Sciences et génie des matériaux	SMS
GRAILLOT	Didier	DR	Sciences et génie de l'environnement	SPIN
GROSSEAU	Philippe	DR	Génie des Procédés	SPIN
GRUY	Frédéric	PR1	Génie des Procédés	SPIN
GUY	Bernard	DR	Sciences de la Terre	SPIN
GUYONNET	René	DR	Génie des Procédés	SPIN
HAN	Woo-Suck	CR	Mécanique et ingénierie	SMS
HERRI	Jean Michel	PR1	Génie des Procédés	SPIN
INAL	Karim	PR2	Microélectronique	CMP
KLOCKER	Helmut	DR	Sciences et génie des matériaux	SMS
LAFOREST	Valérie	MR(DR2)	Sciences et génie de l'environnement	FAYOL
LERICHE	Rodolphe	CR	Mécanique et ingénierie	FAYOL
LI	Jean Michel		Microélectronique	CMP
MALLIARAS	Georges	PR1	Microélectronique	CMP
MOLIMARD	Jérôme	PR2	Mécanique et ingénierie	CIS
MONTHEILLET	Franck	DR	Sciences et génie des matériaux	SMS
PERIER-CAMBY	Laurent	PR2	Génie des Procédés	DFG
PIJOLAT	Christophe	PR0	Génie des Procédés	SPIN
PIJOLAT	Michèle	PR1	Génie des Procédés	SPIN
PINOLI	Jean Charles	PR0	Image Vision Signal	CIS
POURCHEZ	Jérémy	CR	Génie des Procédés	CIS
ROUSTANT	Olivier	MA(MDC)		FAYOL
STOLARZ	Jacques	CR	Sciences et génie des matériaux	SMS
SZAFNICKI	Konrad	MR(DR2)	Sciences et génie de l'environnement	CMP
TRIA	Assia		Microélectronique	CMP
VALDIVIESO	François	MA(MDC)	Sciences et génie des matériaux	SMS
VIRICELLE	Jean Paul	MR(DR2)	Génie des Procédés	SPIN
WOLSKI	Krzystof	DR	Sciences et génie des matériaux	SMS
XIE	Xiaolan	PR1	Informatique	CIS

ENISE : Enseignants-chercheurs et chercheurs autorisés à diriger des thèses de doctorat (titulaires d'un doctorat d'État ou d'une HDR)

FORTUNIER	Roland	PR	Sciences et Génie des matériaux	ENISE
BERGHEAU	Jean-Michel	PU	Mécanique et Ingénierie	ENISE
DUBUJET	Philippe	PU	Mécanique et Ingénierie	ENISE
LYONNET	Patrick	PU	Mécanique et Ingénierie	ENISE
SMUROV	Igor	PU	Mécanique et Ingénierie	ENISE
ZAHOUANI	Hassan	PU	Mécanique et Ingénierie	ENISE
BERTRAND	Philippe	MCF	Génie des procédés	ENISE
HAMDI	Hédi	MCF	Mécanique et Ingénierie	ENISE
KERMOUCHE	Guillaume	MCF	Mécanique et Ingénierie	ENISE
RECH	Joël	MCF	Mécanique et Ingénierie	ENISE
TOSCANO	Rosario	MCF	Mécanique et Ingénierie	ENISE
GUSSAROV	Andrey	Enseignant contractuel	Génie des procédés	ENISE

PR 0	Professeur classe exceptionnelle	Ing.	Ingénieur
PR 1	Professeur 1 ^{ère} classe	MCF	Maître de conférences
PR 2	Professeur 2 ^{ème} classe	MR (DR2)	Maître de recherche
PU	Professeur des Universités	CR	Chargé de recherche
MA (MDC)	Maître assistant	EC	Enseignant-chercheur
DR	Directeur de recherche	IGM	Ingénieur général des mines

SMS	Sciences des Matériaux et des Structures
SPIN	Sciences des Processus Industriels et Naturels
FAYOL	Institut Henri Fayol
CMP	Centre de Microélectronique de Provence
CIS	Centre Ingénierie et Santé

Vertex dynamics simulations of subgrain growth in Al-0.1%Mn binary alloys: Effect of crystallographic orientation



Adhish Majumdar

Centre SMS, CNRS UMR 5307

École Nationale Supérieure des Mines de Saint-Étienne
158 Cours Fauriel, 42023 Saint-Étienne Cedex 2, France

2013

Acknowledgements

First and foremost, I would like to thank my thesis advisors, Julian Driver and Claire Maurice, for their support and encouragement, and the great degree of independence that I experienced during the last three years. This PhD thesis was financed by the Indo-French Centre for the Promotion of Advanced Research (IFCPAR), and I worked at the Centre SMS of École de Mines de Saint-Étienne. I am grateful to both these organizations for providing me with the means to carry out this work.

I would like to thank the members of the thesis committee: Anne-Laure Helbert and Roland Logé for having taken the time to review the manuscript, Claude Esling for having presided the jury, and Indradev Samajdar for his interest in my work and for having traveled so far to attend the thesis defense.

I am grateful to Romain Quey for developing and sharing freely tools such as `Orilib` and `Hermes` which made some parts of my work easier to do. Thanks to Gilles Blanc, Claire Roume and Yoann Garnier, I was able to carry out my experiments, and also to Marilyne Mondon and Sergio São-João for helping me work with the scanning electron microscope.

The years I have spent here in Saint-Étienne were rendered very enjoyable by the company of colleagues, especially the corridor K4 where no moment is ever dull thanks to all the PhD students. Special thanks to my close friends Jean-Baptiste Frühauf, My Thu Tran, Flavien Vucko, Ramin Abbasi, Vincent Gaspard, Alix Vancostenoble, John Wise, Adam Sochacki, Akira Sato and Karolina Maminska for their friendship and company for the many trips we took together. I will never forget the enjoyable moments passed with past PhD students: skiing and via ferrata with Alban Guillotin, games of chess and checkers and long walks in the woods with Adrien Chapuis, and

wandering through the streets of Bordeaux and Lyon with Adeline Albou and Quentin Contrefois. I also thank and ask the forgiveness of those whom I may have omitted.

The members of the Dzięcioł family - Krzysztof, Aleksandra and Emilia - occupy a special place in my heart. Their friendship has been a constant source of support and encouragement for me. They have been my family during my life in Saint-Étienne. I will always cherish the memories of the time I have spent with them.

Lastly, I sincerely thank my parents and my sister for their love and guidance through all the ups and downs of my life. I have them to thank for all that is good in me.

Adhish Majumdar

Contents

List of Figures	ix
List of Tables	xv
Introduction	1
1 Bibliography	5
1.1 Recovery	5
1.1.1 Phenomenon	5
1.1.1.1 Deformation	5
1.1.1.2 Stored energy	6
1.1.1.3 Mechanisms	7
1.1.2 Experimental studies	9
1.1.2.1 Mechanical properties	9
1.1.2.2 Microstructure evolution with recovery	11
1.1.2.3 Recovery in deformed single crystals	13
1.1.3 Modelling recovery kinetics	16
1.1.3.1 Generic kinetic laws	16
1.1.3.2 Analytic kinetic laws	19
1.2 Simulations of grain growth	20
1.2.1 Vertex dynamics simulations	20
1.2.1.1 Introduction	20
1.2.1.2 Brief description	21
1.2.1.3 Application	21
1.2.2 Monte Carlo Potts model	23
1.2.2.1 Introduction	23

CONTENTS

1.2.2.2	Application	25
1.2.3	Phase-field models	25
1.2.3.1	Introduction	25
1.2.3.2	Application	27
1.2.4	Comparison between different models	27
1.3	Objectives of the thesis	29
2	Vertex dynamics simulations	31
2.1	Introduction	31
2.2	Microstructure generation using Voronoi tessellation	31
2.2.1	Definition	31
2.2.2	Program <code>voronoi2d</code>	32
2.3	Principles of the vertex dynamics simulations	34
2.3.1	History	34
2.3.2	Program <code>networkConsole</code>	34
2.3.3	Velocity of vertices	36
2.3.3.1	Geometry	38
2.3.3.2	Energy of subgrain boundaries	39
2.3.3.3	Mobility of subgrain boundaries	40
2.3.4	Topological transformations	42
2.3.5	Time increment	43
2.3.5.1	Global time increment	43
2.3.5.2	<i>Fast</i> vertices	44
2.3.5.3	Relationship between the Global and Fast time increments	45
2.4	Validation	45
2.4.1	Shrinking polygon	45
2.4.2	Von Neumann-Mullins law	47
2.4.3	Scaling behaviour	49
2.4.4	Microstructure	49
2.5	Adapting for subgrain boundaries	49
2.5.1	<i>Fast</i> treatment	49

3	Experimental Techniques	53
3.1	Material	53
3.2	Thermomechanical treatment	54
3.2.1	Deformation by cold rolling	55
3.2.2	Annealing	55
3.3	Characterization	56
3.3.1	Sample preparation	56
3.3.2	Microhardness	56
3.3.3	EBSD mapping	58
4	Kinetics of recovery	61
4.1	Introduction	61
4.2	Microstructural evolution during annealing	62
4.2.1	EBSD mapping	62
4.2.2	Microhardness	63
4.3	Activation energy for recovery	67
4.3.1	Analysis method	67
4.3.1.1	Model equations	67
4.3.1.2	Removal of noise from experimental data	68
4.3.1.3	Evaluating the stored energy and activation energy	70
4.3.2	Results	71
4.3.2.1	Activation energy	71
4.3.2.2	Stored energy	74
4.4	Discussion	75
4.5	Conclusions	78
5	Simulation of subgrain growth	81
5.1	Introduction	81
5.2	Material properties	82
5.3	Deformation microstructures	84
5.3.1	Experimental results	84
5.3.2	Crystal plasticity	86
5.3.3	Input microstructures for the vertex dynamics simulations	87
5.3.3.1	Parameters for generating input microstructures	87

CONTENTS

5.3.3.2	Colour-coded representation of orientations	87
5.3.3.3	Brass orientation	88
5.3.3.4	Goss orientation	88
5.4	Influence of crystallographic orientation on recovery	90
5.4.1	Brass orientation	90
5.4.2	Goss orientation	90
5.5	Discussion	95
5.5.1	Rates of recovery in Brass and Goss oriented crystals	95
5.5.2	Activation energy	98
5.5.3	Recovery kinetics	99
5.6	Conclusions	102
6	Conclusions	103
6.1	Summary	103
6.2	Scope of future work	107
6.2.1	Microstructure	107
6.2.2	Alternative mobility and energy laws	107
6.2.3	Parallel computing	108
6.2.4	Kinetics of recovery	108
	Appendices	109
A	Data Structures	111
A.1	Vertex	111
A.2	Segment	112
A.3	Grain Boundary	113
A.4	List of grain boundaries	114
A.5	Grain	115
A.6	Master class for the simulation	115
B	Topological transformations	119
B.1	Introduction	119
B.2	Checking for topological transformations	119
B.2.1	Marking grain boundaries for topological transformations	120
B.2.2	Identifying the topological transformations	120

CONTENTS

B.3 Removal of a lenticular grain	121
B.4 Removal of a triangular grain	122
B.5 Recombination of triple points	123
References	125

CONTENTS

List of Figures

1.1	Rearrangement of dislocations in a deformed metal during recovery . . .	8
1.2	Softening as a function of time of deformed Al-Mg alloys after storage at room temperature	10
1.3	Transmission electron microscopy (TEM) of aluminium deformed 10% and annealed in-situ (a) as-deformed and (b) annealed for 2 minutes at 250°C	11
1.4	EBSD map representing disorientations greater than 15° in black and disorientations greater than (a) 0.5° and (b) 1.5° in grey	12
1.5	Microstructure resulting from Subgrain Reconstruction Mapping (SRM) with subgrain boundaries detected and closed subgrains	13
1.6	True stress-true strain curves of the deformation up to a true strain of 2.3 of Al-0.1%Mn monocrystals by plane strain compression	14
1.7	Fractional residual strain hardening as a function of time in Brass, Goss and S oriented crystals deformed in plane strain compression to a true strain of 2.3 and then annealed at 264°C	15
1.8	Time evolution of microstructure of deformed Al-0.1%Mn crystals an- nealed at 264°C for 34 hours	15
1.9	Isothermal recovery kinetics modeled using the equation proposed by Vandermeer and Hansen	18
1.10	Different types of models to simulate grain growth	21
1.11	Result of a vertex dynamics simulation in three dimensions using the finite element method showing the pinning of a migrating grain boundary by particles	22

LIST OF FIGURES

1.12	Growing and shrinking grains in a three-dimensional vertex dynamics simulation	23
1.13	Vertex dynamics simulation of grain growth in Damascene interconnects used in microelectronic devices	24
1.14	(a) Zener pinning simulation using Monte Carlo Potts model (b) Simulation of recrystallization with isotropic (top) and anisotropic (bottom) grain boundary energies	26
1.15	Phase-field simulation of grain growth	28
2.1	Schematic representation of Voronoi Tessellation using Delaunay triangulation	33
2.2	Microstructure generated using <code>voronoi2d</code> with 5000 domains and a mean radius of 5 μm	35
2.3	Flowchart of the program <code>networkConsole</code> to carry out vertex dynamics simulations in two dimensions	37
2.4	Connections of vertices - (a) Real vertex with 3 connections and (b) Virtual vertex with 2 connections	38
2.5	Subgrain boundary energy as a function of disorientation angle, evaluated using the Read-Shockley expression	39
2.6	Grain boundary mobility as a function of disorientation.	41
2.7	Mobility of boundaries as a function of disorientation with modified expression for low disorientation angles	42
2.8	Topological transformations (a) Recombination of two triple points, (b) disappearance of a triangular grain and (c) disappearance of a lenticular grain	43
2.9	Rate of decrease of area in simulations compared with the analytic solution	46
2.10	(a) Shrinking 15-sided isolated polygon (b) Reduction of area with time for the 15-sided isolated polygon	46
2.11	Growth of a 9-sided regular polygon embedded in a frozen microstructure: (a) Initial shape (b) Shape after 150 iterations	47
2.12	Rate of increase of area of the 9-sided polygon shown in Figure 2.11	48
2.13	Von Neumann-Mullins law is verified by the simulations for an n -sided polygon embedded in a frozen microstructure.	48

LIST OF FIGURES

2.14	Scaling behaviour of mean grain area evolution with time	50
2.15	Normal grain growth using the vertex dynamics simulation program (a) Initial microstructure generated using Voronoi Tessellation and (b) Evolved microstructure using vertex dynamics	50
3.1	Initial texture of the bars of Al-0.1% Mn model alloy	54
3.2	Schematic representation of the deformation by cold rolling	55
3.3	The sample after cold-mounting and mechanical polishing. The visible sample surface is the ND-RD face of dimensions $380 \mu\text{m} \times 25 \text{ mm}$. The steel rings are used to hold the sample upright during cold-mounting . .	57
3.4	Schematic representation of the setup for EBSD	59
3.5	An example of a Kikuchi pattern, its Hough transform, and identification of Kikuchi bands	60
4.1	EBSD map of the undeformed sample	62
4.2	EBSD map of the sample annealed for 1000 hours at 190°C	63
4.3	EBSD map of the sample annealed for 480 hours at 225°C	64
4.4	Microhardness values for annealing at (a) 130°C , (b) 160°C . The error bars represent the standard deviation of the fifteen measurements made for each point.	65
4.5	Microhardness values for annealing at (a) 190°C and (b) 225°C . The error bars represent the standard deviation of the fifteen measurements made for each point.	66
4.6	Curves (in blue) generated from values of (t, f^2) calculated from micro- hardness measurements on samples annealed at 190°C , with the points of intersection highlighted (in red)	69
4.7	Filtered data set after removal of points lying far from the cluster	70
4.8	Recovery kinetics as a function of temperature - Linear fit performed to estimate the value of the activation energy	72
4.9	Experimental data points (in red) with the model curve (in blue). The model curve is generated using the parameters t_0^{-1} and βP_0 estimated from the experimental data.	73
4.10	Estimate of activation energy for recovery using data from annealing at $130, 160$ and 190°C	74

LIST OF FIGURES

4.11	Values of β for different temperature and strain values, as presented by Vandermeer and Hansen	77
5.1	Curves representing the change in the scaling of mobility with temperature for two values of activation energy	84
5.2	Deformation microstructures in the ND-RD section in (a) Brass, (b) Goss and (c) S single crystals deformed plastically to $\epsilon = 2.3$ in plane-strain compression in a channel-die	85
5.3	Disorientation along a line, with respect to an initial point, in (a) Brass, (b) Goss and (c) S deformed structures presented in Figure 5.2	85
5.4	$\{111\}$ pole figures of orientation spreads resulting from crystal plasticity simulations of plane-strain compression up to a true strain of 2.3 for (a) Brass and (b) Goss	87
5.5	Starting microstructure for Brass oriented crystals	89
5.6	Starting microstructure for Goss oriented crystals	91
5.7	Brass microstructure after simulation of annealing at 264°C for $t = 34$ hours. No evolution is observed.	92
5.8	Goss microstructure after simulation of annealing at 264°C for $t = 4003$ s. Growth is observed in subgrains located at the interface between bands.	93
5.9	Goss microstructure after simulation of annealing at 264°C for 34 hours. Significant subgrain growth is observed. Some of the bands have grown through adjacent bands.	94
5.10	Mean subgrain area as a function of time in the Goss and Brass microstructures in the simulation of annealing at 264°C	95
5.11	Initial disorientation distributions in the Goss and Brass microstructures	96
5.12	Disorientation distributions in Goss and Brass deformation microstructures with subgrain boundary mobility as a function of subgrain boundary disorientation	97
5.13	Change in disorientation distribution in the Goss microstructure. There is a slight increase in the fraction of low angle subgrain boundaries while the fraction of higher angle boundaries reduces.	98
5.14	Mean subgrain radius in the Goss microstructure simulation plotted against time	99

LIST OF FIGURES

5.15 Mean subgrain radius in the Goss microstructure simulation plotted against time	100
5.16 Fit of the simulation data to the recovery kinetics equation by Nes . . .	101
B.1 Removing a lenticular grain using the function <code>killLozenge</code>	121
B.2 Removing a triangular grain using the function <code>killTriangle</code>	122
B.3 Recombination of triple points using the function <code>flipSegment</code>	123

LIST OF FIGURES

List of Tables

3.1	Chemical composition of Al-0.1% Mn model alloy	53
4.1	Values of βP_0 estimated from (t, f^2) curves.	71
4.2	Mean values of t_0^{-1} calculated for each annealing temperature.	71
4.3	Activation energies reported in literature for aluminium alloys	76

LIST OF TABLES

Introduction

Since the beginning of industrial production of aluminium a little over one hundred years ago, there has been a steady rise in the worldwide usage of aluminium alloys. Presently, aluminium is second to only iron in terms of global metal production. There is a wide range of applications of aluminium alloys: transportation - aircraft, automobiles; construction - windows, doors; packaging - cans, foils; household cooking utensils and many more. Packaging applications are a major field of consumption of aluminium alloys. For example, 23% of the global aluminium production in the year 2000 was used for the purposes of containers and packaging [1].

The great advantage of using aluminium over steel for the production of cans is that aluminium alloys offer resistance to corrosion due to the passive oxide layer at a lower cost, and can be formed into cans by ironing. The cans are deep-drawn from a circular section of aluminium sheet and the top is attached later. In the case of steel cans, the top is still made of aluminium, and having two different alloys in the same piece is a hurdle in terms of recycling. Aluminium is lighter than steel and despite its relatively high cost of extraction, aluminium is easier to recycle due to its lower melting point.

The alloys used in the manufacture of cans and household utensils belong to the AA3XXX series, which is the focus of the present study. The plastic deformation induced by rolling to form sheets stores energy in the metal in the form of crystalline defects. These defects are new grain and subgrain boundaries formed by the fragmentation of grains, and dislocations within the grains. All these defects result in the deformation microstructure, which depends strongly on the crystallography of the material. The material also hardens as it is deformed.

When the metal is annealed, the energy stored in the defects is released by annihilation of dislocations and by subgrain growth. This process is called recovery and leads to a softening of the metal. Recovery is a thermally activated process, i.e., it is

INTRODUCTION

strongly temperature dependent and proceeds faster at higher temperatures. This is critical for the aluminium alloys that are cold-rolled and stored in coils. This is because the temperature the metal attains due to the heat from cold-rolling is sufficient to start recovery, and the non-uniform rate of cooling in the coil leads to different mechanical properties in different parts of the coil.

The microstructure during and after recovery is also crucial for metals that are to undergo further annealing. The microstructure at the end of recovery determines the recrystallization behaviour by providing recrystallization nuclei. The distribution of subgrain and grain sizes, influences whether normal or abnormal grain growth will take place. Towards the end of recovery, it is often seen that recrystallization begins, and the two processes may be in competition at this stage.

While the evolution of mechanical properties during recovery has been widely studied and published, the research on the microstructural evolution is relatively sparse. Advances in electron microscopy - both scanning and transmission - have allowed for finer characterization of microstructures. The technique of electron back scatter diffraction (EBSD) developed over the past twenty years has made possible the characterization of crystallographic orientations within a microstructure. Barou et al. [2, 3] have developed a novel technique in combination with EBSD - Subgrain Reconstruction Mapping (SRM) - to detect subgrains, which allows for better estimation of recovery kinetics. It has been shown that the crystallographic orientation has a strong effect on the rate of recovery [4]. A very recent study by Albou et al. [5, 6] has investigated this effect in deformed single crystals of the Al-0.1% Mn model alloy representing the solid state matrix of the AA3XXX alloys. They have shown that the effect of crystallographic orientation shows itself first in the deformation microstructure and it is suggested that the different deformation microstructures lead to different rates of recovery when the samples are annealed.

Advances have also been made in the modelling of recovery. Analytical models, taking into account various quantities like subgrain size, dislocation density representing the internal state of the material, and other more macroscopic quantities such as hardness and flow stress, have been proposed. Mechanisms of recovery involving processes in the dislocation forest and subsequent coarsening of the microstructure have been forwarded based on observations made in transmission electron microscopy. On

the simulation side, however, there are relatively few advances. Considering the similarities between subgrain growth and grain growth, there is the possibility that simulation techniques normally used for grain growth may be applicable to subgrain growth as well.

The aim of the present study is to investigate the suggestion of Albou et al. regarding the effect of the deformation microstructure on the rate of recovery through vertex dynamics simulations applied to the subgrain growth that occurs during recovery. For this, a subgrain growth simulation program using vertex dynamics simulations based on the original work by Maurice et al. [7] and Weygand et al. [8] was created. Simulations of subgrain growth during annealing of samples representing those obtained in the work by Albou et al. are carried out to investigate the role of crystallographic orientation. For the simulations to represent the material of interest, it is important to use physical quantities such as boundary mobility and energy that correspond to the material. Boundary mobility is strongly temperature dependent through an exponential function involving the temperature and activation energy for recovery. The method of SRM developed by Barou et al. is effective but laborious as it involves microscopy and subsequent reconstruction of the microstructures of annealed samples. An apparently simpler method involving microhardness and the analytical recovery kinetics law proposed by Vandermeer and Hansen [9] was thus attempted to estimate the activation energy.

The present document presents a step-by-step development of the ideas described earlier. This is done in five chapters.

- Chapter 1 presents a review of current literature and the state of knowledge of recovery. The chapter focuses on three aspects of research: experimental observations and techniques, analytical models of recovery, and finally techniques used for the simulation of grain growth which may be adapted to the case of subgrain growth.
- Chapter 2 presents the vertex dynamics simulation technique that was used in the subgrain growth simulation program, validation of the equations used therein for cases solvable analytically, and special adjustments required for adapting the simulations to subgrain growth.

INTRODUCTION

- Chapter 3 describes the Al-0.1% Mn model alloy and the experimental techniques used to obtain the activation energy for recovery of the Al-0.1%Mn model alloy.
- Chapter 4 presents the results from the experiments - annealing and Vicker's microhardness measurements - and the analysis of the microhardness data using the recovery kinetics proposed by Vandermeer and Hansen in order to obtain an estimate of the activation energy for recovery.
- Chapter 5 contains the inputs to and results from the vertex dynamics simulations of subgrain growth. A comparison is made with the experimental results of Albou et al. The reasons for the difference in recovery rates are thus investigated using the simulations. Also presented are the kinetics followed in simulations of recovery in deformed single crystals and a fit is attempted with analytical models of recovery kinetics.

In the end a general conclusion of the work done and possible routes of future work are presented.

1

Bibliography

1.1 Recovery

Microstructural evolution occurring during annealing of deformed metals is of great technological importance because the strength of a polycrystalline metal is a strong function of its microstructure. The processes that occur during annealing are - in order of occurrence - recovery, recrystallization, and grain growth. They are thermally activated and result in a softening of the metal.

Annealing phenomena have been studied for a long time and yet there are gaps in the understanding of the basic mechanisms governing them, mainly due to the complex nature and large number of factors that affect them [10].

The work done during the thesis focuses on the first of these processes - recovery. Section 1.1.1 describes the phenomenon, the current theories of the mechanisms and the factors that influence it. Section 1.1.2 focuses on the experimental observations of recovery and section 1.1.3 discusses the models used in order to describe the kinetics of recovery.

1.1.1 Phenomenon

1.1.1.1 Deformation

Plastic deformation is an indispensable part of any industrial cycle that results in a metallic finished or semi-finished product. This deformation stores energy within the metal in the form of crystalline defects like dislocations, and new boundaries resulting from the fragmentation of grains which can also be thought of as collections of

1. BIBLIOGRAPHY

dislocations. The primary driving force behind recovery is the reduction of this stored energy.

1.1.1.2 Stored energy

The distortion field around a dislocation stores strain energy. The following equations represent the elastic energy E_{screw} and E_{edge} stored per unit length of screw and edge dislocations respectively [11].

$$E_{screw} = \frac{\mu b^2}{4\pi} \ln \left(\frac{R}{r_0} \right) \quad (1.1)$$

$$E_{screw} = \frac{\mu b^2}{4\pi(1-\nu)} \ln \left(\frac{R}{r_0} \right) \quad (1.2)$$

where μ is the shear modulus, b the Burgers vector, ν the Poisson's ratio, R the radius of the dislocation's distortion field and r_0 the dislocation core radius. The value of r_0 is taken as the magnitude of the Burger's vector, close to the interatomic spacing, or roughly 1 nm. R is typically equal to the size of the crystal for a crystal having only one dislocation, or if it contains several dislocations, R is equal to half of the distance between the dislocations [11]. This implies that the energy stored in the dislocations depends on the size of the crystal and on the number of dislocations present in it.

In either case, the ratio R/r_0 is very large. However, due to the logarithmic dependence, the value of the dislocation energy is not very sensitive to this ratio. Taking the ratio to be of the order of 500, the stored energy per unit length of a mixed dislocation can be reasonably approximated as

$$E_{mixed} = 0.5\mu b^2 \quad (1.3)$$

For subgrain boundaries, the surface energy is a function of the boundary disorientation (which can also be thought of as boundary dislocation density) according to the Read and Shockley equation [12].

$$\gamma = \gamma_{HAGB} \frac{\theta}{\theta_{HAGB}} \left[1 - \ln \left(\frac{\theta}{\theta_{HAGB}} \right) \right] \quad (1.4)$$

where γ is the subgrain boundary surface energy, γ_{HAGB} the high-angle grain boundary (HAGB) energy, θ the subgrain boundary disorientation and $\theta_{HAGB} = 15^\circ$ the HAGB disorientation.

The total subgrain area A in a given volume V depends on the mean diameter d of the subgrains according to equation 1.5.

$$\frac{A}{V} = \frac{\frac{1}{2}\pi d^2}{\frac{\pi}{6}d^3} = \frac{3}{d} \quad (1.5)$$

The energy stored in unit volume of a structure with mean subgrain diameter d and mean subgrain boundary energy $\langle\gamma\rangle$ is thus

$$E_{stored} = \frac{3\langle\gamma\rangle}{d} \quad (1.6)$$

1.1.1.3 Mechanisms

Annealing provides the activation energy required for the microstructural defects to start moving towards a configuration that lowers the total energy stored in the material. This configuration is reached through the following series of events:

1. Arrangement of dislocations to form cells
2. Annihilation of dislocation tangles within cells
3. Subgrain formation
4. Subgrain growth

The series is illustrated in Figure 1.1 [10]. This results in a softening of the material in a manner opposite to strain hardening during deformation.

In some cases recovery begins during deformation. When this happens, the process is termed *dynamic recovery*. For high stacking-fault energy (SFE) materials like aluminium and its alloys, the activation energies required for the migration of dislocations and subgrain boundaries are sufficiently low for recovery to begin at room temperature [13].

The two first steps, arrangement of dislocations to form cells and annihilation of dislocation tangles, often occur simultaneously [10]. Within the forest of dislocations present, those having Burgers vectors with opposite signs and located near each other annihilate each other and thus reduce the dislocation density, which in turn contributes to the reduction of stored energy. Since the numbers of dislocations having opposing Burgers vectors are not equal, there remain dislocations that are not annihilated. Of

1. BIBLIOGRAPHY

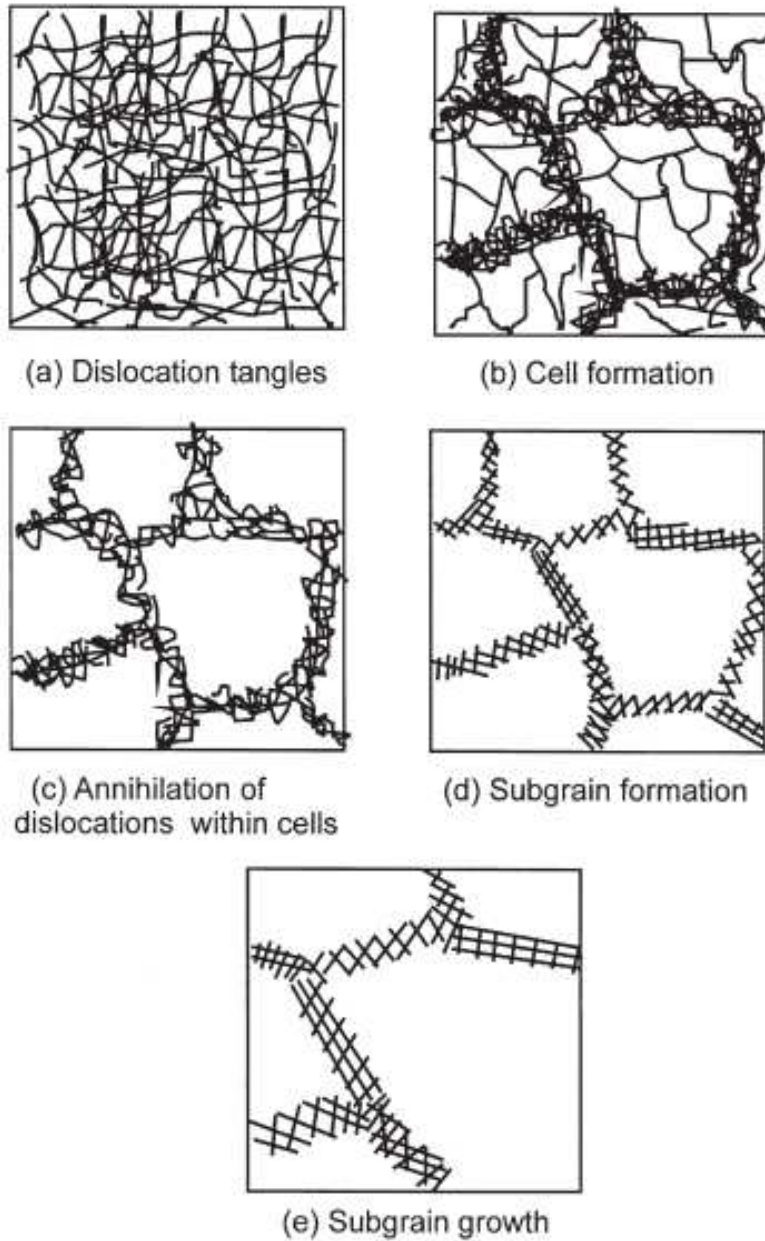


Figure 1.1: Rearrangement of dislocations in a deformed metal during recovery [10]

course, there remain other dislocations that do not form pairs. This part is illustrated in Figure 1.1(a)-(c).

As the dislocation annihilations take place, other dislocations that find themselves in the proximity of dislocations having the same Burgers vector begin arranging themselves into stable structures like low-angle boundaries (Figure 1.1(b)-(c)). A simple case of low-angle boundaries are tilt boundaries which result in the formation of polygonal subgrains.

Due to the complex nature of the dislocation network created by plastic deformation, there are still several dislocations having many different Burgers vectors that remain after the first two steps of annihilation and rearrangement of dislocations. These dislocations react with each other to form complex tangles in two dimensions and thus form a three-dimensional cell structure. As recovery proceeds, these tangled networks become more regular and finally become low-angle grain boundaries. At this point, we can say that the cells have become subgrains.

The energy stored in these structures is essentially the surface energy of the subgrain boundaries. This energy is further released by the migration of subgrain boundaries resulting in subgrain growth. The state of the microstructure towards the end of recovery affects the nucleation of recrystallization and whether or not abnormal grain growth would occur.

Due to the four processes occurring in recovery, with occasional overlap between successive processes, analysing the kinetics of recovery is not simple. Many models have been proposed, from the simpler empirical models to the more complex models that depend on detailed descriptions of the involved mechanisms. These models are discussed in section 1.1.3.

1.1.2 Experimental studies

1.1.2.1 Mechanical properties

The most obvious symptom of recovery is the loss of mechanical properties such as hardness and yield strength. Thus, before the development of advanced electron microscopy systems, recovery was mainly characterized by measurements of microhardness, in addition to microstructural features like grain or subgrain size to the extent observable by microscopy.

1. BIBLIOGRAPHY

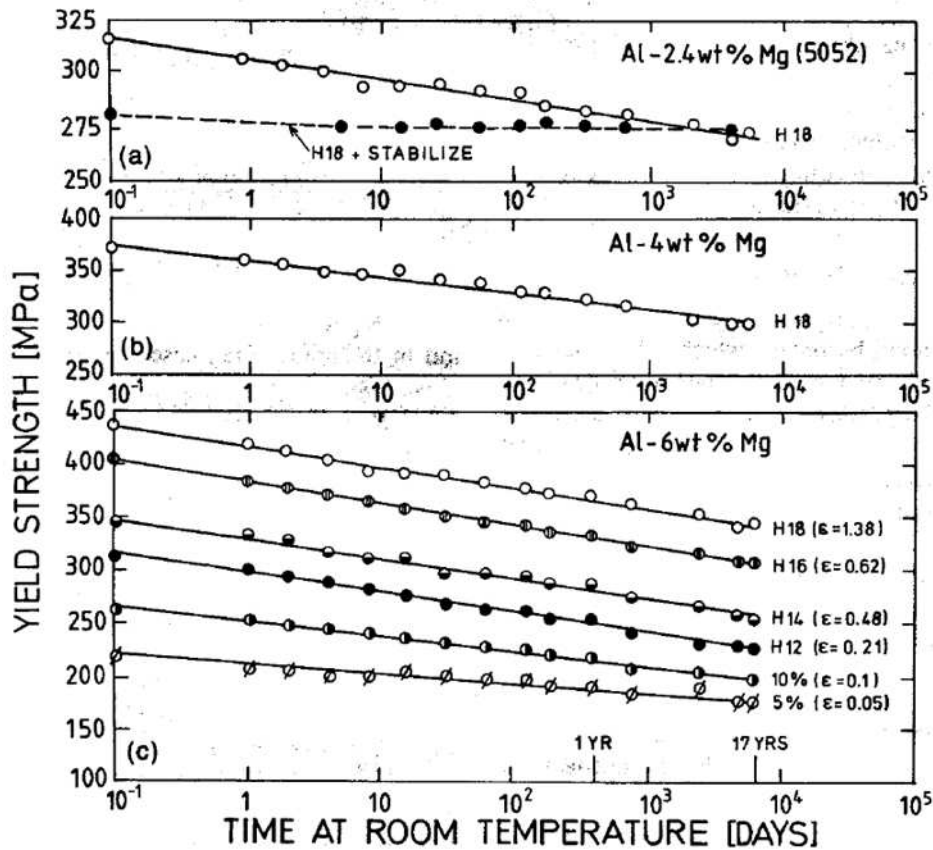


Figure 1.2: Softening as a function of time of deformed Al-Mg alloys after storage at room temperature [13]

In nearly all the experiments, a metallic sample is deformed, most commonly by rolling, and subsequently it is subjected to isothermal annealing, during which the hardness or yield stress of the samples is measured at intervals to provide a trend of the softening as a function of time and temperature. In the case of high SFE metals like aluminium and aluminium alloys, recovery has been observed to proceed even at ambient temperatures.

The review article by Nes [13] presents several examples of the softening of deformed aluminium alloys when they are subjected to annealing, and even storage at room temperature. Figure 1.2 shows one of the examples exhibiting the logarithmic decay of yield strength over a period of 17 years in samples of Al-Mg maintained at room temperature.

Mechanical properties like hardness and other quantities that affect it, like subgrain

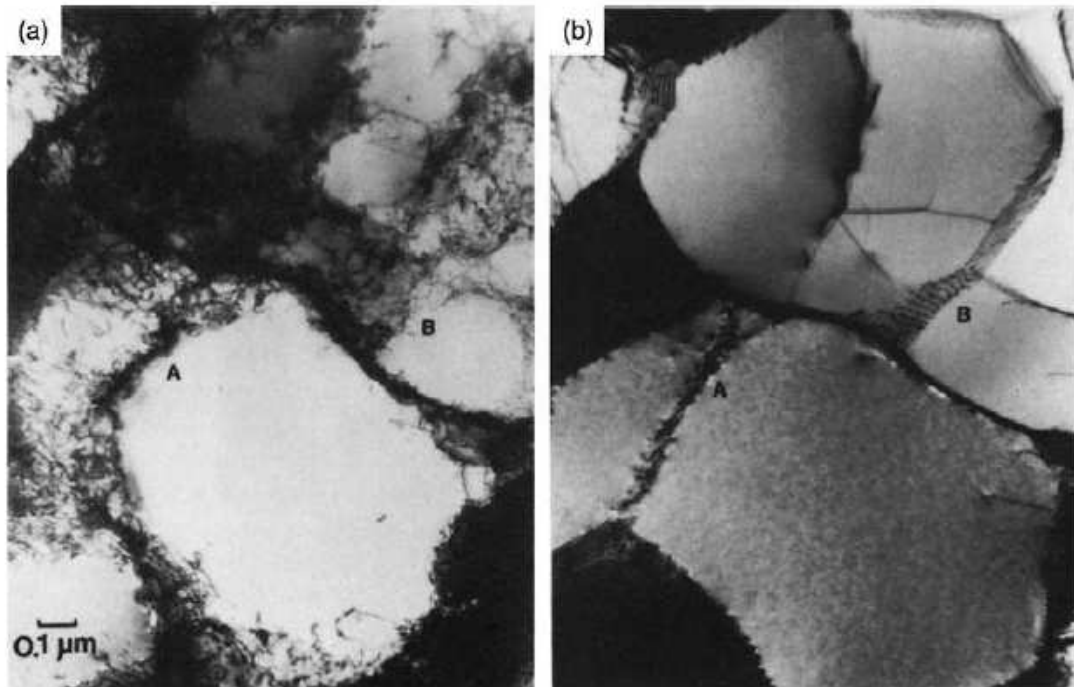


Figure 1.3: Transmission electron microscopy (TEM) of aluminium deformed 10% and annealed in-situ (a) as-deformed and (b) annealed for 2 minutes at 250°C [10]

size and dislocation density, will be used as progress parameters to model the kinetics of recovery - these models are discussed in section 1.1.3.

1.1.2.2 Microstructure evolution with recovery

The microstructure of the deformed metal evolves during recovery. The annihilation of dislocations and the rearrangement of the remaining dislocations result in subgrains that are free of dislocations, as shown in Figure 1.1. The subgrain boundaries separate regions that are disoriented with respect to each other by low values, this disorientation being accommodated by the dislocations present in these boundaries. Figure 1.3 shows transmission electron microscopy (TEM) images of an aluminium sample deformed 10% before and after annealing at 250°C [10]. It can be seen clearly in the deformed structure that the dislocations are tangled in the interior of the subgrains, and there are some dislocations that have formed cell-boundaries. After annealing for 2 minutes at 250°C, distinct equiaxed subgrains are visible with clear boundaries and very few dislocations within them.

1. BIBLIOGRAPHY

The subsequent and final step in recovery is subgrain growth, which reduces the total subgrain boundary area within the metal, thus reducing the surface energy associated with it. Therefore subgrain size may be used as a measure of the progress of recovery. However, it is often difficult to detect subgrain size, for example by EBSD due to ambiguity in the threshold disorientation value to be used. For example, Figure 1.4 shows two EBSD maps with the black lines representing disorientations greater than 15° , and in grey the disorientations greater than 0.5° (Figure 1.4(a)) and 1.5° (Figure 1.4(b)) [2]. It is visible in the two images that no clear disorientation limit can be attributed to the subgrain boundaries - a low limit includes disorientations arising from dislocations within subgrains and a higher limit misses subgrain boundaries resulting in non-closure. As a result, it is difficult to measure the subgrain size accurately.

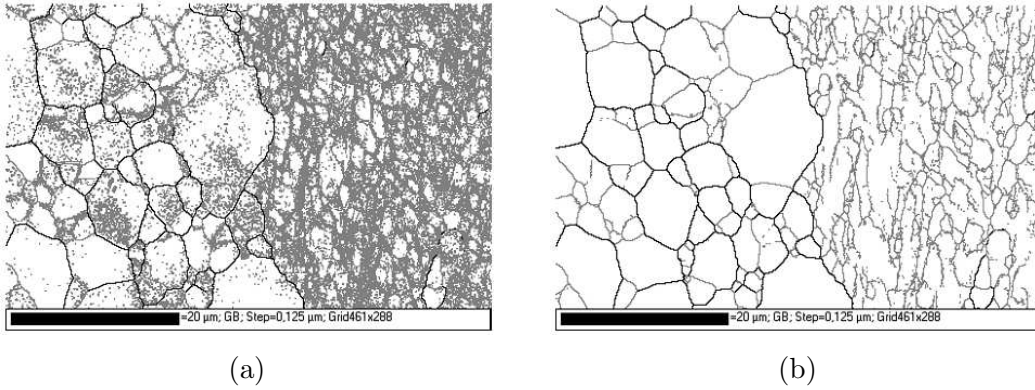


Figure 1.4: EBSD map representing disorientations greater than 15° in black and disorientations greater than (a) 0.5° and (b) 1.5° in grey [2]

In order to solve this problem, Barou [2] developed the method of Subgrain Reconstruction Mapping (SRM), which uses information from three maps - Euler angles, band contrast, and band slope - from EBSD, coupled with image processing techniques in order to detect subgrains boundaries resulting in closed subgrains. A sample result using this technique is presented in Figure 1.5.

Once the detection of subgrains is achieved, it is possible to measure their sizes relatively accurately. The subgrain size can then be used as a measure of the progress of recovery according to the equation 1.7.

$$R^2 - R_0^2 = \frac{M\gamma}{2}t \quad (1.7)$$

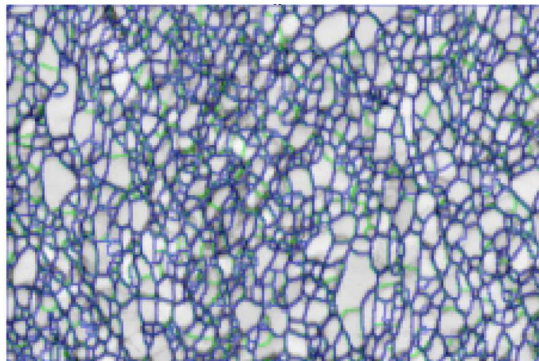


Figure 1.5: Microstructure resulting from Subgrain Reconstruction Mapping (SRM) with subgrain boundaries detected and closed subgrains [2]

where R and R_0 are mean subgrain sizes at time t and $t = 0$ respectively, M is the subgrain boundary mobility, and γ is the subgrain boundary energy.

Equation 1.7 is in fact the same as the power law equation for continuous grain growth derived by Burke and Turnbull [14]. This equation has been used by Huang et al. [15] for subgrain growth, assuming that subgrain growth is similar to grain growth. While this law has shown some agreement with experimental data, the exponent is not equal to 2 for the case of subgrain growth. As shown by Barou [2], the exponent was found to be between 6 and 10 for Al-0.1% Mn, and greater than 10 for Al-0.3% Mn. This suggests the need for an equation that is more general, and also the need for simulations that would take into account local properties instead of an average for the entire microstructure.

As mentioned above, this approach considers a mean subgrain size. However, when a polycrystalline sample is deformed by rolling, the grains rotate towards certain orientations, which have been termed the rolling texture components. The rate of subgrain growth in the bands belonging to these texture components has been observed by TEM to be different from that in other orientations [4]. Therefore, in order to study the effect of crystallographic orientation on the kinetics of recovery, it is important to study the rate of recovery in deformed single crystals.

1.1.2.3 Recovery in deformed single crystals

Albou et al. [6] have presented a study in which single crystals of Al-0.1%Mn were deformed in plane-strain compression using a channel die to a true strain of $\epsilon = 2.3$.

1. BIBLIOGRAPHY

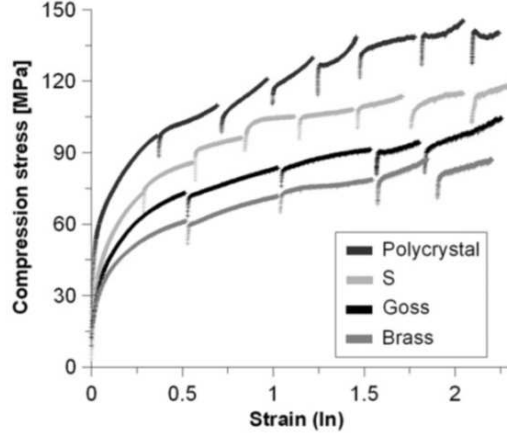


Figure 1.6: True stress-true strain curves of the deformation up to a true strain of 2.3 of Al-0.1%Mn monocrystals by plane strain compression [6]

This deformation is similar to the deformation given to metals in industry in forming processes such as cold-rolling. The orientations chosen for the single crystals were Goss $\{110\}\langle 001\rangle$, Brass $\{110\}\langle 112\rangle$ and S $\{123\}\langle 634\rangle$. Figure 1.6 shows the true stress-true strain curves for the deformation of the monocrystals of different orientations. The differences in crystallographic orientations result in different mechanical properties, and thus the flow stress values are not the same, and neither is the hardening behaviour.

The deformed monocrystals were then annealed at different temperatures and for different durations, and their hardness was measured in order to quantify the recovery kinetics. It was found that the softening in all the three crystals followed a logarithmic dependence on time, the Goss and S crystals softening at similar rates, while the Brass crystals softened much slower (see Figure 1.7).

The same behaviour is exhibited in the microstructural evolution - Goss and S oriented crystals show faster subgrain growth than the Brass oriented crystal. This is shown in Figure 1.8 where we find a larger increase in the subgrain size of Goss and S crystals than in the Brass crystal after 34 hours of annealing at 264°C.

The authors have measured the dislocation densities using X-ray line profile analysis and have found a rapid decrease in the early stages, lasting a few seconds, which represents the annihilation of dislocation dipoles, followed by a stage of subgrain growth in the Goss and S oriented crystals. The lower rate of subgrain growth in the Brass oriented crystal is attributed to the lower disorientations (4°) compared to the Goss

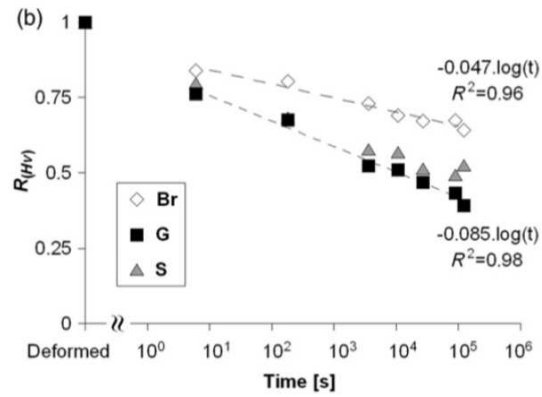


Figure 1.7: Fractional residual strain hardening as a function of time in Brass, Goss and S oriented crystals deformed in plane strain compression to a true strain of 2.3 and then annealed at 264°C [6]

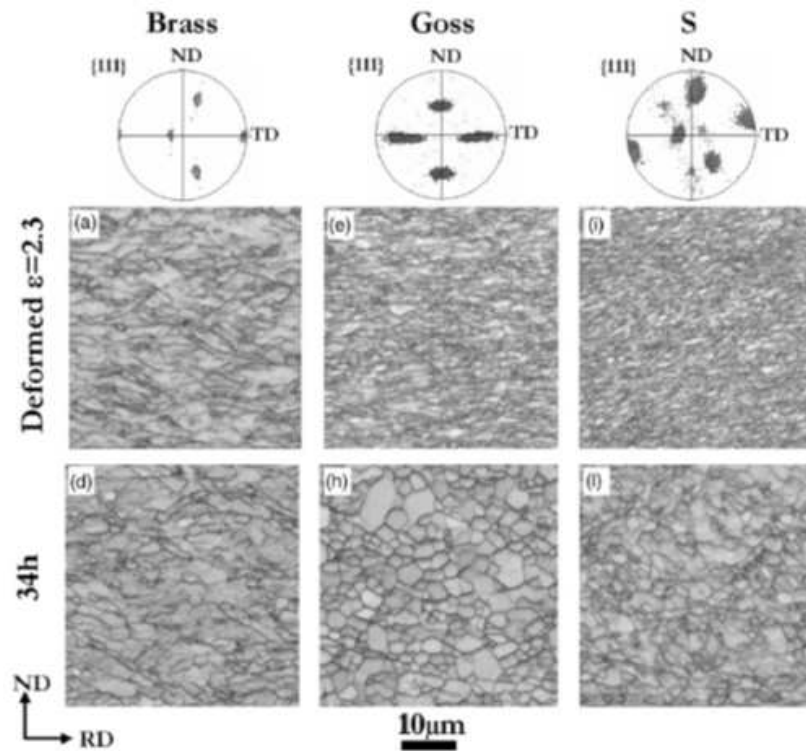


Figure 1.8: Time evolution of microstructure of deformed Al-0.1%Mn crystals annealed at 264°C for 34 hours [6]

1. BIBLIOGRAPHY

and S oriented crystals ($7-8^\circ$). It was also observed that the disorientation distribution evolved during annealing. The average non-correlated disorientation remained the same for Brass, but decreased for the Goss and increased for the S oriented crystals.

1.1.3 Modelling recovery kinetics

Modelling recovery based on the processes occurring within the material is rather difficult because the mechanisms shown in Figure 1.1 do not occur in discrete steps. There is an overlap in between the processes when one process has not yet ended and the next process has already begun. Therefore, it is not feasible to propose a single global model that takes into account all the phenomena.

The models proposed in the literature attempt to relate the different steps of recovery with measurements at the macroscopic scale like hardness, yield strength, mean subgrain size and mean dislocation density. The kinetic laws proposed in the literature measure the progress of recovery in terms of at least one of the following quantities:

1. Mechanical properties - such as hardness or yield strength, or derivative quantities like fractional residual strain hardening
2. Microstructural evolution - subgrain size
3. Dislocation density

1.1.3.1 Generic kinetic laws

The generic approach is to fit a single equation that would describe the progress of recovery with time. These laws describe either a logarithmic or a power law evolution of the progress parameter f with time t [10].

Logarithmic:

$$\frac{df}{dt} = -\frac{A}{t} \Rightarrow f = A' - A \ln(t) \quad (1.8)$$

Power law:

$$\frac{df}{dt} = -Bf^m \quad (1.9)$$

For $m > 1$:

$$f^{1-m} - f_0^{1-m} = B(m-1)t \quad (1.10)$$

For $m = 1$

$$\ln\left(\frac{f}{f_0}\right) = Bt \quad (1.11)$$

Another approach is to model the rate of recovery using the stored energy P as the parameter indicating the progress of recovery, in an Arrhenius-like rate law involving an activation energy Q . However, it has been shown that the activation energy does not remain a constant during recovery but increases as recovery progresses [16]. The activation energy represents the recovery mechanisms taking place at a given time. Since there are several overlapping mechanisms, the activation energy cannot remain a constant throughout recovery.

Vandermeer and Hansen [9] used this approach incorporating the variable activation energy by writing the rate law as in equation 1.12. This form was originally proposed by Kuhlmann-Wilsdorf et al. [17] using the flow stress and subsequently Borelius et al. [18] proposed a rate law in terms of the stored energy.

$$\frac{dP}{dt} = -PK_0e^{-\left(\frac{Q_0-\beta P}{RT}\right)} \quad (1.12)$$

Here P is the instantaneous stored energy, t the time, T the temperature, $(Q_0 - \beta P)$ the apparent activation energy, R the gas constant, and K_0 and β are constants.

Since it is difficult to measure the stored energy P , it is preferable to use another parameter that can be measured easily. In the situation of Figure 1.1(c), where all the dislocations are present in the subgrain boundaries, the stored energy per unit volume is inversely proportional to the mean subgrain size (equation 1.6). According to the Hall-Petch relationship, mechanical properties like the yield stress and hardness depend inversely as the square root of the mean domain size. Therefore, the stored energy would be proportional to the square of the hardness or the yield stress. If we consider that the stored energy has an initial value P_0 and reduces to zero at the end of recovery, we require a function that varies from 1 to 0, and is proportional to the square of the hardness. For this reason the variation of the stored energy P is taken by Vandermeer and Hansen to follow equation 1.13.

$$P = P_0f^2 \quad (1.13)$$

with

$$f = \frac{H - H_r}{H_d - H_r} \quad (1.14)$$

1. BIBLIOGRAPHY

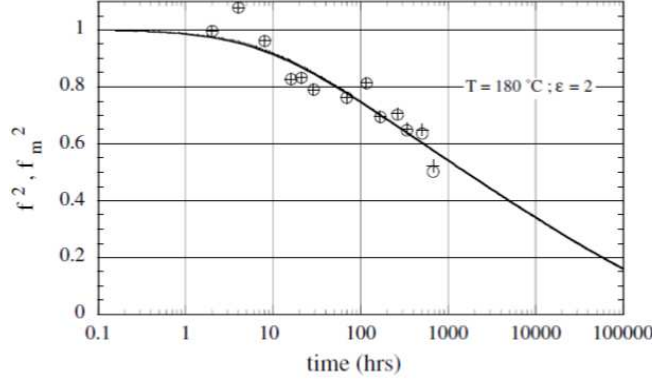


Figure 1.9: Isothermal recovery kinetics modeled using the equation proposed by Vandermeer and Hansen [9]. The crosses represent the square of the fractional residual strain hardening and the solid line is the equation resulting from the parameters calculated from the experimental data.

In equation 1.14, f is the fractional residual strain hardening with H , H_r and H_d being the instantaneous, fully recovered and as-deformed values of hardness respectively.

Using equation 1.13 in the differential equation 1.12, and integrating from $f^2 = 1$ to f^2 , we get the following equation.

$$E_1\left(\frac{\beta P_0}{RT} f^2\right) = E_1\left(\frac{\beta P_0}{RT}\right) + t t_0^{-1} \quad (1.15)$$

where

$$E_1(x) = \int_{t=x}^{\infty} \frac{e^{-t}}{t} dt = \int_{t=1}^{\infty} \frac{e^{-xt}}{t} dt \quad (1.16)$$

and

$$t_0^{-1} = K_0 e^{-\frac{Q_0}{RT}} \quad (1.17)$$

From hardness measurements after annealing for different durations at different temperatures, Vandermeer and Hansen obtained a set of (t, f^2) data at each temperature. Each such pair forms a curve of the form of equation 1.15 in the $\left(\frac{\beta P_0}{RT}, t_0^{-1}\right)$ space. The point of convergence of all the curves at a given temperature yields an estimate of the values of $\frac{\beta P_0}{RT}$ and t_0^{-1} at that temperature. Calculating these values at several temperatures finally yields the values of βP_0 and the activation energy Q_0 . The resulting curves, shown in Figure 1.9, are in good agreement with the experimental data.

This model was also used by Yu [19] to study the kinetics of recovery in commercial purity aluminium AA1050 deformed by cold rolling and commercial purity aluminium AA1100 deformed by accumulative roll bonding (ARB).

1.1.3.2 Analytic kinetic laws

The other approach is to look at the phenomena occurring during recovery represented in Figure 1.1 and constructing a model based on them. This approach is described by Nes in his review of studies on recovery [13]. As mentioned earlier, the overlap between two mechanisms is an obstacle to proposing a single analytical model. In order to overcome this, a rate equation for each mechanism is formulated and one of two approaches is taken:

1. Fractional approach: adding the fractional contributions from each mechanism to obtain the final recovery rate
2. Sequential approach: considering the mechanisms to occur sequentially with little or no overlap

The two mechanisms refer to the effect of the forest of dislocations and that of the subgrain size. In the fractional approach, the contributions of the dislocation density and of the mean subgrain size are taken to be f_1 and f_2 respectively, with $f_1 + f_2 = 1$. This yields the expression for the fractional residual strain hardening R as a function of time t in equation 1.18.

$$R(t) = f_1 \sqrt{\frac{\rho(t)}{\rho_0}} + f_2 \frac{\delta_0}{\delta(t)} \quad (1.18)$$

with ρ and δ representing the dislocation density and mean subgrain size respectively, the subscript 0 the initial value, and the argument t the value at time t .

The sequential approach considers the flow stress to depend initially on the forest of dislocations. At a certain time critical time, a transition occurs, after which the flow stress depends on the subgrain size. This transition is not abrupt, and an appropriate function is chosen to cause a smooth transition from one domain to the next. The final equation is of the following form.

$$R(t) = f \sqrt{\frac{\rho(t)}{\rho_0}} + (1 - f) C \frac{\delta_0}{\delta(t)} \quad (1.19)$$

1. BIBLIOGRAPHY

The critical time for transition and the smooth transition function are both present in the parameter f , and C is a constant proportional to $(\delta_0\sqrt{\rho_0})^{-1}$.

In spite of the striking similarity between the equations 1.18 and 1.19, their behaviours differ due to the difference in the definitions of f in the two cases. The fractional approach has a value of f_1 that varies gradually while the sequential approach has a value of f that is constant over a period of time when the effect of the dislocation forest is dominant, then changes quickly to the value for the time when the effect of the mean subgrain size dominates.

1.2 Simulations of grain growth

Sections 1.1.2 and 1.1.3 have shown the wealth of research that has been conducted on experimental studies and the modelling of recovery. However, no instances of simulations of recovery were found in the literature. The simulation of annealing phenomena have mainly concentrated on the phenomenon of grain growth. It has been suggested that subgrain growth during recovery follows kinetics similar to that of grain growth [20]. Therefore, these simulation methods may be adapted to the case of subgrain growth.

Analytical theories of grain growth have successfully treated the problem of grain growth with isotropic boundary conditions. Real microstructures are anisotropic with grain boundary properties such as energy and mobility varying as functions of the boundary disorientation and other factors. Hence, there is a need for computer simulations in order to model grain growth taking into account the properties of different grain boundaries.

Several types of 2 and 3 dimensional computer simulations of grain growth exist. The 3 major types, presented in Figure 1.10, are the vertex model, Monte Carlo Potts model and the phase-field model [21].

1.2.1 Vertex dynamics simulations

1.2.1.1 Introduction

The vertex dynamics model is a deterministic model that treats the grain boundaries as line segments discretized using vertices placed on them and at the triple points. This

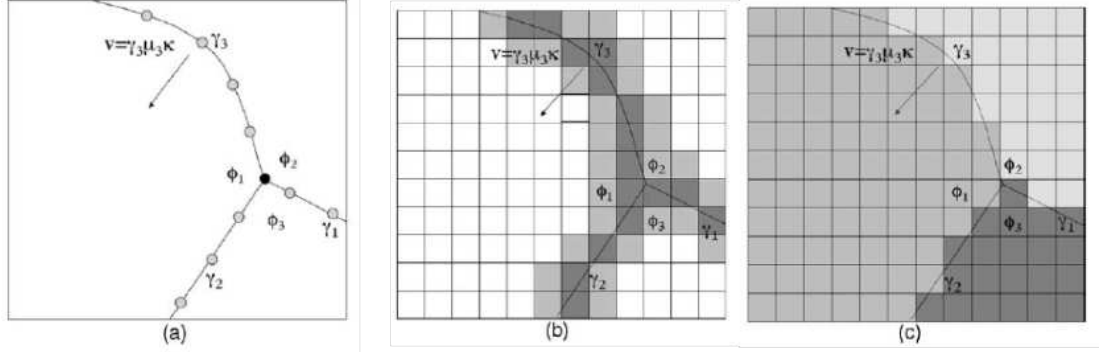


Figure 1.10: Different types of models to simulate grain growth: (a) Vertex dynamics, (b) Monte Carlo Potts model and (c) Phase-field model [21]

model was first introduced by Kawasaki et al. [22] and further developed by Weygand et al. [8].

1.2.1.2 Brief description

The boundary migration is applied by calculating the velocities of the vertices using the following equation:

$$v = m(\theta, T)\gamma(\theta, T)\kappa \quad (1.20)$$

where v is the vertex velocity, m and γ are the boundary mobility and energy respectively that are functions of the grain boundary disorientation θ and the temperature T , and κ is the local curvature of the grain boundary at the position of the vertex. The disappearance of shrinking grains and topological transformations of short segments are carried out through a set of topological rules that are defined in the simulation [21].

1.2.1.3 Application

Vertex dynamics simulations have been successfully applied to the problem of grain growth in two and three dimensions [8, 23, 24, 25, 26, 27] and also to grain growth in the presence of Zener pinning [26]. Figure 1.11 shows the result of a vertex dynamics simulation in three dimensions of a grain boundary migrating through a field of pinning particles.

Discontinuous grain growth has also been simulated using vertex dynamics [7]. Following the observation of abnormal subgrain growth in deformed Goss-oriented single

1. BIBLIOGRAPHY

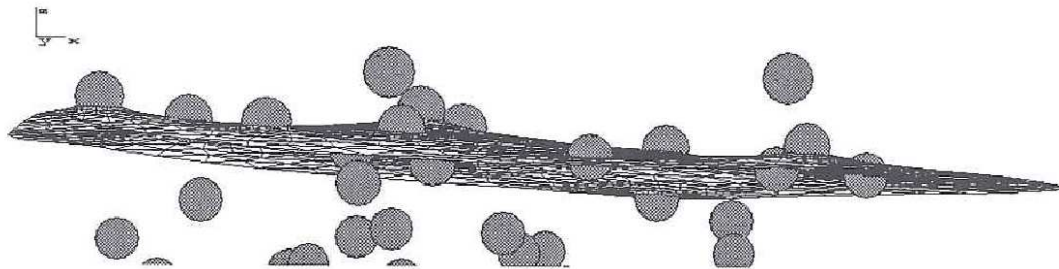


Figure 1.11: Result of a vertex dynamics simulation in three dimensions using the finite element method showing the pinning of a migrating grain boundary by particles [26]

crystals by Ferry et al. [28], Humphreys [29] suggested a criterion for the instability - that the subgrains having a size larger than the average value have a slightly different disorientation compared to the average. In the vertex dynamics simulation, a subgrain structure having a narrow initial size distribution was created using Voronoi tessellation, and a few subgrains with sizes larger than the average were given higher than average disorientations, according to the instability criterion proposed by Humphreys. Experimental values for the mobility and energy of grain boundaries were used, and the results obtained matched the experimental observations of abnormal grain growth in the deformed Goss crystals.

A study by Barrales Mora [24] using two-dimensional vertex dynamics simulations investigated the effect of a magnetic field on grain growth. This simulation was different from the ones used by Maurice et al. in that separate mobility laws were used for grain boundaries and triple junctions. The results were in good agreement with the theory suggesting that grains having certain orientations with respect to the applied magnetic field would have a growth advantage, leading to the development of a strong texture during grain growth.

Barrales Mora et al. [25] also carried out vertex dynamics simulations in three-dimensions. Figure 1.12 shows a result from this simulation with two grains, one growing and the other shrinking.

More recently, this model has been used to study grain growth in thin films and Cu-Damascene interconnects used widely in microelectronic devices. One of the results of this work is shown in Figure 1.13 [30].

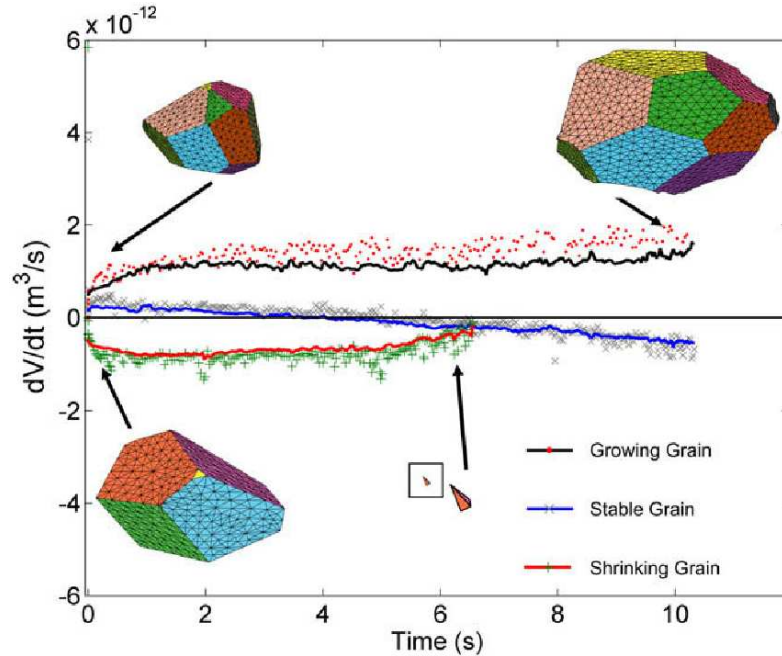


Figure 1.12: Growing and shrinking grains in a three-dimensional vertex dynamics simulation [25]

1.2.2 Monte Carlo Potts model

1.2.2.1 Introduction

The Monte Carlo Potts model is a stochastic method in which a lattice is defined (as seen in Figure 1.10(b)) and the lattice points are allocated to different grains. No grain boundary is specified explicitly - it is defined by adjacent lattice points that belong to different grains. Next, the energy of the system is calculated using the interfacial energy of the grain boundaries. The evolution of the microstructure is carried out through random jumps of the boundaries in the thermodynamically favoured directions. This method is simple to apply, relative to the vertex dynamics and the phase-field models, and also rather elegant in that the behaviour of triple points and the topological transformations are handled automatically as a result of the condition of minimizing the total interfacial energy. The main disadvantages of this approach are:

1. When anisotropic boundary energy and mobility laws are used, lattice defects form that cause boundary distortion

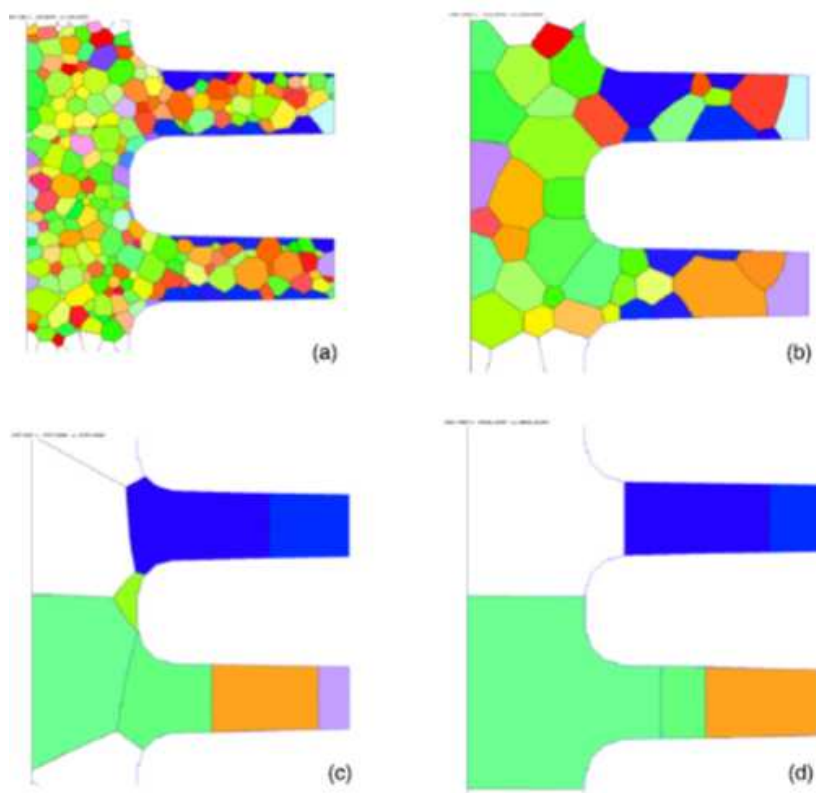


Figure 1.13: Vertex dynamics simulation of grain growth in Damascene interconnects used in microelectronic devices [30]

2. The correspondence between the jump frequency and the physical time is unknown

1.2.2.2 Application

Owing to the relative ease of application of the method and the advantage of lower computational load compared to other methods of simulating grain growth, the Monte Carlo Potts model has been applied in two and three dimensions by several authors. Figure 1.14(a) shows an example of a three-dimensional simulation of Zener pinning using the Monte Carlo Potts model [31]. In Figure 1.14(b) we see a Monte Carlo Potts model simulation of recrystallization with isotropic and anisotropic grain boundary energies [32].

1.2.3 Phase-field models

1.2.3.1 Introduction

The third kind of model used to simulate grain growth is the phase-field model. In this model, the microstructure is defined by a set of continuous field variables $\eta_i(\vec{r})$ such that its value is 1 when the position \vec{r} is within the grain g , and continuously decreases at the boundaries to have a value of zero elsewhere. This gives the grain boundaries a finite thickness [21, 33].

Next the total free energy of the system is calculated using the free energy density as a function of the orientation field variables and their gradients which are non-zero only at the grain boundaries. The evolution of the microstructure is calculated by solving the following set of Ginzburg-Landau equations:

$$\frac{\partial \eta_i(r, t)}{\partial t} = -L_i \frac{\delta F}{\delta \eta_i(r, t)}, i = 1, 2, \dots, p \quad (1.21)$$

where F is the total free energy, t the time, and L_i the relaxation coefficients [33].

The correctness of the microstructural evolution depends on the choice of the free energy density function used, and also on the number of orientation field variables p . Therefore the choice of the free energy density function is crucial, and it must be chosen such that it reflects the phenomenon to be modelled. The method is quite expensive in terms of computation as energy minima are to be calculated for each order

1. BIBLIOGRAPHY

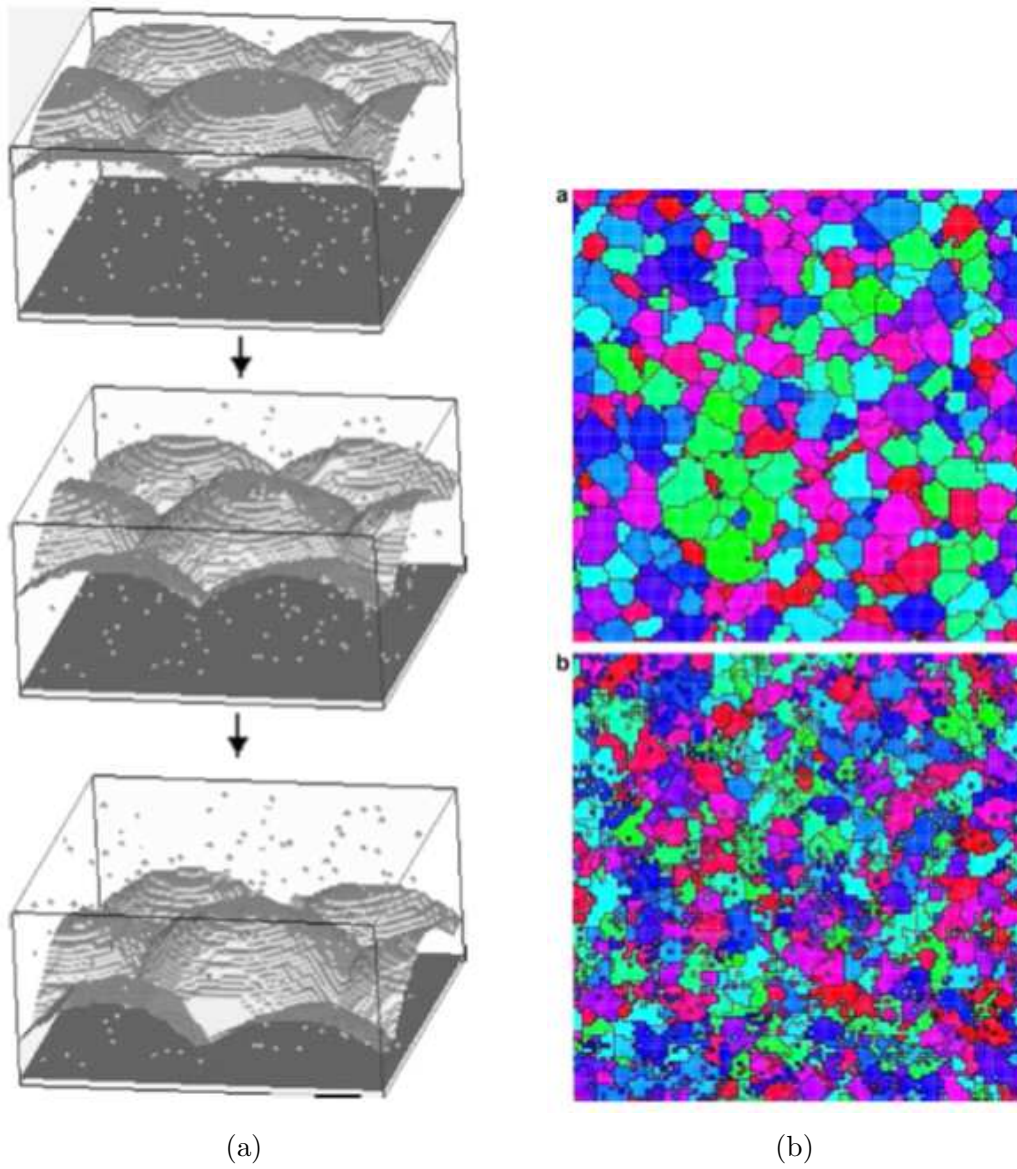


Figure 1.14: (a) Zener pinning simulation using Monte Carlo Potts model [31] (b) Simulation of recrystallization with isotropic (top) and anisotropic (bottom) grain boundary energies [32]

parameter. However, unlike the vertex model, no rules are required for the topological transformations as these take place automatically as a result of the minimization of the energy functional.

1.2.3.2 Application

Despite the difficulty involved in formulation of the free energy density function, and the relatively high computational cost involved, there are several examples available in the literature of the phase-field model applied to the problem of grain growth.

In Figure 1.15 we see a simulation of grain growth by Fan et al. [33] with 512 grid points in each direction and 36 orientation field variables. The grain growth is found to follow the parabolic growth law, i.e. $R(t)^m - R(0)^m = kt$, where $R(t)$ is the mean grain radius at time t , k and m are constants and $m = 2$.

More recent applications of the phase-field model have coupled with the finite element method [34]. In this method, the grain boundary velocity is calculated using an equation similar to equation 1.7 with the difference being that the energy and curvature are replaced by force and the grain boundary normal vector. The force on the boundary is evaluated by multiplying the dislocation line energy with the difference in dislocation densities across the grain boundaries. The novel aspect of this work is the application of the level-set framework - a popular method to track interfaces and boundaries that change form with time - to the problem of grain growth. In this method, a grain i is given its own private level-set function ϕ_i such that its boundary Γ_i is defined by equation 1.22. The velocity of the interface \vec{v} is then given by equation 1.23.

$$\Gamma_i = \{(x, y) \mid \phi_i(x, y) = 0\} \tag{1.22}$$

$$\frac{\partial \phi_i}{\partial t} + \vec{v} \cdot \nabla \phi_i = 0 \tag{1.23}$$

1.2.4 Comparison between different models

The stochastic methods involving the Monte Carlo Potts model have an advantage with regard to simplicity of application in two and three dimensions, while the deterministic methods like vertex dynamics and phase-field are considerably more complex. However, the fact that the Potts model used a space scale that does not correspond to the

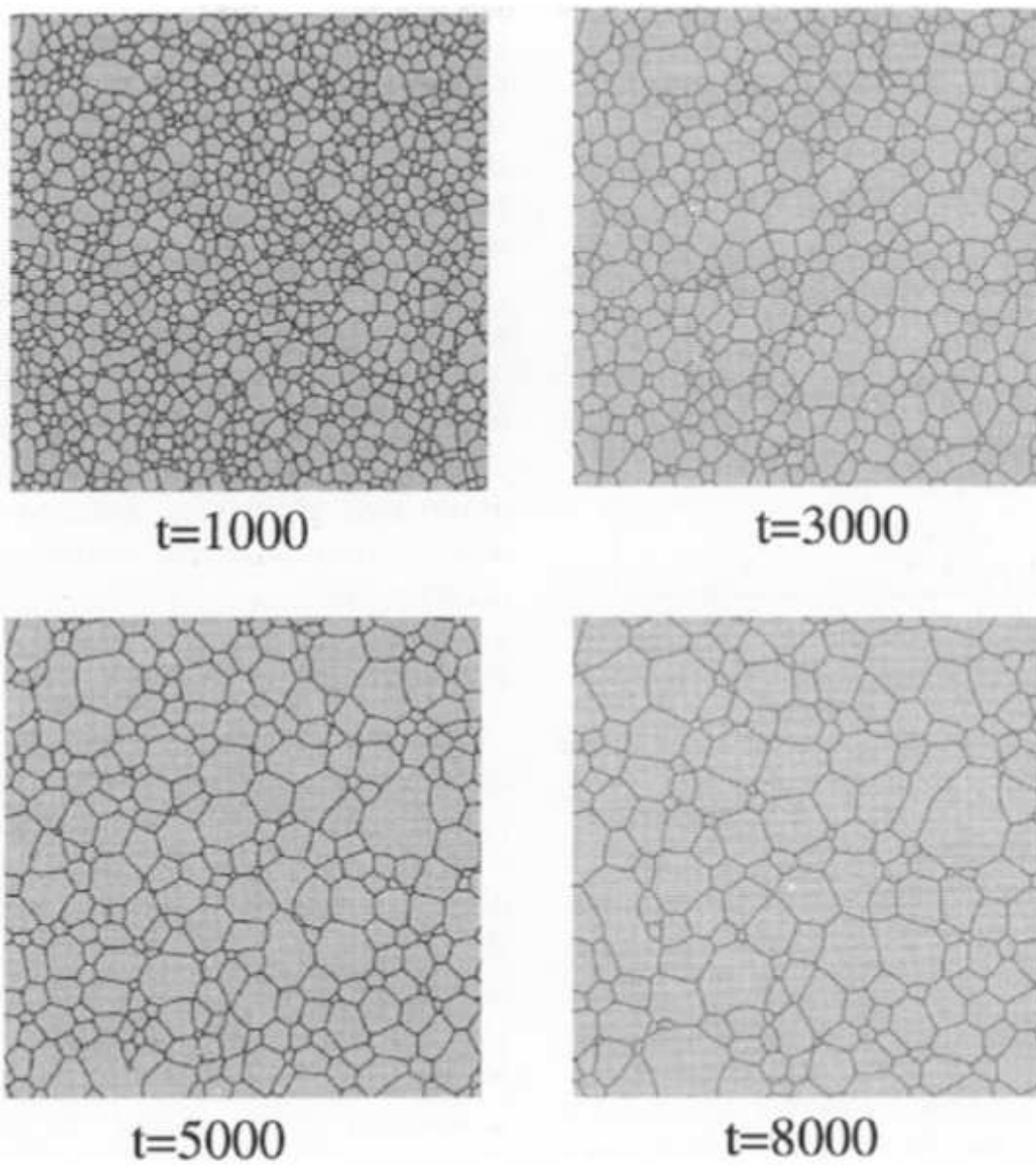


Figure 1.15: Phase-field simulation of grain growth [33]

atomistic scale, and that the Monte Carlo time step does not correspond to the physical time, introduce some arbitrariness into the procedure.

If the kinetics of recovery is to be simulated, an unambiguous time scale is required. Therefore, the choice is restricted to the deterministic methods. Between the vertex and phase-field models, the application of the vertex model seems to be more economical, both in terms of complexity of application and the computational cost. Therefore the vertex dynamics model was selected to simulate recovery. More details about its application to the problem are given in Chapter 2 which is dedicated to vertex dynamics.

1.3 Objectives of the thesis

Based on the current state of awareness on the subject of recovery and the effect of crystallographic orientation, it is proposed that vertex dynamics simulations of subgrain growth be carried out with initial microstructures similar to the deformation microstructures of monocrystals studied by Albou et al. [6] in order to gain some insight into the difference in recovery rates between Brass and Goss oriented crystals. An advantage of carrying out the simulations is the ease with which the distributions of disorientations between neighbouring subgrains can be obtained. These distributions might yield some insight into the reasons for the difference in recovery rates.

Mobility, activation energy and subgrain boundary energy for Al-0.1%Mn are already reported in the literature [3, 35]. The estimation of activation energy by Barou et al. [3] used a method involving the reconstruction of subgrains and measuring their sizes as they evolved during annealing. Vandermeer and Hansen [9] have proposed a model of recovery kinetics which can be used to estimate the activation energy using microhardness measurements on a deformed sample. This method is simpler compared to the one used by Barou et al. It is proposed that a polycrystalline bar of the alloy be deformed by cold rolling to a large strain and samples taken from this rolled bar will then be annealed for different durations and at different temperatures. Hardness measurements will be made on each sample and then equation 1.15 will be used to estimate the activation energy Q_0 .

The activation energy Q_0 estimated from the experiments, and the pre-exponential term for mobility m_0 and HAGB energy γ_{HAGB} reported in literature will then be used in the simulations as material parameters representing the Al-0.1%Mn model alloy. A

1. BIBLIOGRAPHY

quantitative comparison will be made between the rates of subgrain growth in Brass and Goss crystals, and the reasons for differences, if any, will be explored. Since it is easy to measure subgrain sizes in the simulations, the kinetics of recovery in the structures will also be matched with recovery models based on subgrain size.

2

Vertex dynamics simulations

2.1 Introduction

This chapter presents detailed descriptions of the method of generating microstructures using Voronoi tessellation and the vertex dynamics simulations for grain and subgrain growth. These methods have been used to study the influence of crystallographic orientation on the rate of recovery in Al-Mn binary alloys.

Section 2.2 contains the description of the use of Voronoi tessellation to generate the microstructures for the simulations. Section 2.3 presents the basic principles of the vertex dynamics method for simulating grain and subgrain growth. In section 2.4, these principles are validated by comparing with simple cases that can be solved for analytically and section 2.5 describes the necessary changes to be made to the method in order to simulate subgrain growth.

2.2 Microstructure generation using Voronoi tessellation

2.2.1 Definition

The microstructures for the simulation are created using Voronoi Tessellation. Voronoi Tessellation is a decomposition of space into domains, each of which corresponds to a certain *seed* point, in such a way that all points within a given domain are closer to its own seed point than to any other.

This definition can be stated more mathematically as follows. Let $X = \{x_1, x_2, x_3, \dots\}$ be a non-empty set of points x_i ,

2. VERTEX DYNAMICS SIMULATIONS

$d(x_i, x_j)$ be the distance function between the points x_i and x_j , $x_i, x_j \in X$, and $P = \{p_1, p_2, p_3, \dots\} \in X$ the set of n seeds p_i ($1 \leq i \leq n$).

Using these n seeds, we can define n Voronoi domains V_k ($1 \leq k \leq n$) as follows:

$$V_k = \{x \in X : d(x, p_k) < d(x, p_j) \forall j \neq k\} \quad (2.1)$$

In this way, a Voronoi tessellation can be created from a set of points P .

2.2.2 Program voronoi2d

The program `voronoi2d` has been written using C++ for the purpose of generating two-dimensional microstructures. Structures generated using this program have periodic boundary conditions and there is also the possibility of creating microstructures similar to rolled structures with flattened grains.

This program uses the fact that a Voronoi Tessellation is the dual of a Delaunay triangulation. The generation of the structure is achieved in four steps:

1. Create a set of random points P . The dimensions of the domain containing these points depend on the number of domains required, their mean diameter, and their form in the case where a rolled structure is desired.
2. Triangulate the space using the points P as the vertices of the triangles. The triangulation is carried out using the Delaunay criterion, i.e. for each triangle, only its three vertices lie on its circumcircle, and no other points lie within.
3. The positions of the circumcentres of each of the triangles are calculated. These points are the vertices of the polygons that will form the Voronoi tessellation, and the perpendicular bisectors of the arms of the triangles will be sides of the polygons. The polygons obtained at this stage are equiaxed.
4. If a structure representing rolled grains is desired, one of the axes is scaled appropriately to achieve this effect.

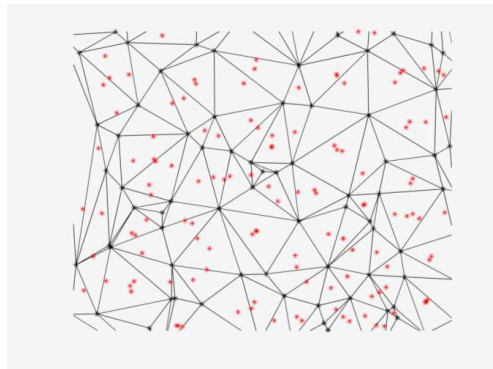
The first three steps listed above are represented schematically in Figure 2.1.

The Vertex Dynamics Simulations program that will use this structure requires periodic boundary conditions, i.e. the top edge of the Voronoi Tessellation must fit in

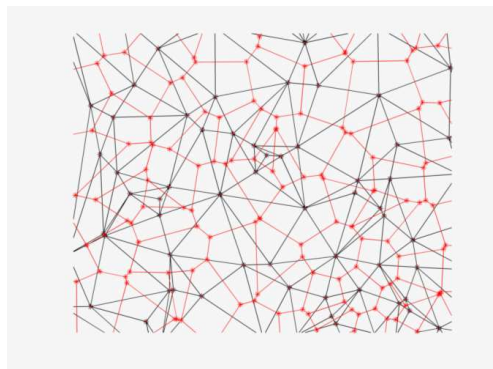
2.2 Microstructure generation using Voronoi tessellation



(a) Points



(b) Triangulation



(c) Voronoi tessellation

Figure 2.1: Schematic representation of Voronoi Tessellation using Delaunay triangulation: (a) Generation of a random point field (black points) (b) Triangulation of the point field using the Delaunay triangulation (black lines) and calculating the positions of the circumcentres (red points) (c) Joining the red points to obtain the Voronoi Tessellation (red lines)

2. VERTEX DYNAMICS SIMULATIONS

exactly with the bottom edge, and similarly for the left and right edges. As a result, the Voronoi tessellation represents one tile in an infinite tiling of two-dimensional space. Analogous to this tiling example, the structure represents a small repeating part of the entire microstructure.

The structure generated is stored in two files:

1. A `.nod` file containing the coordinates of the vertices
2. A `.c11` file containing the vertex lists of each polygon. The vertices are referred to using integers that correspond to the order of appearance in the `.nod` file.

Figure 2.2 shows a structure generated using `voronoi2d` with 5000 domains, with a mean radius of 5 microns.

2.3 Principles of the vertex dynamics simulations

2.3.1 History

Vertex dynamics simulations were developed by Kawasaki et al. [22]. In their simulations, the grain boundary triple points were represented by the vertices of polygons and the grain boundaries themselves were the sides of these polygons. As a result, the grain boundaries remained straight segments during grain growth.

The simulations were further improved by Weygand et al. [8] by introducing extra vertices (called *virtual* vertices - as opposed to *real* vertices at the triple points) on the grain boundaries in order to simulate their curvature.

In either case, the migration of grain boundaries is driven by the reduction in the energy of the system by reducing the total grain boundary length - or surface area in three dimensions. This is essentially what is termed curvature driven boundary migration.

2.3.2 Program `networkConsole`

The program `networkConsole` has been written using C++ to carry out Vertex Dynamics simulations in two dimensions. The program reads the structure generated using `voronoi2d` as input, along with other simulation parameters like temperature, stopping criterion, statistics to be written to file and the frequency with which they are to be

2.3 Principles of the vertex dynamics simulations

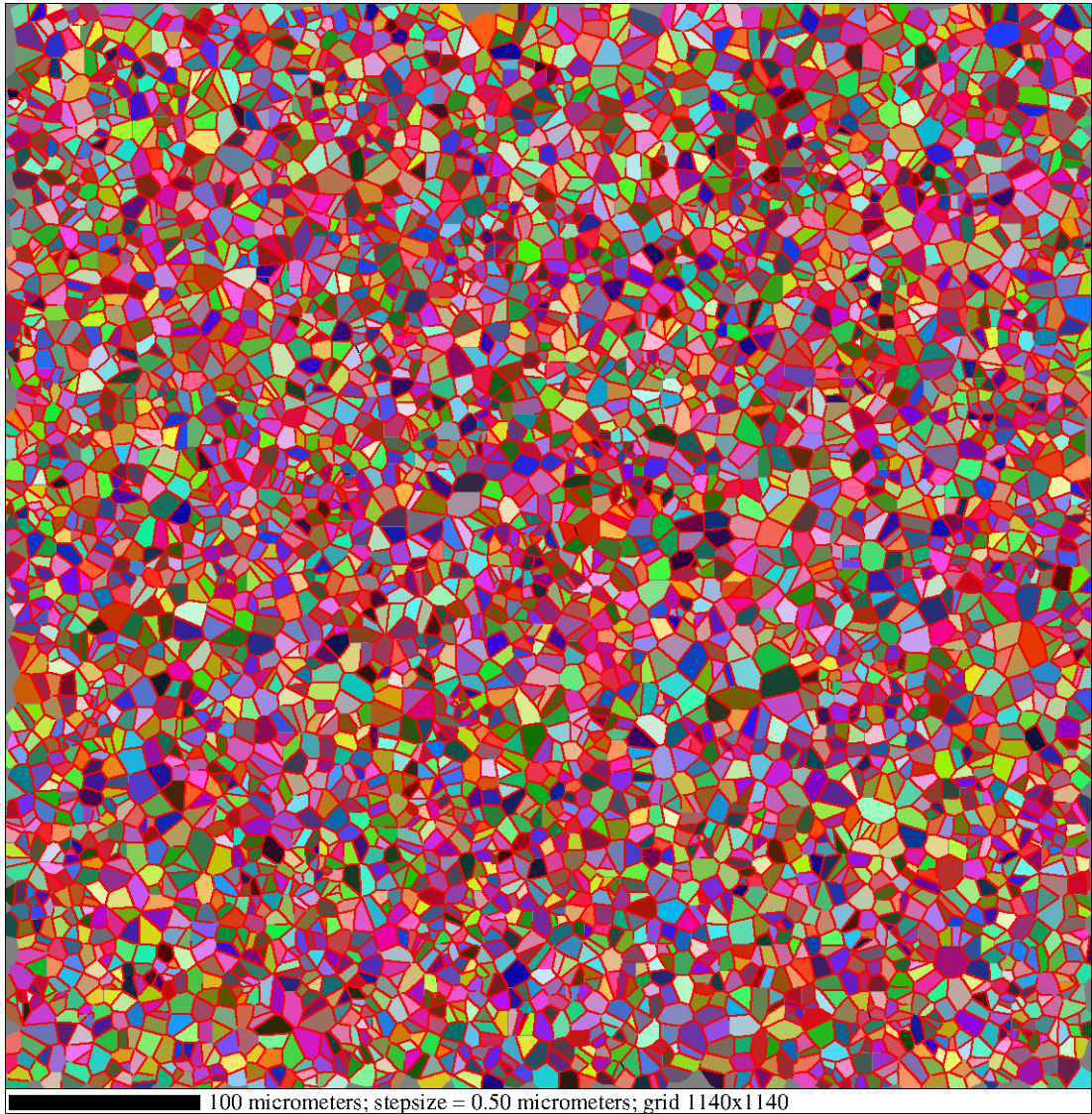


Figure 2.2: Microstructure generated using `voronoi2d` with 5000 domains and a mean radius of $5 \mu\text{m}$.

2. VERTEX DYNAMICS SIMULATIONS

written, and finally material parameters like the pre-exponential term for mobility and the high-angle grain boundary energy. It proceeds then to carry out the simulation. The flowchart of the program is presented in Figure 2.3. For details on the data structures used in the program, refer to Appendix A. All calculations involving crystallographic orientations are carried out using the library `orilib` developed by Romain Quey and distributed freely under the GNU Public License v3.0 [36].

The equations used to calculate the velocity of vertices, and the mobility and energy of subgrain boundaries are explained in section 2.3.3, the topological transformations in section 2.3.4 and the determination of the time increment in section 2.3.5.

2.3.3 Velocity of vertices

Each vertex in the simulation is connected to other vertices - 2 for virtual vertices and 3 for real vertices. For a vertex i , the velocity \vec{v}_i is calculated using the equation 2.2.

$$D_i \vec{v}_i = \vec{f}_i - \frac{1}{2} \sum_j D_{ij} \vec{v}_j \quad (2.2)$$

where

$$\vec{f}_i = \sum_j \vec{f}_{ij} = \sum_j \gamma_{ij} \frac{\vec{r}_{ij}}{|\vec{r}_{ij}|} \quad (2.3)$$

$$D_{ij} = \frac{1}{3m_{ij} |\vec{r}_{ij}|} (n_{ij} \otimes n_{ij}) \quad (2.4)$$

$$D_i = \sum_j D_{ij} \quad (2.5)$$

Here \vec{r}_{ij} is the vector representing the boundary segment joining the vertices i and j , m_{ij} its mobility, γ_{ij} its energy, and n_{ij} its normal vector. The vector \vec{v}_j is the velocity of the vertex j connected to the vertex i .

The equation for the velocity of the vertex i is essentially an equation of conservation of energy, where the term \vec{f}_i represents the potential or surface energy available, and the other terms containing the velocities represent the dissipation of this energy due to the movement of the boundary segments [8].

2.3 Principles of the vertex dynamics simulations

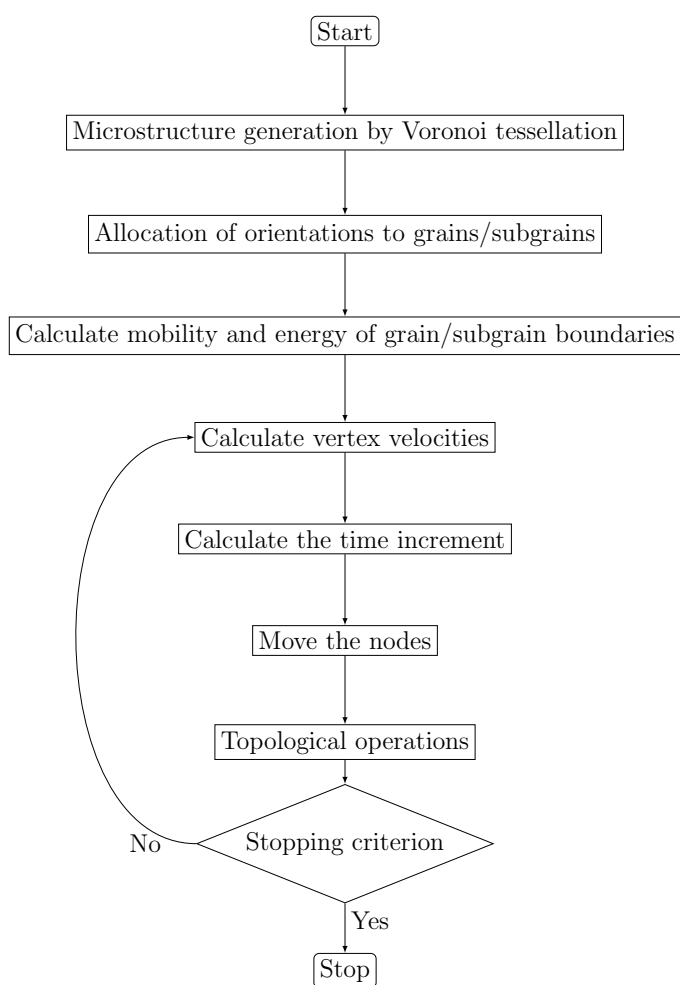


Figure 2.3: Flowchart of the program `networkConsole` to carry out vertex dynamics simulations in two dimensions

2. VERTEX DYNAMICS SIMULATIONS

2.3.3.1 Geometry

The term \vec{f}_i in the equation of the velocity represents the surface energy available for the migration of boundary segments through the movement of vertices. This term is the result of a vector addition of the directions and energies of each of the segments of the vertex i .

Figure 2.4 shows the two kinds of connections that a vertex may have. In the vertex velocity equation 2.2, the real and virtual vertices differ from each other only in that the real vertices have three connections while the virtual vertices have two. Since \vec{f}_i is a sum of the vectors in the directions of the segments, and these vectors are weighted by the energies of these segments, the vertex will have a tendency to move more towards a segment having higher energy, and thus contribute to the reduction of energy stored in the system. In the special case when the energies of all the segments are identical and the angles between the segments is 120° for a real vertex and 180° for a virtual vertex, then the vertex is at equilibrium because $\vec{f}_i = \vec{0}$.

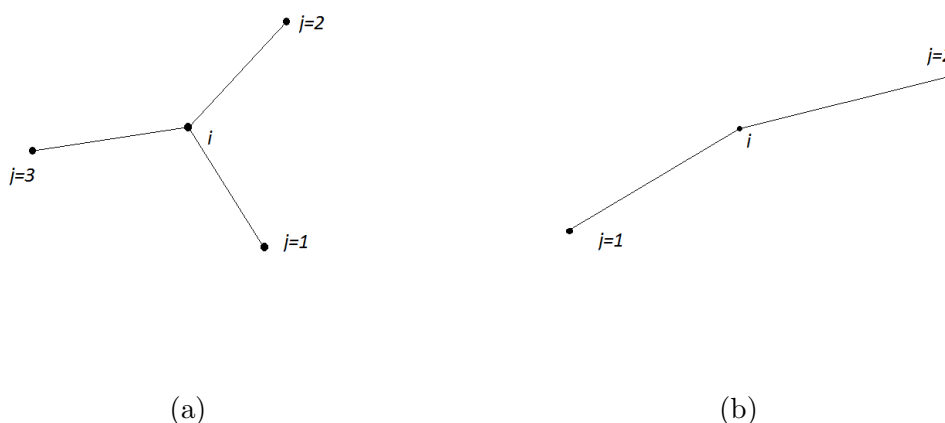


Figure 2.4: Connections of vertices - (a) Real vertex with 3 connections and (b) Virtual vertex with 2 connections

2.3.3.2 Energy of subgrain boundaries

The boundary energy γ_{ij} plays a crucial role in the expression of \vec{f}_{ij} . The program `networkConsole` uses the Read-Shockley expression [12] for the boundary energy:

$$\gamma = \gamma_0 \frac{\theta}{\theta_0} \left[1 - \ln \left(\frac{\theta}{\theta_0} \right) \right] \quad (2.6)$$

where γ_0 is energy of a high-angle grain boundary (HAGB), θ the boundary disorientation and θ_0 the HAGB disorientation, taken to be 15° . This expression is used for all disorientation angles less than the HAGB disorientation. For values greater than the HAGB disorientation, the boundary energy is taken as γ_0 . Figure 2.5 shows the variation of the boundary energy with disorientation evaluated using this equation.

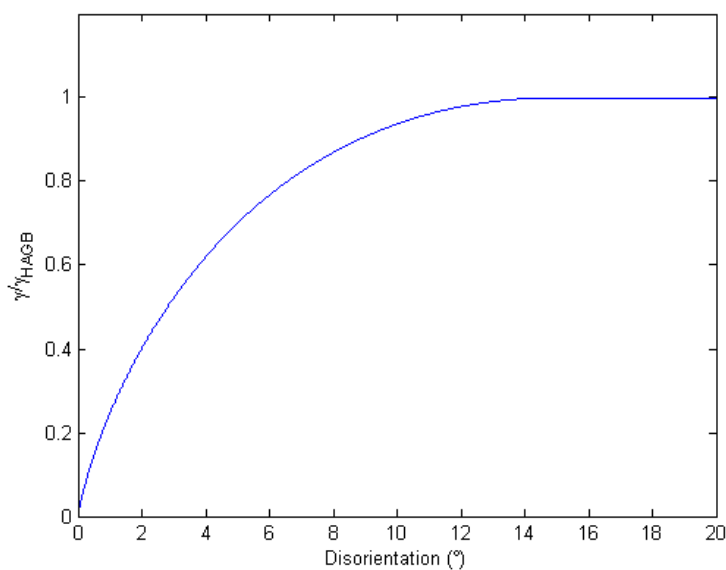


Figure 2.5: Subgrain boundary energy as a function of disorientation angle, evaluated using the Read-Shockley expression [12]

This is a rather simple description of the grain boundary energy as it depends on nothing but the boundary disorientation. Other descriptions of grain boundary energy, depending on disorientation axis, or coincidence site lattice (CSL) etc. [37] or on other factors like the inclination and tilt of boundaries [38], may easily be used in place of this equation.

2. VERTEX DYNAMICS SIMULATIONS

2.3.3.3 Mobility of subgrain boundaries

The dissipation terms in the equation of the vertex velocity include the mobility m_{ij} of the boundary segment joining the vertices i and j . In the program `networkConsole`, the mobility of a boundary having a disorientation $\theta < \theta_0$ is calculated using the expression in equation 2.7 due to Humphreys [29].

$$m = m_{HAGB} \left[1 - e^{-B(\theta/\theta_0)^n} \right] \quad (2.7)$$

where m_{HAGB} is the HAGB mobility, $B = 5$ and $n = 4$ are constants, θ and θ_0 are the boundary disorientation and HAGB disorientation respectively. The HAGB mobility is strongly dependent on the activation energy for boundary migration and the temperature according to equation 2.8.

$$m_{HAGB} = m_0 e^{-Q/RT} \quad (2.8)$$

m_0 is the pre-exponential term for the HAGB mobility and is related to the self-diffusion coefficient of the material. For boundaries with a disorientation $\theta \geq \theta_0$, the mobility is taken to be equal to the HAGB mobility. Figure 2.6 shows the mobility as a function of disorientation. It is clear that the exponential term in the mobility equation gives the curve a very strong dependence on the disorientation angle between 4° and 14° .

It is seen from equation 2.7 and in Figure 2.6 that the mobility of subgrain boundaries with a disorientation $\theta < 4^\circ$ is almost 0. Humphreys and Hatherly [10] proposed an alternative law for the mobility of subgrain boundaries with very low disorientation ($\theta \rightarrow 0$). In this case, the boundary is made up dislocations that are spaced far enough from each other for the effect of the behaviour of individual dislocations to be dominant. The proposed mobility law is given in equation 2.9.

$$m = \frac{D_s c_j b^2}{4c_1 k T \theta} \quad (2.9)$$

where D_s is the coefficient of self-diffusion, c_j the concentration of jogs, b the magnitude of the Burgers vector, k the Boltzmann's constant, T the temperature, and c_1 is a small constant. According to this equation, the mobility is inversely proportional to the disorientation angle for very low angles. As a result, subgrain boundaries with very low angles of disorientations would have larger mobilities. A schematic curve, given by Humphreys and Hatherly [10], is shown in Figure 2.7.

Equation 2.9 was not used in the simulations for the following reasons:

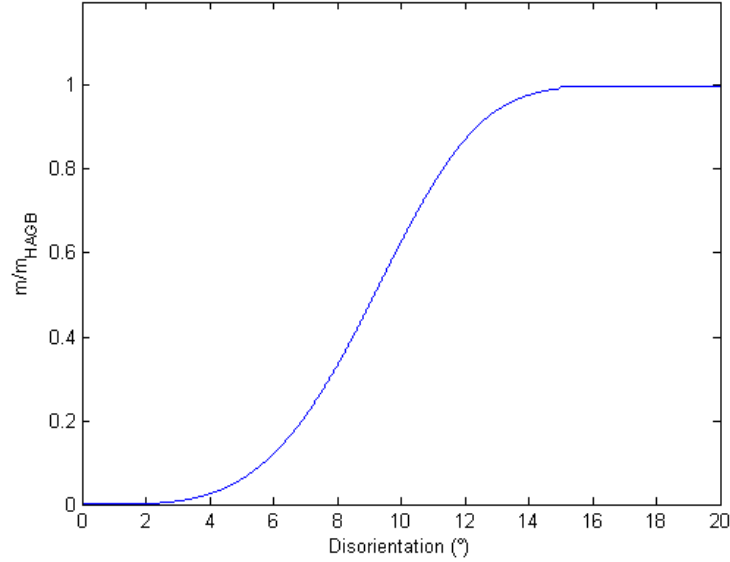


Figure 2.6: Grain boundary mobility as a function of disorientation.

1. It is difficult to measure the mobilities of subgrain boundaries with very low angles of disorientations and therefore hardly any experimental data exists that may provide values to be used in the simulations.
2. A recent study by Winning et al. [39] has looked into the mobilities of low-angle boundaries in pure metals, but the expressions mentioned there correspond to specific cases like symmetrical tilt boundaries, and are thus difficult to apply in the current simulations where the nature of all the subgrain boundaries is taken to be same. Winning et al. have also suggested an equation for the mobility of a generic low-angle grain boundary (LAGB), but its expression is independent of disorientation.
3. In equation 2.9, the jog concentration c_j is unknown. Its value should depend on the disorientation and thus may differ from one subgrain boundary to another, and may also not remain constant during subgrain growth.
4. In the simulations, values of the disorientation approaching zero will result in mobilities approaching infinity. This can be problematic from the point of view

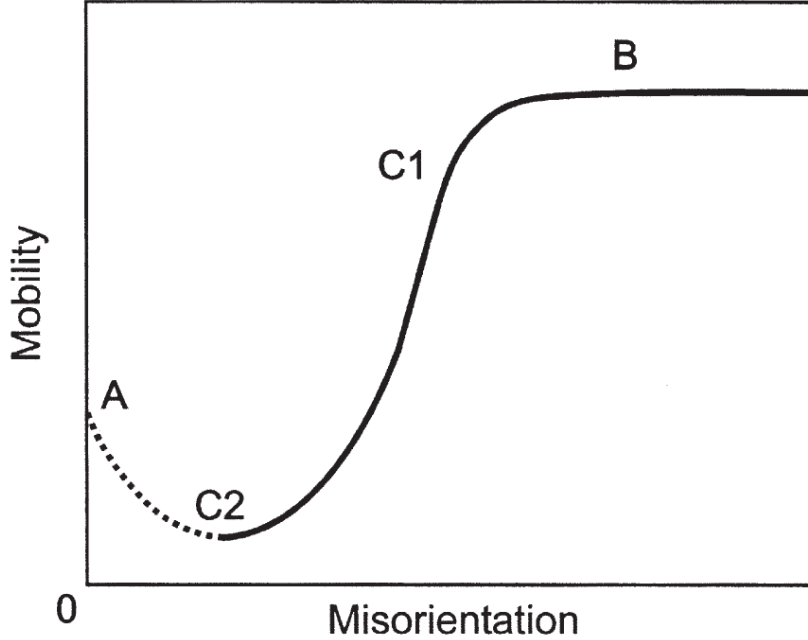


Figure 2.7: Mobility of boundaries as a function of disorientation with modified expression for low disorientation angles (equation 2.9) [10].

of machine precision, and additional rules will have to be introduced to handle such situations.

2.3.4 Topological transformations

The topological changes occurring in the microstructure during grain/subgrain growth are duplicated in the program using the topological transformations. These transformations include the recombination of two triple points, and the disappearance of small triangular and lens-shaped grains [8]. The topological transformations are illustrated in Figure 2.8.

These topological transformations are triggered when a segment becomes shorter than a critical length e . This critical length is defined as a fraction of the average length between virtual vertices.

$$e = 2.5n_{virtual}\Delta \quad (2.10)$$

$$\Delta = \frac{K\langle r \rangle}{1 + n_{virtual}} \quad (2.11)$$

2.3 Principles of the vertex dynamics simulations

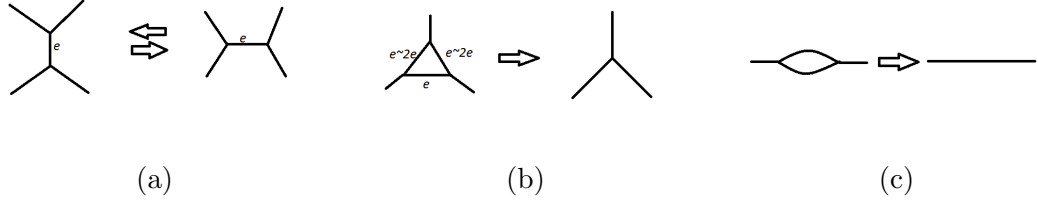


Figure 2.8: Topological transformations (a) Recombination of two triple points, (b) disappearance of a triangular grain and (c) disappearance of a lenticular grain

$$\langle r \rangle = \sqrt{\frac{2A_t}{\pi n_{grains}}} \quad (2.12)$$

Here $\langle r \rangle$ is the average radius of the grains, A_t the total area of the simulation, $n_{virtual}$ the number of virtual vertices on each segment and K is a constant of proportionality. This constant K is a simulation parameter. Choosing smaller values results in higher precision - because topological transformations are triggered at smaller segment lengths - at the cost of speed of execution. The value of K used in the simulations is 0.025 as specified by Weygand et al. [8].

The methods for carrying out the topological transformations in the program are detailed in Appendix B.

2.3.5 Time increment

The big advantage of the vertex dynamics simulations over the Monte Carlo type of simulations of grain or subgrain growth is that vertex dynamics simulations have a well-defined time step that corresponds directly with real-time. There are two kinds of time step used in the simulation:

- Global time increment
- Fast vertices' time increment

2.3.5.1 Global time increment

The time increment has a direct influence on the evolution of the microstructure because it gives us the movement of the vertices by multiplying with the velocity calculated. If the time step is too small, the movement of the vertices will be smaller, and this will slow down the simulation unnecessarily. On the other hand, if the time step is too

2. VERTEX DYNAMICS SIMULATIONS

large, then the vertices may move too far and thus bypass any potential topological operations. This will result in crossed grain boundaries and other similar errors.

In order to avoid these errors, the time increment is calculated for each segment and the vertices on its two ends such that the segment does not change its length by more than a fraction $f = 0.5$. If the two vertices of a segment have the initial position vectors \vec{p}_1 and \vec{p}_2 and final position vectors \vec{p}'_1 and \vec{p}'_2 , the segment before and after movement can be written as r_{12} and r'_{12} where

$$r_{12} = \vec{p}_2 - \vec{p}_1 \quad (2.13)$$

$$\begin{aligned} r'_{12} &= \vec{p}'_2 - \vec{p}'_1 \\ &= r_{12} + (\vec{v}_2 - \vec{v}_1) \Delta t \end{aligned} \quad (2.14)$$

Here \vec{v}_1 and \vec{v}_2 are the velocities of the vertices 1 and 2 and Δt is the time increment. In order to calculate the time increment, the following inequalities are solved:

$$(1 - f) |r_{12}| < |r'_{12}| < (1 + f) |r_{12}| \quad (2.15)$$

The inequalities in 2.15 involve quadratic terms in Δt due to the vector magnitudes and thus have 4 possible solutions. The smallest positive value is chosen as the solution.

It should be noted that at this point, each segment has its own value of time increment. This is because the velocities of the vertices at the extremities of each segment affect the change in length, and thus the value of the time increment.

Next, a fraction of up to $f_{fast} = 0.05$ of the vertices having the smallest Δt values are separated and labelled *fast* vertices. Their treatment is explained in section 2.3.5.2. Among the remaining vertices, the smallest time step is selected as the `globalTimeIncrement` variable which is used for the movement of these vertices. Performing this step speeds up the simulation considerably by separating out the vertices with very high velocities and consequently low time increments.

2.3.5.2 *Fast* vertices

The *fast* vertices are those that have been selected based on their time increments as explained in section 2.3.5.1. For these vertices an alternative time increment is calculated using a different value of the limiting fractional change in segment length.

For the other vertices, this limiting value is taken to be equal to 0.5, while for the *fast* vertices, it is taken to be 0.05. The time increment corresponding to this smaller length change limit is smaller than `globalTimeIncrement` and prevents these vertices from moving too fast and thus bypass any potential topological transformations.

2.3.5.3 Relationship between the Global and Fast time increments

After displacing all the other vertices, the program treats the *fast* vertices. The velocities and time increments for these vertices are re-calculated to check if the motion of the other vertices have modified them. Those vertices that no longer require a time step smaller than the value in `globalTimeIncrement` are removed from the fast list and displaced using their new velocities and the global time increment value. The remaining vertices are moved using their own smaller time increment value, and this value is added to a separate counter variable. When the value of this counter variable reaches the global time increment value, the vertex is removed from the fast list.

The above steps are repeated in a loop until there are no fast vertices remaining. Once in every five iterations of this loop, a check is performed for the topological transformations and they are carried out if necessary.

By this method, the simulations remain quite fast by having a large global time increment, while locally fast-moving vertices are dealt with separately using a finer time step that adds up to the global time increment.

2.4 Validation

Before using the simulations for more complex cases, they must be validated using simpler geometries that can be solved for analytically. This validation is presented in the following sections.

2.4.1 Shrinking polygon

An isolated regular polygon with n sides slowly shrinks till it reaches zero area. The rate of decrease of area is given by equation 2.16 [8].

$$\frac{dA_n}{dt} = -2m_{GB}\sigma n \operatorname{tg}\left(\frac{\pi}{n}\right) \quad (2.16)$$

2. VERTEX DYNAMICS SIMULATIONS

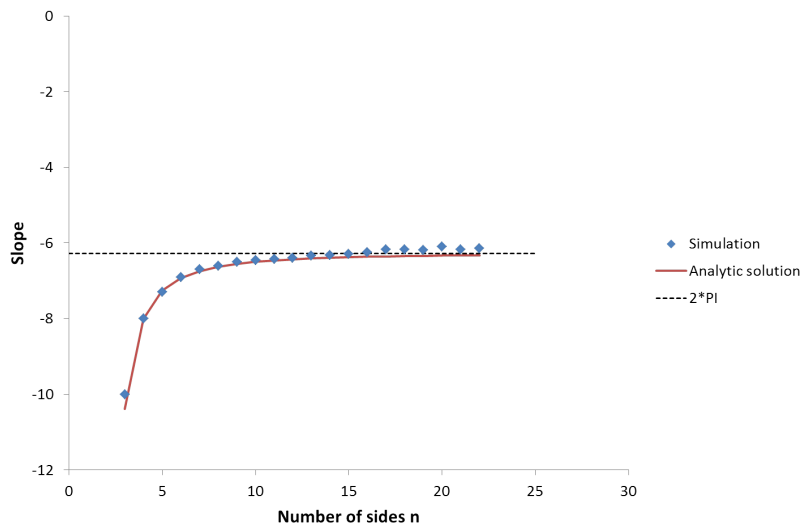


Figure 2.9: Rate of decrease of area in simulations compared with the analytic solution

For the limiting case of a circle, it can be considered to be an n -sided polygon with $n \rightarrow \infty$. The slope is then equal to $-2\pi m_{GB}\sigma$. Simulations of such isolated grains, carried out with m_{GB} and σ taken to be 1 for simplicity, yield the slopes shown in Figure 2.9. Good agreement is seen with the slope values from the analytical expression. It is seen that for $n = 15$ and above, the slope is approximately equal to that for very large n . A shrinking 15-sided polygon and its decrease in area with time are presented in Figure 2.10.

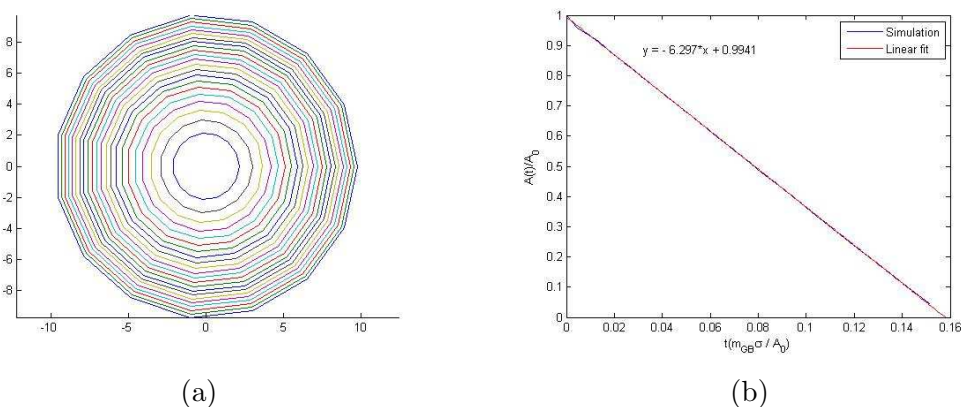


Figure 2.10: (a) Shrinking 15-sided isolated polygon (b) Reduction of area with time for the 15-sided isolated polygon

2.4.2 Von Neumann-Mullins law

The evolution of the area A_n of an n -sided 2D polygon embedded in a frozen microstructure is described by the Von Neumann-Mullins equation:

$$\frac{dA_n}{dt} = \frac{\pi}{3} m_{GB} \sigma (n - 6) \quad (2.17)$$

An example of a 9-sided regular polygon is shown Figure 2.11 and its growth rate is shown in Figure 2.12. It is seen that the slope of 3.2 is close to the value given by the Von Neumann-Mullins law for $n=9$.

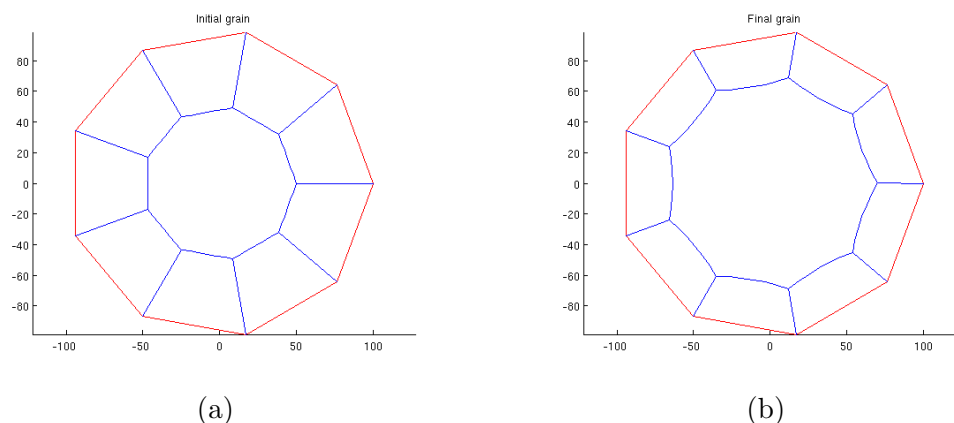


Figure 2.11: Growth of a 9-sided regular polygon embedded in a frozen microstructure: (a) Initial shape (b) Shape after 150 iterations

Figure 2.13 shows that the present simulations, carried out with mobility and energy both taken to be equal to 1 for simplicity, fulfil the Von Neumann-Mullins law for different numbers of virtual vertices used to discretize the grain boundaries.

The number of virtual vertices used for discretizing the grain boundaries must be selected carefully. Using a large number of virtual vertices is expected to improve accuracy, but in the case of short boundary segments, it might do exactly the opposite by causing very high values of boundary curvature in the vicinity of triple points. This would, in turn, make the triple points have high velocities and typically lead to a flip-flop situation at these points where the triple point keeps oscillating about its position at the time when the high curvature first occurred. This problem is solved by

2. VERTEX DYNAMICS SIMULATIONS

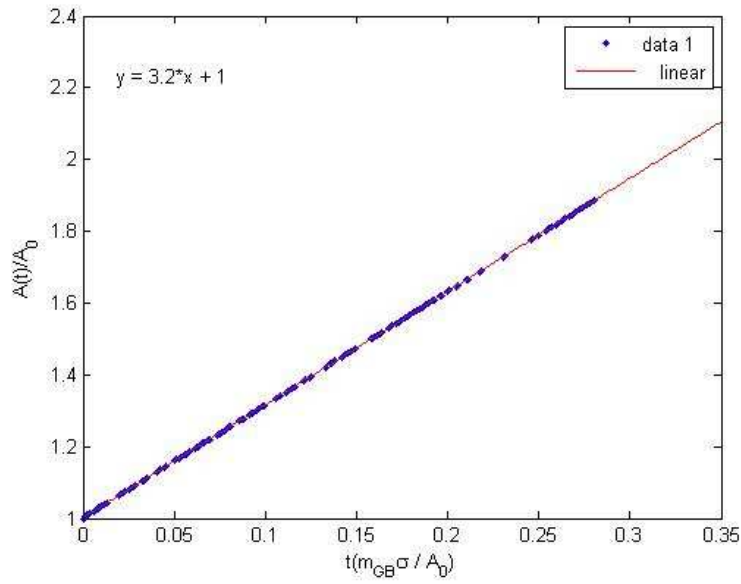


Figure 2.12: Rate of increase of area of the 9-sided polygon shown in Figure 2.11

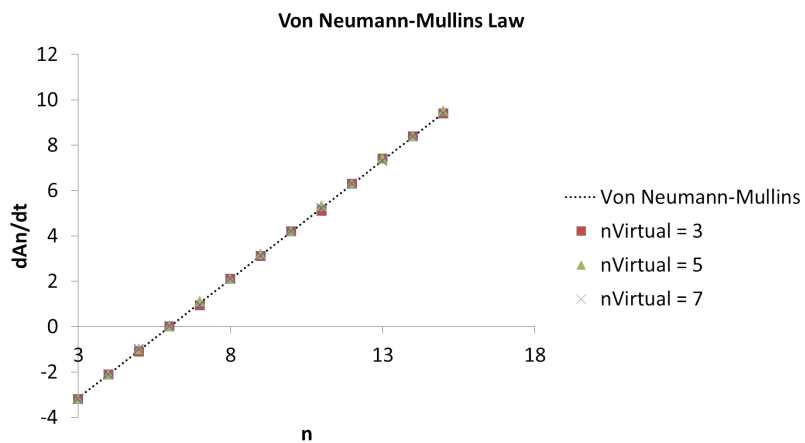


Figure 2.13: Von Neumann-Mullins law is verified by the simulations for an n -sided polygon embedded in a frozen microstructure.

defining a minimum length limit such that all boundaries shorter than this length are not discretized using virtual vertices.

The equations for the simulation have thus been validated for simple cases that can be solved analytically. Therefore, the simulations can now be applied to more complex structures.

2.4.3 Scaling behaviour

In the case of normal grain growth, the increase in the mean grain area is expected to follow the power-law derived by Burke and Turnbull [14]. According to this law, the mean radius is proportional to the square root of time. In other words, the mean area should have a linear dependence on time as seen in equation 2.18.

$$\langle A \rangle (t) = \langle A \rangle (0) + Km_{GB}\sigma t \quad (2.18)$$

A simulation was carried out with all grain boundaries having the same values of mobility and energy, which were equal to the values for high-angle grain boundaries. The increase of mean grain area with time is shown in Figure 2.14. The constant K was found to be equal to 0.96, or approximately equal to 1, in the present simulations as shown in Figure 2.14.

2.4.4 Microstructure

The images in Figure 2.15 show a sample of grain growth achieved using the vertex dynamics program developed in the course of the PhD thesis. The initial structure had 530 grains with a mean size of 30 μm , and a random distribution of orientations. A visual inspection of the microstructures provides for a qualitative validation of the correctness of the simulation.

2.5 Adapting for subgrain boundaries

2.5.1 *Fast* treatment

As explained in section 3.5, the treatment of *fast* vertices is carried out by separating these vertices having high velocities in order to obtain a higher value of the time increment. The detection of the fast vertices is done by pooling the vertices into bins

2. VERTEX DYNAMICS SIMULATIONS

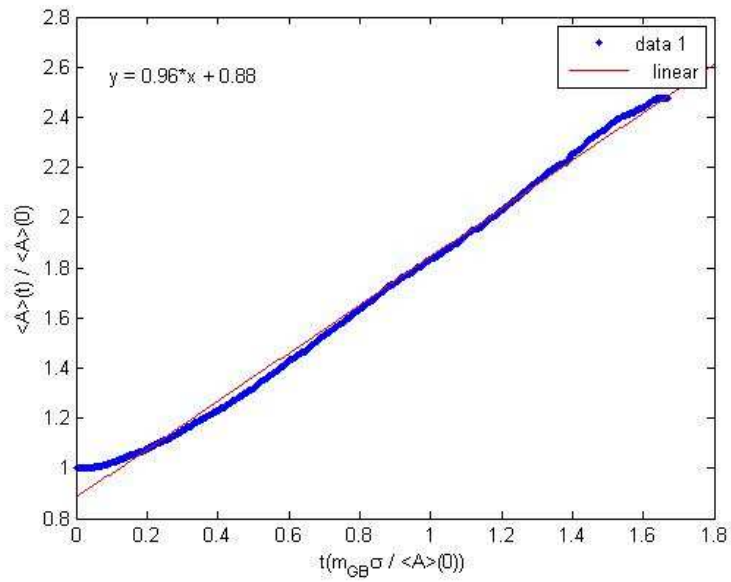


Figure 2.14: Scaling behaviour of mean grain area evolution with time

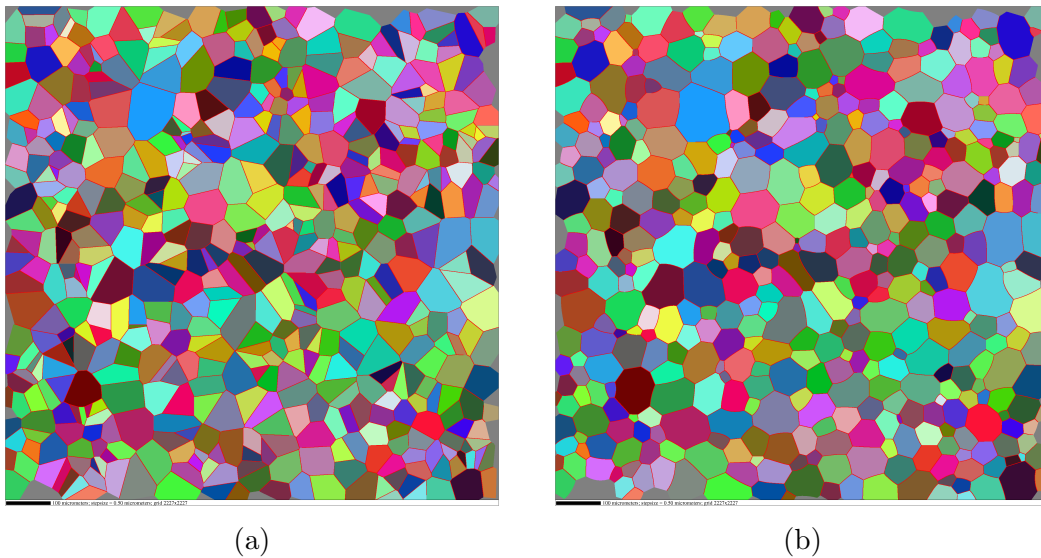


Figure 2.15: Normal grain growth using the vertex dynamics simulation program (a) Initial microstructure generated using Voronoi Tessellation and (b) Evolved microstructure using vertex dynamics

2.5 Adapting for subgrain boundaries

according to their individual time increment values, the number of vertices in the n^{th} bin being the number of vertices having a time increment less than or equal to $10^{-n}s$ with $0 < n < N; n, N \in \mathbf{N}$. The index i of the first bin having at least one and less than the fraction f_{fast} number of vertices gives the global time increment value as $10^{-i}s$, and all the vertices having a time increment less than this value are labelled *fast*.

For grain growth, the value of $N = 10$ yielded satisfactory results. In the case of subgrain growth, the disorientations between subgrains are smaller, resulting in smaller mobilities, energies and thus smaller velocities. This means that for most of the vertices, the time increment value should be large compared to the vertices in a grain growth simulation. Nevertheless, there remain a small number of vertices which have very large velocities. These vertices force the global time increment to remain at small values - typically 10^{-9} s - and this slowed down the simulation considerably for the meagre benefit of managing a few fast vertices.

To avoid this problem, it was decided to use a smaller value of N , i.e., fewer bins. This serves two purposes: first, a larger time increment is obtained allowing the simulation to run faster and second, more vertices fall into the *fast* category which justifies their being treated separately.

It should be noted that having too small a number of bins would be detrimental to the accuracy of the simulation by forcing a large time increment on some vertices having large velocities. It was found that $N = 6$ was sufficiently small for the purpose of subgrain growth - achieving a compromise between speed and precision.

2. VERTEX DYNAMICS SIMULATIONS

3

Experimental Techniques

3.1 Material

This study concentrates on the industrial alloys of the type AA3004. The alloys of this type are used for beverage packaging such as cans, and also for heat exchangers and radiators. Since these service conditions usually involve pressure differences between the inside and outside of the structures, and in the latter case the added influence of heat, softening by recovery is a very pertinent problem for alloys of this type.

A model alloy of Al-0.1% Mn is used because it represents approximately the solid solution matrix of the industrial alloy without the presence of the precipitates. The alloy was furnished by Alcan CRV in the form of ingots for the theses of Quey [40], Barou [2] and Albou [5]. The role of Mn is that it improves the strain hardening of the alloy and also limits the rate of recovery and recrystallization, thus providing more control during the study of the recovery kinetics compared to high-purity Al. The chemical composition of the alloy is presented in Table 3.1.

From the ingot, bars of dimensions 20 mm \times 13 mm \times 150 mm were cut out. Quey [40] reported that these bars only had a weak initial texture (see Figure 3.1). These

Solute (wt%)	Impurities(ppm)							
Mn	Cu	Mg	Si	Fe	Ni	Zn	Ca	Na
0.12	15	2	6	5	0.33	0.23	0.23	1.47

Table 3.1: Chemical composition of Al-0.1% Mn model alloy [5]

3. EXPERIMENTAL TECHNIQUES

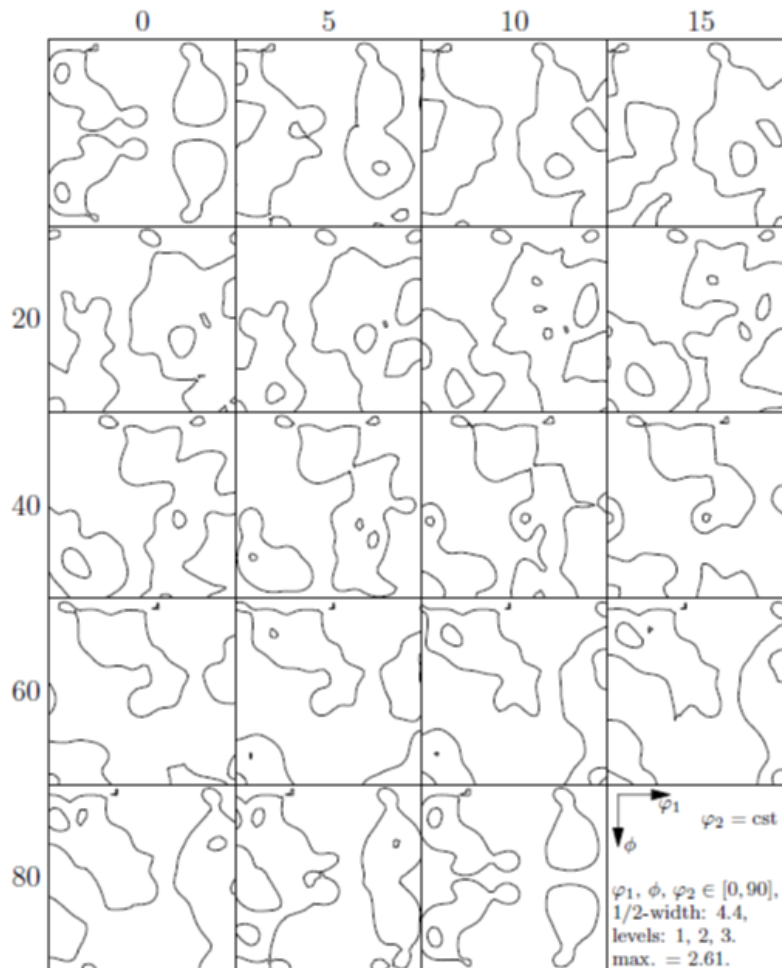


Figure 3.1: Initial texture of the bars of Al-0.1% Mn model alloy [40]

bars were then subjected to the thermomechanical treatment described in section 3.2 and the methods used for their characterization are described in section 3.3.

3.2 Thermomechanical treatment

In order to quantify the kinetics of recovery, severely deformed samples were annealed at different temperatures for different durations and their microhardness was measured. These processes are detailed in the following sections.

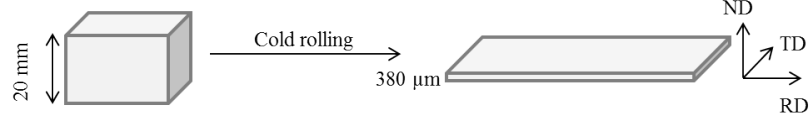


Figure 3.2: Schematic representation of the deformation by cold rolling

3.2.1 Deformation by cold rolling

One bar of the Al-0.1% Mn model alloy was deformed by cold rolling to reduce its thickness from 20 mm to 380 μm , or a true strain of $\epsilon = -\ln\left(\frac{380 \times 10^{-6}}{20 \times 10^{-3}}\right) \approx 3.96$. This severe level of deformation was carried out to enable recovery to proceed readily during annealing. The rolling setup is schematically shown in Figure 3.2. The reduction of thickness was achieved in four passes through the rolls.

Since the metal is severely deformed, it would start to soften by recovery even at room temperature. In order to prevent this, the rolled sheet was stored in a freezer maintained at -23°C . From the rolled sheet, samples measuring 25 mm (along RD) \times 15 mm (along TD) were cut out, taking care to exclude parts of the sample close to the borders of the rolled sheet. These samples were then subjected to annealing at different temperatures and for different durations. Between annealing and microhardness measurements, as well as sample preparation steps, the samples were always returned to the freezer.

3.2.2 Annealing

Four temperatures were selected for the annealing: 130, 160, 190 and 225 $^\circ\text{C}$. They were carried out in an oil bath for the treatments at 130 and 160 and 190 $^\circ\text{C}$, and in an air furnace for 225 $^\circ\text{C}$. This was done because the maximum allowed temperature for the silicone oil used in the oil bath was 200 $^\circ\text{C}$. It is assumed that the large surface area of the samples compared to their thickness causes the temperature to homogenize rapidly, and thus avoid large temperature gradients within the samples.

Both the oil bath and the air furnace were heated up to the required annealing temperature and maintained for at least 48 hours in order to verify the stability of the temperature. The annealing treatments were carried out only after the temperature reached a stable value.

3. EXPERIMENTAL TECHNIQUES

3.3 Characterization

3.3.1 Sample preparation

The sample characterization was performed by microhardness to observe the softening of the alloy and by Electron Back Scattered Diffraction (EBSD) to observe the evolution of the microstructure. For both types of observation, some sample surface preparation is necessary. The observations by EBSD and the microhardness measurements were made on the ND-RD section of the samples.

For this, the samples were cold-mounted in a methacrylate resin mould. This is a nonconducting resin and later proved to be a major obstacle in carrying out observations in EBSD. The conducting resin required hot mounting involving temperatures up to 150 °C. Since the samples' microstructure and mechanical properties are extremely sensitive to temperature, it was decided to use the non-conducting resin to mount the samples.

After mounting, the samples were mechanically polished using SiC abrasive papers with grit sizes of P800, P1200, P2400 and P4000 successively, and finished with 3 μm and 1 μm diamond pastes on felt discs. The state of the sample at this stage can be seen in Figure 3.3.

The quality of the surface produced after mechanical polishing was adequate for the microhardness measurements. For observation by EBSD, an additional step of electrolytic polishing was carried out in an electro-polishing setup Struers LectroPol-5 using the Struers electrolyte A2. The electropolishing parameters are as follows:

- **Voltage:** 10 V
- **Flux:** 12
- **Mask area:** 5 cm²
- **Polishing time:** 25 s

3.3.2 Microhardness

The microhardness measurements were made using a Matsuzawa MXT70 microhardness tester with a Vicker's micro-indenter. The applied load was 25 g with a dwell time of 10 seconds.

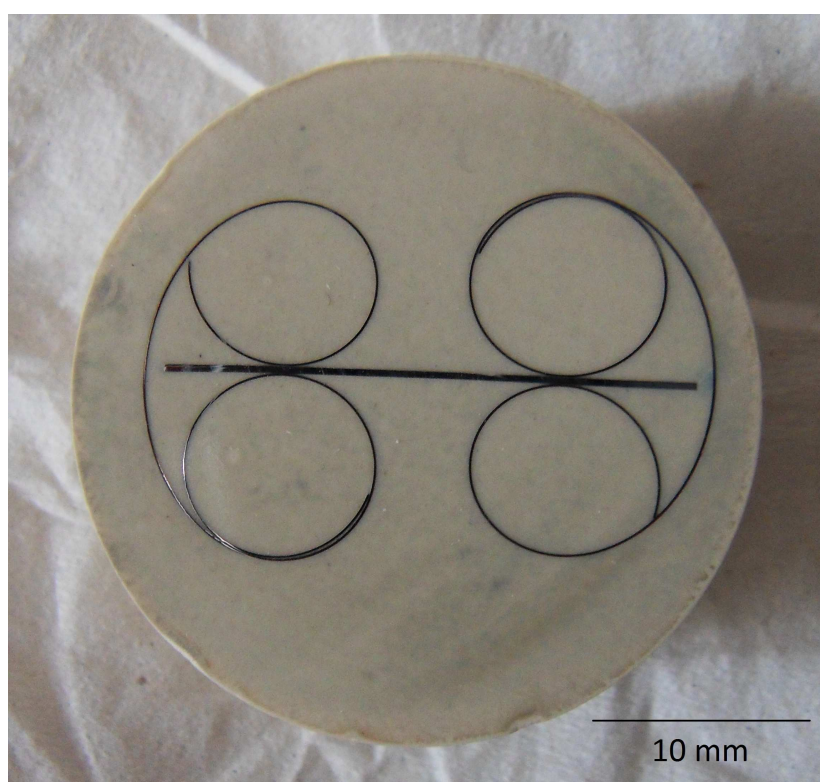


Figure 3.3: The sample after cold-mounting and mechanical polishing. The visible sample surface is the ND-RD face of dimensions $380 \mu\text{m} \times 25 \text{ mm}$. The steel rings are used to hold the sample upright during cold-mounting

3. EXPERIMENTAL TECHNIQUES

The NF A 03-253¹ norms were followed for the microhardness testing. These hardness testing norms indicate that for accurate microhardness measurements for an indentation having a diagonal length of d , the centre of the indentation must be at a distance of $3d$ from the edges of the sample and $6d$ from the centre of any other indentation. The load of 25 g is the largest load that can be applied on these samples while staying within the specifications of the hardness testing norms. Smaller loads produce indentations of smaller size, which results in greater errors in measurement.

The ND-RD face (see Figures 3.2 and 3.3) of the samples was chosen for the microhardness measurements because the maximum elongation of grains as well as their flattening are observable on this face. The width of this face is about 380 μm . The indentations produced by 25 g load had diagonals of length in the vicinity of 30 μm . Since the grains in the undeformed sample had sizes of the order of 1 mm, the deformed structure should have flattened grains that are about 20 μm thick in the ND-RD section. Therefore, the size of the indentation was about the same as the grain size. In order to respect the norms, the required distance from the edges of the sample is 90 μm . However, it was observed that there was a large dispersion in the microhardness values of any sample if the indentation was made anywhere off the central line. This is probably due to the small width of the sample and possible effect of the resin and the steel rings holding the sample. Therefore, care was taken to make the indentations along the central line of the samples, i.e. at approximately 190 μm from the edges, and the sample was displaced by 200 μm between subsequent indentations. For the samples that underwent longer annealing treatments, the indentation diagonal length was close to 35 μm . For these samples, the displacement between subsequent indentations was taken to be 300 μm . Fifteen measurements were made on each sample and the mean and standard deviation were calculated.

3.3.3 EBSD mapping

Electron Back Scattered Diffraction (EBSD) in a Scanning Electron Microscope (SEM) is a technique developed over the last two decades that allows us to determine the crystallographic orientation of individual regions within a microstructure. It is therefore the ideal tool for characterizing the micro texture of a sample.

¹Norme Française enregistrée pour aluminium et alliages d'aluminium, cuivre et alliages de cuivre, April 1972.

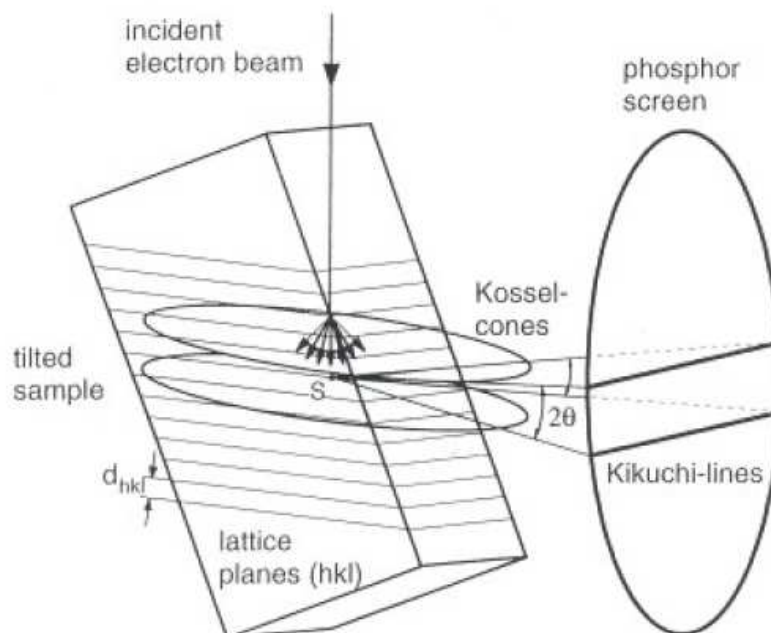


Figure 3.4: Schematic representation of the setup for EBSD [41]

The EBSD technique works on the principle of diffraction of electrons by planes present in the crystal. The electron beam incident at a point on the sample causes the electrons to diffuse into the sample and then scattered by the atoms. The back-scattered electrons are then diffracted by the crystallographic planes when Bragg's law (equation 3.1) is satisfied.

$$2d_{hkl} \sin \theta_{hkl} = n\lambda \quad (3.1)$$

The diffracted electrons form a cone on each side of the set of diffracting planes, with the normal to the planes being the cones' common axis. Inside the microscope chamber, a phosphor screen is placed to detect the diffracted electrons. The schematic representation of the setup described above is shown in Figure 3.4 [41]. The sample is tilted to an angle of 70° to reduce the depth of penetration of the electrons into the sample, and thus maximize the number of electrons backscattered and diffracted towards the phosphor screen.

The intersection of each set of cones with the phosphor screen gives us two hyperbolae which appear as straight lines because the diffraction cones usually have very large

3. EXPERIMENTAL TECHNIQUES

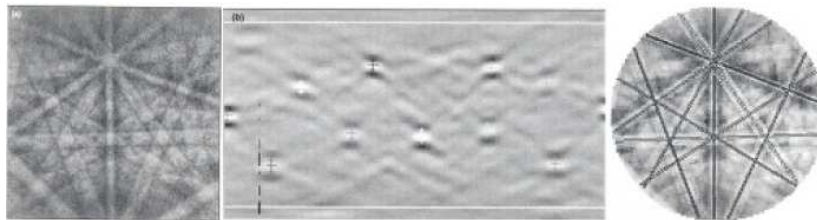


Figure 3.5: An example of a Kikuchi pattern, its Hough transform, and identification of Kikuchi bands [42]

angles and thus are very wide. These lines are known as Kikuchi bands. The central line of each Kikuchi band is in fact the trace of the diffracting plane. When the electron beam is focused on a certain point on the sample surface, several planes diffract, and thus a pattern with many Kikuchi bands is formed. An example of a Kikuchi pattern and the identification of the Kikuchi bands explained later are shown in Figure 3.5 [42].

Next, the diffraction pattern is transformed from the $x - y$ space of the screen plane to the $\rho - \theta$ of Hough space according to the Hough transform shown in equation 3.2. A straight line in the $x - y$ space becomes a point in Hough space with ρ being the perpendicular distance from the origin and θ the angle between the perpendicular to the line and the x -axis.

$$\rho = x \cos \theta + y \sin \theta \quad (3.2)$$

Using the points in Hough space, the Kikuchi bands are identified. The angles between the bands are used to calculate the angles between the corresponding planes by considering the geometry of the setup and the point of incidence of the electron beam. Comparing these angles to lists of interplanar angles for the crystal structure of the sample yields the Miller indices of each plane. Using the Miller indices the crystallographic orientation is calculated.

For carrying out EBSD mapping in this work, A JEOL 6500F SEM-FEG was used, with a voltage of 20 kV at a working distance of 18.1 mm.

4

Kinetics of recovery

4.1 Introduction

Albou et al. [6] have reported that single crystals of Al-0.1% Mn, deformed in plane strain compression and subsequently annealed, show rates of recovery that differ from one orientation to another. The objective of this work is to ultimately carry out simulations of subgrain growth using vertex dynamics in order to explain the causes behind the different recovery rates and attempt to quantify this difference. In order to carry out the simulations, a value of the activation energy for subgrain boundary mobilities in this alloy is required so that they take realistic values in the simulations. Before subgrain growth occurs, two other steps - the arrangement of dislocations into cells, the annihilation of dislocations within the cells - occur [10]. These steps represent different mechanisms and thus the activation energy can be different for each. It should be noted here that Barou et al. [3] have made measurements of sub-grain growth in this deformed alloy by special EBSD techniques but they are delicate and time-consuming. A more general and simpler method was therefore attempted.

This chapter presents an estimation of the activation energy for recovery based on the method of analysis by Vandermeer and Hansen [9]. This method is attractive because it proposes a single kinetic law based on hardness variations that spans the beginning of recovery to the final stages of subgrain growth. Additionally, it is a relatively recent development in the study of recovery kinetics that has not been applied widely. The analysis uses microhardness measurements on samples taken from a cold-rolled sheet of Al-0.1% Mn model alloy, deformed to a true strain of $\epsilon = 3.96$ or 98%

4. KINETICS OF RECOVERY

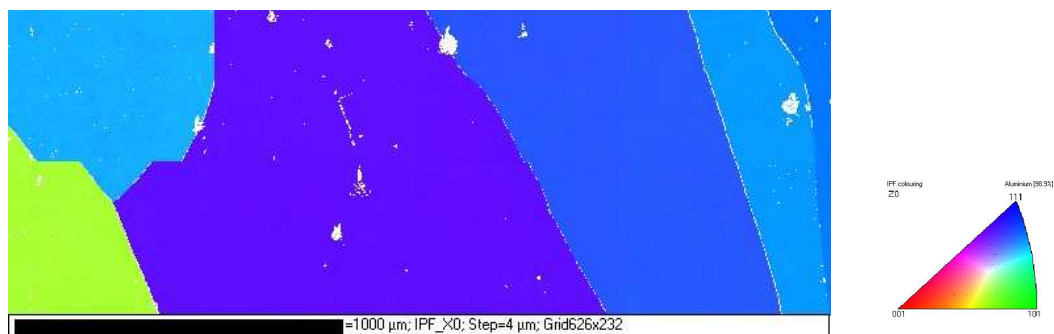


Figure 4.1: EBSD map of the undeformed sample showing part of large grains of size of the order of 1 mm. Non-indexed points are shown in white.

reduction in thickness, which were isothermally annealed at four different temperatures for different durations. Annealing at 130, 160 and 190 °C was carried out in an oil bath, and an air furnace was used for annealing at 225°C. The high value of deformation was selected so that the samples would recover relatively quickly at low temperature values.

4.2 Microstructural evolution during annealing

4.2.1 EBSD mapping

Characterization of the microstructure by EBSD was attempted, but it resulted in rather poor indexation rates for all except the undeformed sample and the samples annealed for the longest duration of 1000 hours at 190°C and 480h at 225°C. These EBSD maps are presented in Figures 4.1-4.3. The colours in the figures represent crystallographic orientations, a legend for which is present in each figure in the form of an inverse pole figure (IPF). The non-indexed points are shown in white on the EBSD maps.

There are two reasons for the poor indexation in EBSD. The first is the very high amount of deformation given to the metal, which results in a highly fragmented microstructure which is harder to index. This problem is not critical for the samples that have started to recover during annealing and indeed for these samples the indexation was better in the beginning of the scans. However, we also encountered beam focusing difficulties which adversely affected the EBSD quality. Due to the temperature sensitivity of the microstructures, it was not possible to mount the annealed samples in

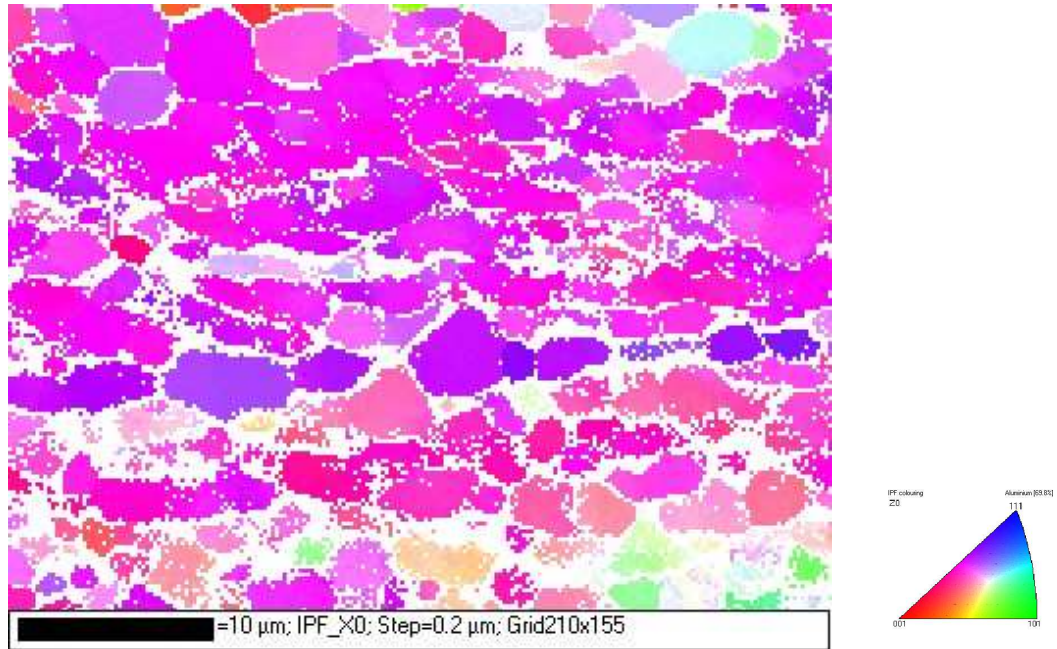


Figure 4.2: EBSD map of the sample annealed for 1000 hours at 190°C. Non-indexed points are shown in white.

a conducting resin which requires hot mounting. They were thus cold-mounted in a non-conducting resin. As a result, there was an accumulation of charges on the surface of the sample during the EBSD mapping, which caused the beam to de-focus.

4.2.2 Microhardness

The microhardness measurements were carried out using a Matsuzawa MXT70 microhardness tester with a Vicker \acute{Z} s micro-indenter. The load applied was 25 g and the dwell time was equal to 10 seconds. The measurements were carried out on the ND-RD face of the samples. Fifteen measurements were made for each sample and their mean and standard deviation were calculated. The results for four annealing temperatures between 130°C and 225°C are presented in Figures 4.4 and 4.5. The points in the figures are the mean of the fifteen measurements and the error bars represent the standard deviation.

The figures present the microhardness values versus annealing time (on a logarithmic scale). For ease of comparison, all the figures share the same scale on both axes. By

4. KINETICS OF RECOVERY

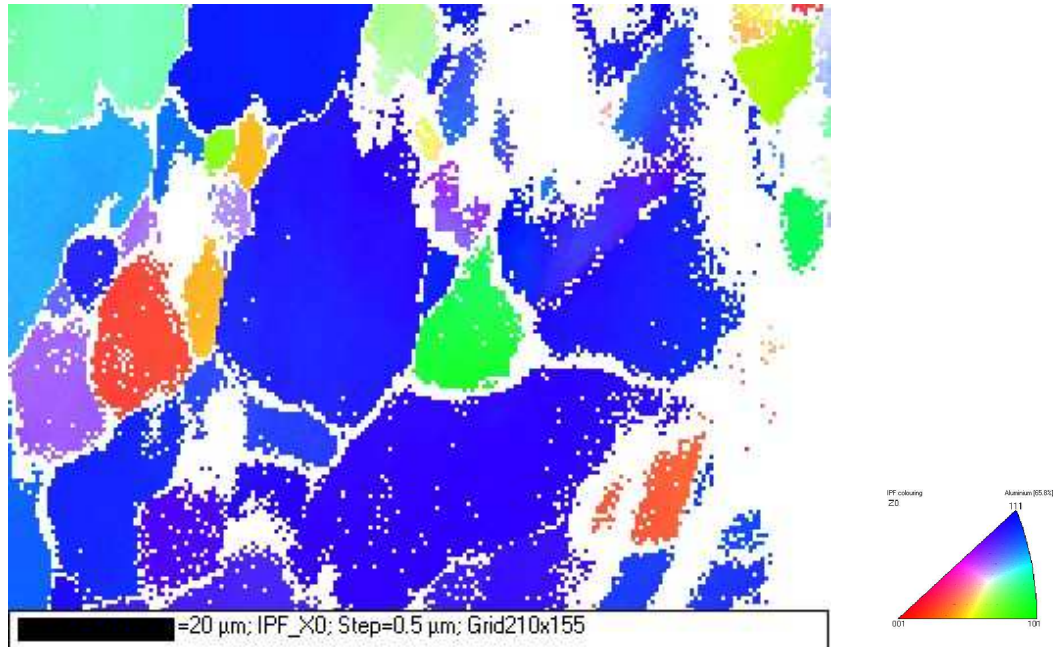
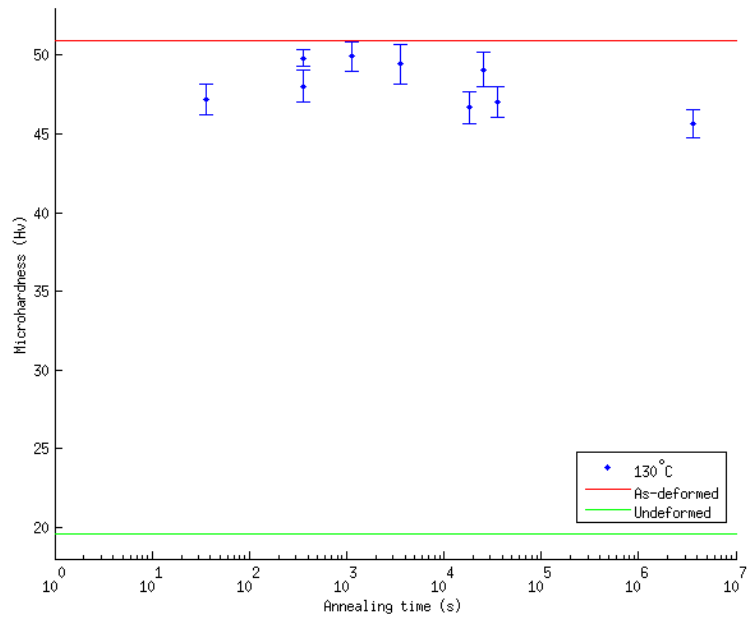


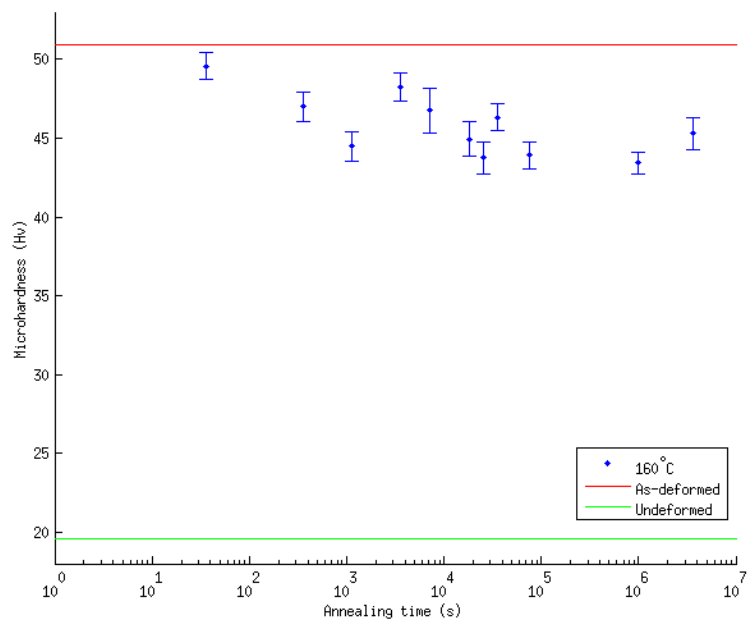
Figure 4.3: EBSD map of the sample annealed for 480 hours at 225°C. Non-indexed points are shown in white.

comparing the figures, it is evident that there is a softening of the deformed alloy with time of annealing at a given temperature. This softening occurs at a higher rate at higher temperatures. It is also seen in the graphs for the samples annealed at 190°C and 225°C, that there is a trend of logarithmic decay of the microhardness with time. However, the results at 225°C show that the samples have recovered more than 50% of the difference between the deformed and undeformed (recrystallized) states. In fact, their hardness values are close to that of the undeformed sample, which was in a recrystallized state. The softening trend is not very clear for the samples annealed at 130°C and 160°C. For the samples annealed at 130°C, there is hardly any softening observed, while for those annealed at 160°C, there is some softening, but the trends are interrupted by the relatively high hardness values observed for the samples annealed for 1 hour and 1000 hours.

4.2 Microstructural evolution during annealing



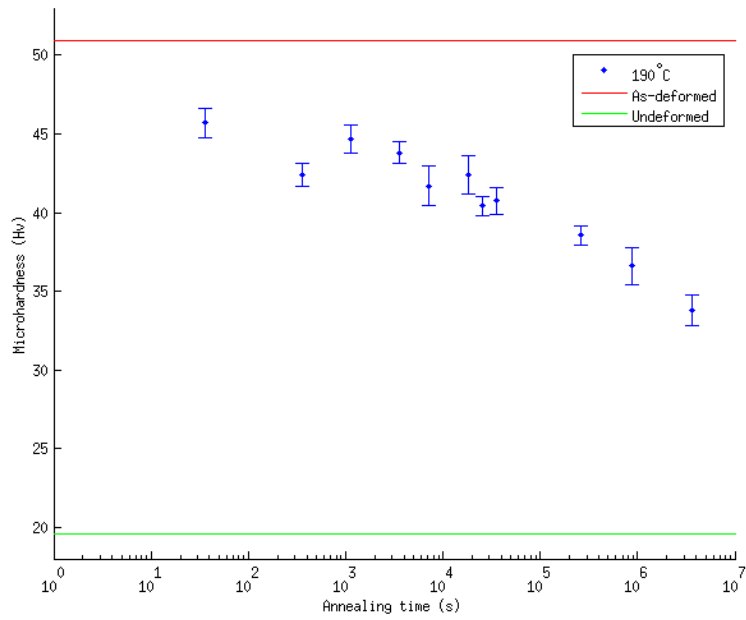
(a) 130°C



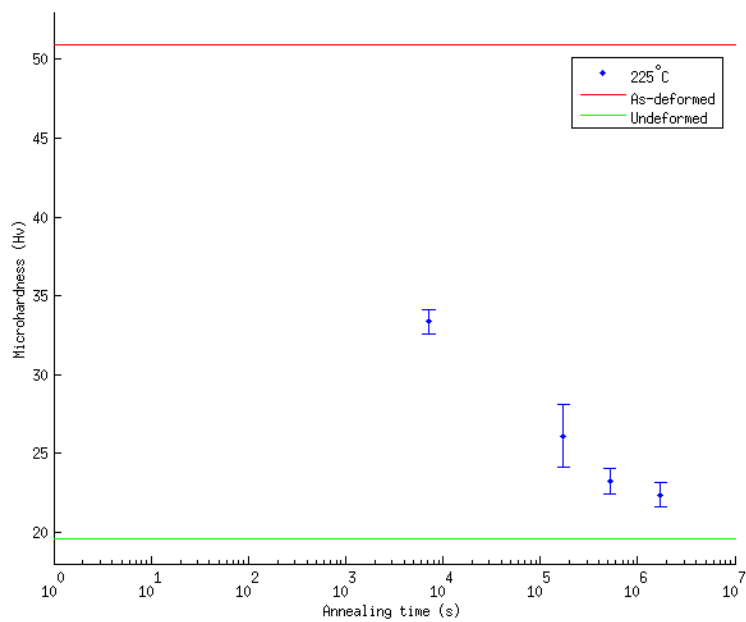
(b) 160°C

Figure 4.4: Microhardness values for annealing at (a) 130°C, (b) 160°C. The error bars represent the standard deviation of the fifteen measurements made for each point.

4. KINETICS OF RECOVERY



(a) 190°C



(b) 225°C

Figure 4.5: Microhardness values for annealing at (a) 190°C and (b) 225°C. The error bars represent the standard deviation of the fifteen measurements made for each point.

4.3 Activation energy for recovery

4.3.1 Analysis method

4.3.1.1 Model equations

The analysis of recovery kinetics proposed by Vandermeer and Hansen [9] was used to estimate the activation energy for recovery from the microhardness data. This analysis method is based on the representation of stored energy as the measure of the progress of recovery, as first proposed by Borelius et al. [18]. This model is based on an earlier model by Kuhlmann-Wilsdorf et al. [17], where the flow stress was used to quantify recovery. The differential equation for the rate of recovery is given in equation 4.1

$$\frac{dP}{dt} = -PK_0e^{-\left(\frac{Q_0-\beta P}{RT}\right)} \quad (4.1)$$

This equation involves a variable activation energy term $(Q_0 - \beta P)$, so that the activation energy is lowest at first in the presence of high dislocation densities and slowly rises towards Q_0 as recovery proceeds. P represents the energy stored in one mole of the metal at time t , and was represented by Vandermeer and Hansen (equation 4.2) in terms of the fractional residual strain-hardening f (defined in equation 4.3).

$$P = P_0f^2 \quad (4.2)$$

$$f = \frac{H - H_r}{H_d - H_r} \quad (4.3)$$

In equation 4.3 H is the hardness of the sample at time t , and H_r and H_d are the hardness values of the recrystallized and deformed states respectively. Replacing P in equation 4.1 with the expression given in equation 4.2, and integrating, Vandermeer and Hansen obtained the kinetic law described in equation 4.4.

$$E_1\left(cf^2\right) = E_1(c) + tt_0^{-1} \quad (4.4)$$

where

$$E_1(x) = \int_{t=x}^{\infty} \frac{e^{-t}}{t} dt = \int_{t=1}^{\infty} \frac{e^{-xt}}{t} dt \quad (4.5)$$

$$t_0^{-1} = K_0e^{-\frac{Q_0}{RT}} \quad (4.6)$$

4. KINETICS OF RECOVERY

and

$$c = \frac{\beta P_0}{RT} \quad (4.7)$$

In equation 4.6, Q_0 is the activation energy that is to be estimated. The other unknown in the kinetic equation is c (equation 4.7), which involves the constant β and the energy stored per mole of material P_0 . Due to the form of the expression of c , these two cannot be separated from each other. However, P_0 can be estimated from the deformation given to the material and this value can be used to obtain an estimate of β once the quantity c in equation 4.4 is evaluated.

The microhardness data appears in equation 4.4 in the form of the quantities (t, f^2) where f^2 is the square of the fractional residual strain hardening at time t . The fractional residual strain hardening is defined in equation 4.3.

The unknown terms in equation 4.4 are t_0^{-1} and c , defined in equations 4.6 and 4.7. Assuming that all terms in these equations are independent of the temperature T , t_0^{-1} and c should be constants for a given temperature. Due to the complexity of equation 4.4, it is not possible to solve analytically for the unknown terms. Therefore, a numerical approach, very recently used by Yu [19], is applied. For each data point (t, f^2) for a single temperature, a curve is plotted in the (c, t_0^{-1}) space by calculating the values of t_0^{-1} for a range of values of c . Next, points of intersection between these curves are calculated; they should provide the characteristic values of t_0 and βP_0 . An example of the resulting graph can be seen in Figure 4.6.

4.3.1.2 Removal of noise from experimental data

From Figure 4.6, it is evident that while there is a grouping of the points of intersection, there are also a few other points that lie far from this group. Further analysis taking all the intersection points results in very poor fitting of the experimental data with the model equation. In a communication with Yu (Materials Department, DTU Risø, Denmark), he informed us that he had faced the same problem. In order to determine the characteristic value of c , he manually selected a point which appeared to be the convergence for the majority of the lines.

In the interest of developing a more general method, it was decided to adopt a statistical approach to exclude points that introduce errors. This method is explained in the following.

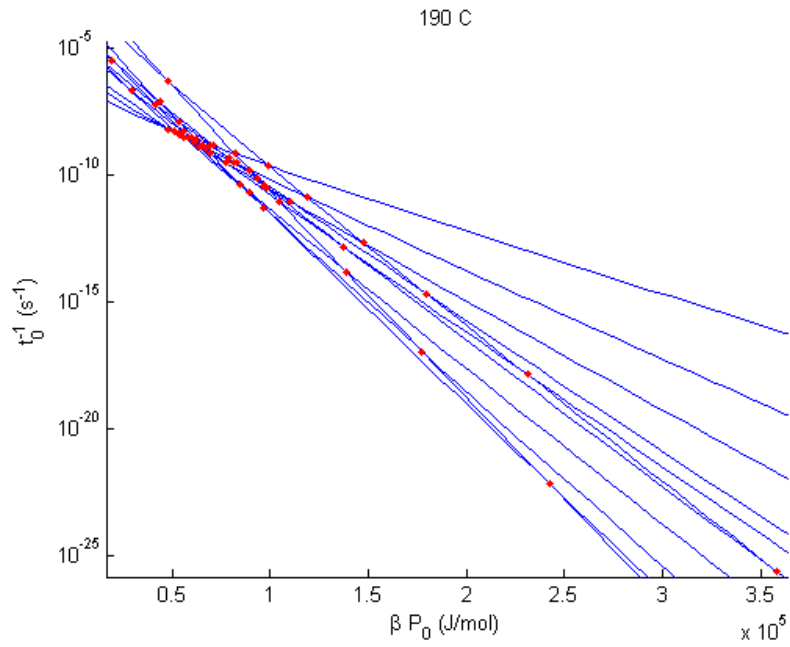


Figure 4.6: Curves (in blue) generated from values of (t, f^2) calculated from microhardness measurements on samples annealed at 190°C , with the points of intersection highlighted (in red)

4. KINETICS OF RECOVERY

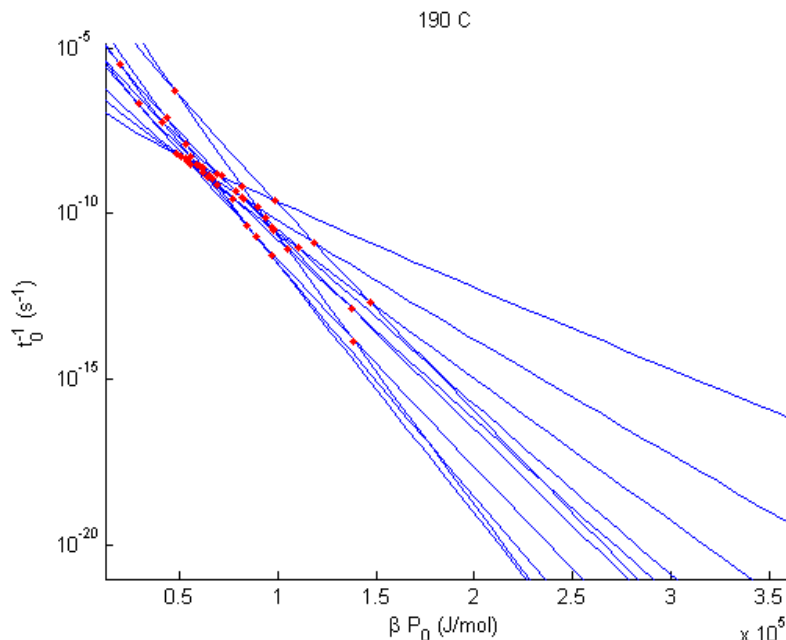


Figure 4.7: Filtered data set after removal of points lying far from the cluster

Since some of these points are rather far away from the cluster in which most of the points lie, they adversely affect the value of the mean convergence point. To avoid this, a recursive scheme is used to remove outlying points one by one, starting from the ones farthest from the mean, until the standard deviation of the new reduced data set becomes less than a fraction p of its mean value. This value of p is determined to be equal to be 1 by iterating through a series of values till the best possible fit (smallest residuals) of experimental data is obtained. This filtering process applied to the dataset of 55 points shown in Figure 4.6 removes five points from the lower right portion of the graph. The resulting graph with the smaller dataset is shown in Figure 4.7.

Once the smaller dataset with a lower standard deviation is obtained, the mean value of c is calculated for this temperature. The same process is then repeated for each temperature.

4.3.1.3 Evaluating the stored energy and activation energy

Using the values of c and their corresponding temperatures, the values of βP_0 are extracted. Since P_0 represents the energy stored in one mole of the metal by deformation, and β is also a constant, βP_0 should be the same for all samples. This constant is taken

4.3 Activation energy for recovery

Temperature ($^{\circ}\text{C}$)	βP_0 (kJ/mol)
130	171.6
160	102.4
190	90.4
225	81.2

Table 4.1: Values of βP_0 estimated from (t, f^2) curves.

Temperature ($^{\circ}\text{C}$)	t_0^{-1} (s^{-1})
130	7.77×10^{-18}
160	1.25×10^{-15}
190	4.99×10^{-12}
225	5.95×10^{-7}

Table 4.2: Mean values of t_0^{-1} calculated for each annealing temperature.

to be equal to the mean of the different values of βP_0 , and the values of $c = \beta P_0/RT$ are re-calculated for each temperature using the mean value.

The new values of c are then used in equation 4.4 to obtain a value of t_0^{-1} for each (t, f^2) at a given temperature. The geometric mean of the set of t_0^{-1} values is calculated to obtain the value of t_0^{-1} for each temperature. The geometric mean is taken because of the large dispersion of these values due to the exponential nature of its expression (equation 4.6). This expression also shows that plotting $\ln(t_0^{-1})$ against $1/T$ should give us a straight line with slope equal to $-Q_0/R$, from which the activation energy Q_0 is estimated.

4.3.2 Results

4.3.2.1 Activation energy

The values obtained for βP_0 , using the method explained above, are listed in Table 4.1. The mean value is 111.4 kJ/mol.

Using this value for βP_0 the values of t_0^{-1} are calculated for each temperature. These values are presented in Table 4.2. These values are plotted against $(1000/T)$ in Figure 4.8 and the slope of the line is used to obtain the value of the activation energy as 440.6 kJ/mol.

4. KINETICS OF RECOVERY

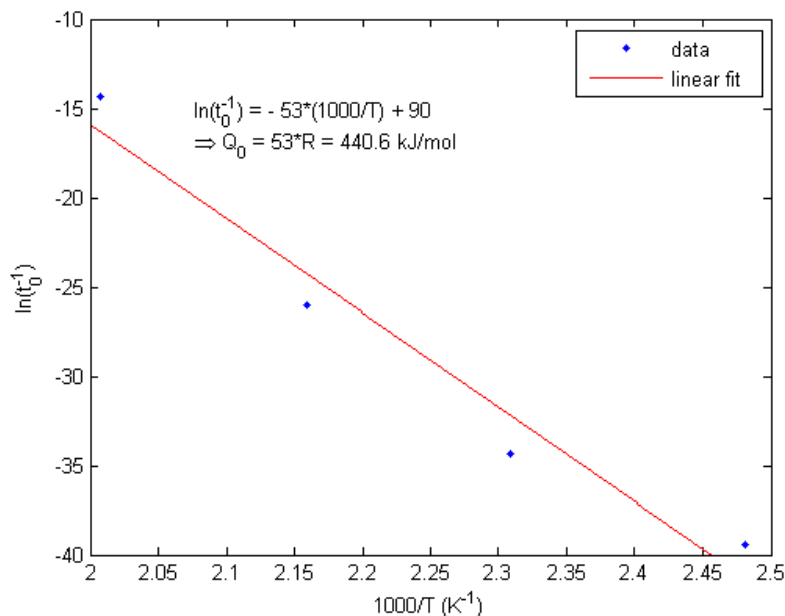


Figure 4.8: Recovery kinetics as a function of temperature - Linear fit performed to estimate the value of the activation energy

With the values of t_0^{-1} and the mean value of βP_0 , the fit of the experimental data with the equation of the form of equation 4.4 is tested. The results are presented in Figure 4.9.

The activation energy of 440 kJ/mol obtained from the analysis of the data is unusually high compared to values for other aluminium alloys published in the literature: from 141 kJ/mol to 196 kJ/mol for AA1050 deformed by cold rolling to true strains of 2 and 4 respectively, 228 kJ/mol for AA1100 deformed by accumulative roll bonding (ARB) to a true strain of 4.2 [19], and 124 kJ/mol for AA1050 cold rolled to true strains of 2 and 4 [9].

Looking at the hardness values of the samples annealed at 225°C (Figure 4.5(b)), it is suspected that these samples have begun to recrystallize. This is also suggested by the equiaxed form of the grain that is visible in the EBSD map of the sample annealed for 480 hours at 225°C (Figure 4.3). Therefore, it was decided that measurements from annealing at this temperature were not representative of recovery, and should be excluded from the analysis.

4.3 Activation energy for recovery

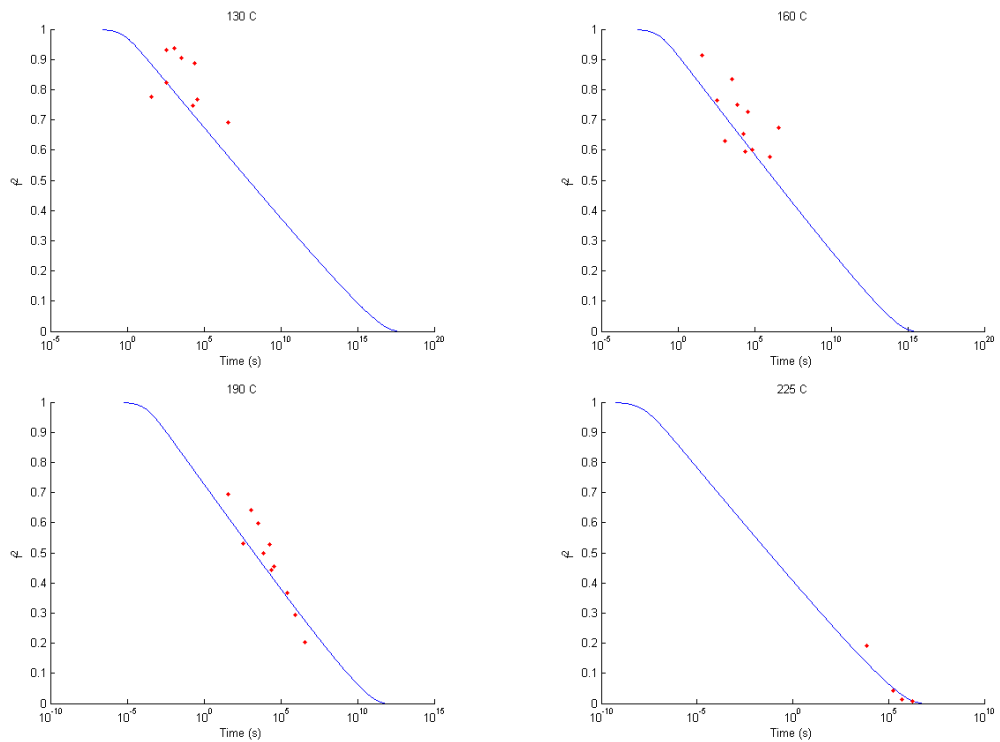


Figure 4.9: Experimental data points (in red) with the model curve (in blue). The model curve is generated using the parameters t_0^{-1} and βP_0 estimated from the experimental data.

4. KINETICS OF RECOVERY

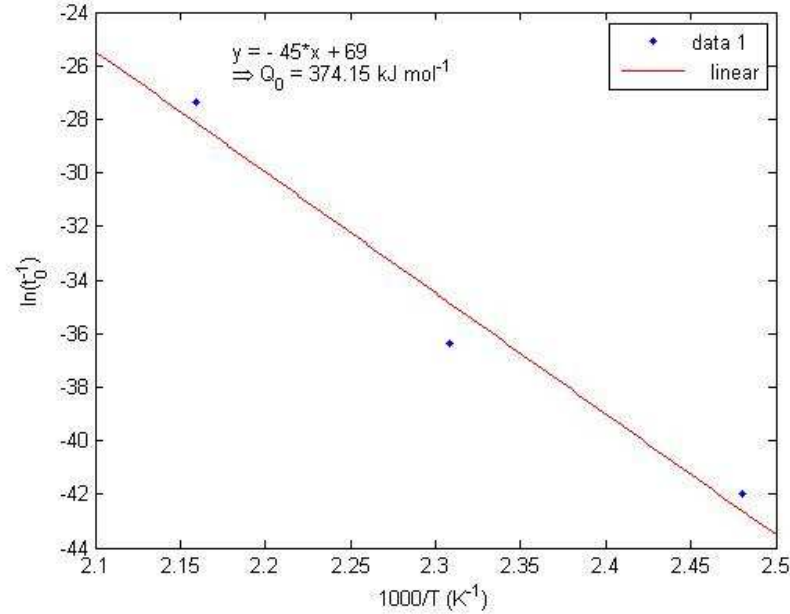


Figure 4.10: Estimate of activation energy for recovery using data from annealing at 130, 160 and 190°C

Repeating the analysis with data from the three lower annealing temperatures yields a value of 121 kJ/mol for βP_0 and 374 kJ/mol for Q_0 . (Figure 4.10)

4.3.2.2 Stored energy

The energy given to the material by means of deformation is stored within it in the form of dislocations. This stored energy per unit volume is expressed in terms of dislocation density in equation 4.8.

$$E = 0.5\mu b^2\rho \quad (4.8)$$

where μ is the shear modulus of the metal, b the magnitude of the Burgers vector and ρ the dislocation density. Evidently, for a greater deformation given to the material, the dislocation density is greater and thus more energy is stored. The relationship between dislocation density and the strain hardening is expressed approximately by the parabolic hardening law in equation 4.9.

$$\Delta\sigma = M\alpha\mu b\sqrt{\rho} \quad (4.9)$$

In the above equation, $\Delta\sigma$ is the strain hardening, M the Taylor factor, and α a geometrical constant equal to the cosine of the angle at which dislocations break through obstacles. The terms μ , b and ρ have the same meanings as earlier. Using the stress-strain curve for the plane-strain compression of Al-0.1% Mn alloys published by Albou et al. [6], and extrapolating to a true strain of 4, the expected flow stress is 175 MPa, and the strain hardening is thus 155 MPa. The values of the other terms in equation 4.9 are taken equal to those used by Albou et al.: $M = 3.31$ for polycrystals, $\mu = 26$ GPa, $b = 2.86$ Å. This gives us the value of dislocation density $\rho = 4.4 \times 10^{14}$ m⁻², and the stored energy per unit volume $E = 468$ kJ m⁻³, or per mole $P_0 = 4.68$ J/mol. From the value of βP_0 estimated earlier, we get $\beta = 2.6 \times 10^4$.

Since the real stored energy is three orders of magnitude smaller than the activation energy, β is expected to take large values if the apparent activation energy is to vary in the course of recovery.

4.4 Discussion

From the results obtained using the Vandermeer analysis, we see that the apparent activation energy Q_{app} for recovery, given in equation 4.10, should start from 253 kJ/mol and keep increasing up to 374 kJ/mol as the material recovers and the stored energy decreases. These values are much higher than the activation energy for the diffusion of Mn in Al, 211 kJ/mol [3].

$$Q_{app} = Q_0 - \beta P_0 \quad (4.10)$$

Barou et al. have applied the logarithmic recovery kinetics law proposed by Nes [13] to estimate the apparent activation energy for recovery based on detailed subgrain size measurements; in the Al - 0.1% Mn model alloy they were found to be in the range of 173 to 194 kJ/mol. The model used in their analysis considers the mechanism of recovery to be dislocation climb in subgrains. The recovery rate is thus controlled by the diffusion of Mn atoms through the Al matrix and the activation energy values reported correspond to the activation energy for solute diffusion. The presence of dislocations in the subgrains introduces stresses into the matrix, which lower the activation energy for solute diffusion. As recovery proceeds, the dislocation density reduces as do the internal stresses, and the activation energy for solute diffusion increases. Good agreement

4. KINETICS OF RECOVERY

Authors	Alloy	Deformation mode	Strain	Activation energy (kJ/mol)
Yu (2011) [19]	AA1050	Cold Rolling	2	141 ± 17
			4	192 ± 5
			5.5	186-196 ± 10
	AA1100	ARB	4.2	228 ± 18
Vandermeer and Hansen (2008) [9]	AA1050	Cold rolling	2	125
			4	124
Barou et al. (2012) [3] Solute-diffusion model [13]	Al-0.1%Mn model alloy	PSC (channel-die)	1.56	186
Majumdar (2013) Present study	Al-0.1%Mn model alloy	Cold rolling	4	374

Table 4.3: Activation energies reported in literature for aluminium alloys [3, 9, 19]

was obtained between the subgrain growth predicted by the model and that measured experimentally.

The activation energy obtained in the present work is also quite high compared to those reported for other aluminium alloys - 186-196 kJ/mol by Yu for cold rolled AA1050 [19], 124 kJ/mol by Vandermeer and Hansen for AA1050 [9], both using the same analysis method as in the present study.

All the values quoted above are represented in Table 4.3.

In the study by Barou et al., the samples were deformed in plane strain compression to a Von Mises equivalent strain of 1.8, which in terms of true strain is equal to 1.56. Using the square-root law in equation 4.9 to determine the flow stress and thus the stored energy, we get the stored energy to be 2.2 J/mol. This results in an activation energy of 243 kJ/mol according to the expression in equation 4.10 and the value of β determined earlier is used with the mean apparent activation energy of 186 kJ/mol.

It should be recalled at this point that the activation energy for recovery is supposed to be a constant value, characteristic of the solute elements, the diffusion of which is expected to be the rate controlling mechanism.

The results obtained by Vandermeer and Hansen give the same value of activation energy for strains of 2 and 4. The value of 124 kJ/mol in their analysis is equal to

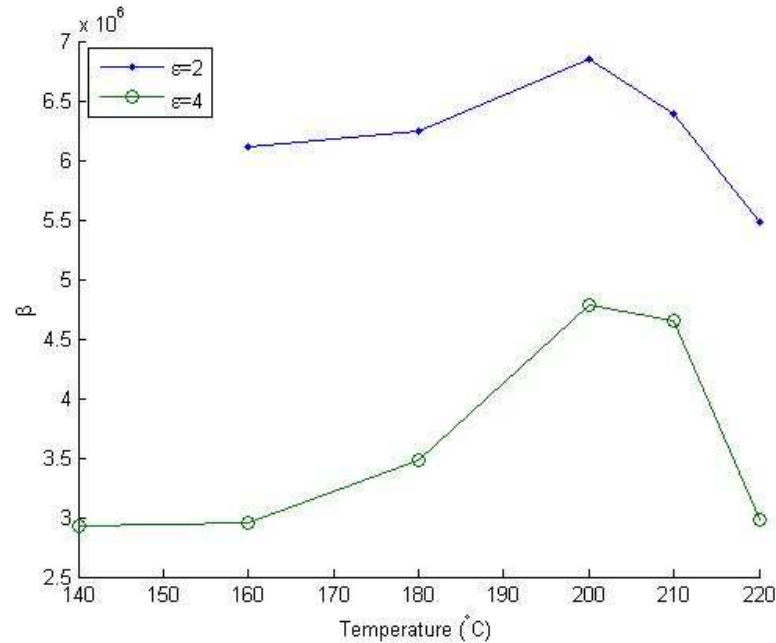


Figure 4.11: Values of β for different temperature and strain values, as presented by Vandermeer and Hansen [9]

that of the self-diffusion of Aluminium. However, Table 1 in their article shows that the quantity $(\beta P_0/RT)$ remained roughly constant for all temperatures and strains. This is inconsistent because the model (equation 4.1) assumes β to remain constant, and the stored energy P_0 should be a constant for a given value of strain, implying that $(\beta P_0/RT)$ must be different for different temperatures. Using approximate values of the stored energies corresponding to the strains of 2 and 4, the values of β were calculated from Table 1 of Vandermeer and Hansen [9]. These values are plotted against temperature in Figure 4.11 and it is seen that, as expected, β is not constant in their analysis. Therefore, the constant activation energy obtained in this study is probably erroneous resulting from the fact that $(\beta P_0/RT)$ was taken to be a constant.

In Yu's PhD thesis [19], the analysis of the method developed by Vandermeer and Hansen was improved upon. A single value of βP_0 was calculated for each strain. This was done by manually selecting the point of convergence of curves in a graph of the type of Figure 4.6. The numbers presented in Table 4.3 show that, for AA1050, the activation energy values calculated by Yu increase with increasing strains. The values for strains 4 and 5.5 for AA1050 are close the activation energy for the diffusion of Fe

4. KINETICS OF RECOVERY

in the bulk Al matrix.

It should also be noted that both analyses study the same AA1050 alloy deformed by the same method of cold rolling. Yet the activation energies calculated by the two authors are quite different.

In the present analysis, precautions were taken to avoid any of the errors mentioned earlier. An improvement was made over Yu's method of manually selecting the convergence points (Figure 4.6) by applying a statistical filtering of the data set to only include points that are clustered together. In spite of these, the activation energy obtained is very different from that reported Barou et al., and is in fact uncharacteristically high for an aluminium alloy of its kind.

4.5 Conclusions

In light of the above results and comparisons, it is concluded that the recent model by Vandermeer and Hansen, though elegant in form and based on relatively simple microhardness measurements, poses several difficulties in practice. These are due to the following sources of error:

- The complexity of the kinetic law (equation 4.4) and the number of unknowns render the problem impossible to solve analytically. A numerical approach is therefore necessary, which introduces errors due to approximations.
- The model contains two constants - β and K_0 - that represent the dominant recovery mechanism. However, it has been established that there are several processes that occur, concurrently or consecutively, during recovery [10]. Therefore, the two aforementioned constants should, in fact, not be constant and change as recovery proceeds. This is demonstrated by the fact that even the simple expression for the apparent activation energy (equation 4.10) results in different values for different strains [19]. This adds further complexity to the already complex model equation.
- The model equations contain terms expressed as exponential integrals. Any uncertainty in microhardness measurements are greatly amplified in these exponential terms when they are used in the model equations.

- The progress of recovery is expressed in terms of microhardness. This method is sensitive to the form of the samples, especially when the sample size is small. This is the case for the highly deformed samples that were used in this study where the standard deviation of the measurements on some samples were found to have large values (see Figures 4.4 and 4.5).

It is therefore decided that the activation energy for the Al-0.1% Mn model alloy, to be used for the vertex dynamics simulations that follow, will be taken to be 190 kJ/mol, reported by Barou et al. [3].

4. KINETICS OF RECOVERY

5

Simulation of subgrain growth

5.1 Introduction

It is well known that crystallographic orientation has a strong effect on the mechanical properties of a metal. Consequently, the deformation microstructure depends strongly on crystallographic texture [10]. It has also been noted that the annealing behaviour is dependent on the crystallography. Xing et al. [4] have shown that in the commercial purity aluminium alloy AA1200, structural coarsening during annealing depended on the local texture. In their analysis, the microstructure of the rolled samples consisted of lamellar bands with 70% typical rolling texture components, like Brass and S and Copper, and 30% other texture components. When annealed at temperatures of 200°C and above, heterogeneous coarsening was observed - subgrains lying close to the boundary between lamellae grew and became more equiaxed while those far from the boundary did not grow. It was also observed that lamellae consisting of rolling texture components showed less coarsening compared to those having other texture components. This difference was attributed to the high mobilities of the lamellar boundaries due to their high misorientation.

In order to study more specifically the effect of crystallographic orientation on the rate of recovery, Albou et al. [6] deformed single crystals of an Al-0.1%Mn model alloy in plane-strain compression in a channel-die up to a true strain of 2.3, and then annealed them at different temperatures for different durations. The orientations selected were the ones typically encountered in the rolling texture - Goss $\{110\}\langle 001\rangle$, Brass $\{110\}\langle 112\rangle$ and S $\{123\}\langle 634\rangle$. It was reported that during annealing of the deformed

5. SIMULATION OF SUBGRAIN GROWTH

samples, both Goss and S showed significant subgrain growth while the Brass oriented crystals exhibited very little subgrain growth. In the article, the difference in recovery rates was attributed to the deformation microstructures and the resulting difference in the disorientation distributions.

Vertex dynamics simulations of grain and subgrain growth are a very appropriate tool to study the effect of microstructural parameters such as disorientation and subgrain size on the rate of recovery. Hence, it was decided to carry out simulations of annealing and try to reproduce the experimental results. If the similar behaviour is found in the experiments and simulations, this would validate the proposition of the disorientation distributions being the cause of different rates of recovery.

In this chapter, the results of simulations of subgrain growth with microstructures matching those of the deformed single crystals are presented. The simulations represent the stage of subgrain growth that takes place when most of the dislocations annihilations have already taken place. The results from the simulation are compared with those from experiments carried out by Albou et al., and an explanation is provided for the observations.

5.2 Material properties

The material of interest is an Al-0.1%Mn model alloy that represents the solid state matrix of the alloys of the AA3XXX series. The subgrain boundary mobility and energy used in the simulation are the following:

- Boundary mobility pre-exponential term: $m_0 = 2.71 \times 10^{12} \mu\text{m}(\text{MPa}\cdot\text{s})^{-1}$ [35]
- Boundary energy: $\gamma_{HAGB} = 0.324 \text{ Jm}^{-2}$ [3]

An attempt was made, using the recovery kinetics proposed by Vandermeer and Hansen [9], to estimate the activation energy for recovery of the alloy. The approach and the results are presented in chapter 4, Kinetics of Recovery. The values obtained from this analysis were found to be unreasonably high. It was thus decided to take the mean apparent activation energy value of $Q_0 = 190 \text{ kJ/mol}$ calculated by Barou et al. [3] using the logarithmic kinetic law described by Furu et al. [16] and Nes [13]. This value is not very far from the activation energy of $Q_0 = 136 \text{ kJ/mol}$ reported by Lens

et al. [35] using the variation of grain boundary mobility with temperature and is also coherent with the solute diffusion controlled mechanism of recovery.

The EBSD images published by Albou et al. [6] showing significant differences in subgrain growth between Brass, Goss and S oriented crystals were of samples annealed at 264°C for 34 hours. This temperature was selected for the simulations as well.

The temperature and the activation energy affect the value of the subgrain boundary mobility. The expression for the subgrain boundary mobility used in the simulations, and its value based on the material properties, activation energy and temperature mentioned earlier, are given in equation 5.1. In the equation, θ is the subgrain boundary disorientation (in degrees) and $\theta_0 = 15^\circ$ is the high-angle grain boundary (HAGB) disorientation. The pre-factor of $m_0 e^{-Q_0/RT} = 6.58 \times 10^{-4} \mu\text{m}(\text{MPa}\cdot\text{s})^{-1}$ in equation 5.1 is extremely small, and the final mobility will be still smaller as the term involving the disorientation is bounded between 0 and 1. Therefore the subgrain boundary velocities are expected to be extremely small.

$$\begin{aligned} m &= m_0 e^{-Q_0/RT} \left[1 - e^{-5(\theta/\theta_0)^4} \right] \\ &= 6.58 \times 10^{-4} \left[1 - e^{-5(\theta/15)^4} \right] \mu\text{m}(\text{MPa}\cdot\text{s})^{-1} \end{aligned} \quad (5.1)$$

The subgrain boundary energy is expressed using the Read and Shockley expression (equation 5.2) and therefore it depends only on the boundary disorientation [12].

$$\begin{aligned} \gamma &= \gamma_0 \left(\frac{\theta}{\theta_0} \right) \left[1 - \ln \left(\frac{\theta}{\theta_0} \right) \right] \\ &= 0.0216\theta [3.71 - \ln \theta] \text{Jm}^{-2} \end{aligned} \quad (5.2)$$

Equations 5.1 and 5.2 represent the mobility and energy of subgrain boundaries, i.e., boundaries having disorientation less than 15°. Any boundary having a higher disorientation value is treated as a HAGB and its mobility and energy are taken to be $6.58 \times 10^{-4} \mu\text{m}(\text{MPa}\cdot\text{s})^{-1}$ and 0.324Jm^{-2} respectively.

An estimation of the HAGB velocity using equation 5.3, with curvature equal to 10^6m^{-1} for subgrains with a radius of the order of $1 \mu\text{m}$, gives a velocity of 2.13Ås^{-1} . In the simulations, the velocities of the subgrain boundaries are expected to be at least 2 to 3 orders of magnitude smaller because of their lower disorientation, and also due to drag effect of neighbouring subgrain boundaries.

5. SIMULATION OF SUBGRAIN GROWTH

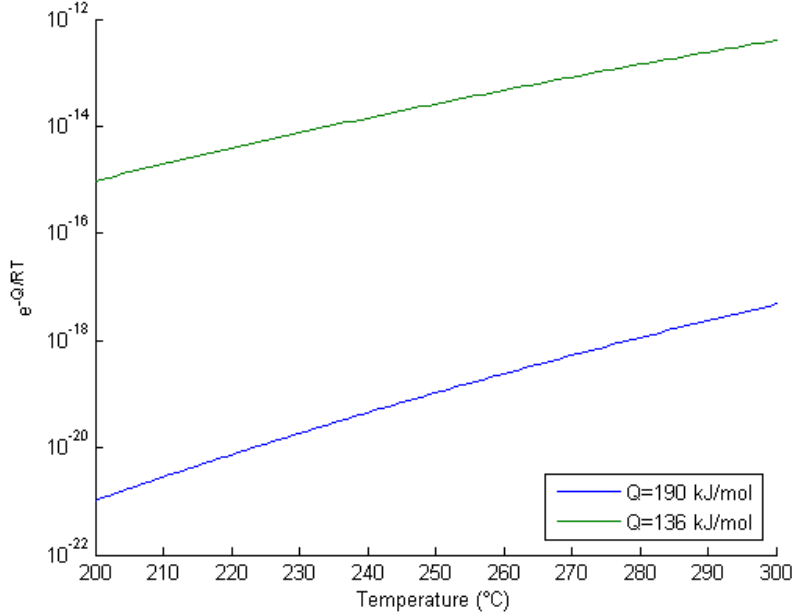


Figure 5.1: Curves representing the change in the scaling of mobility with temperature for two values of activation energy

$$v = m\gamma\kappa \quad (5.3)$$

As a result, the microstructures in the simulations did not evolve even after several hundreds of thousands of iterations representing annealing times of the order of 100 hours. Therefore, in order to demonstrate the reason for the difference between the Brass and Goss recovery rates, the lower activation energy of 136 kJ/mol, estimated by Lens et al. [35], was used in the simulations. Figure 5.1 shows that by using this lower value of activation energy, the mobility is increased by a factor of 10^5 for the temperature of 264°C which was used in the experiments and the simulations.

5.3 Deformation microstructures

5.3.1 Experimental results

Apart from the crystallographic orientations, the major difference between the deformed single crystals is the deformation microstructure. These microstructures from the three

5.3 Deformation microstructures

deformed crystals are shown in Figure 5.2. Line scans on these structures, depicting disorientation with respect to the initial point are presented in Figure 5.3.

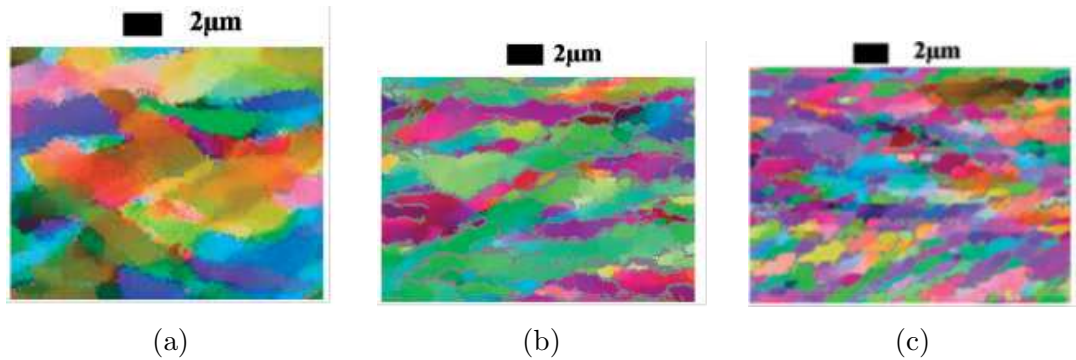


Figure 5.2: Deformation microstructures in the ND-RD section in (a) Brass, (b) Goss and (c) S single crystals deformed plastically to $\epsilon = 2.3$ in plane-strain compression in a channel-die [6]. The colours indicate crystallographic orientation.

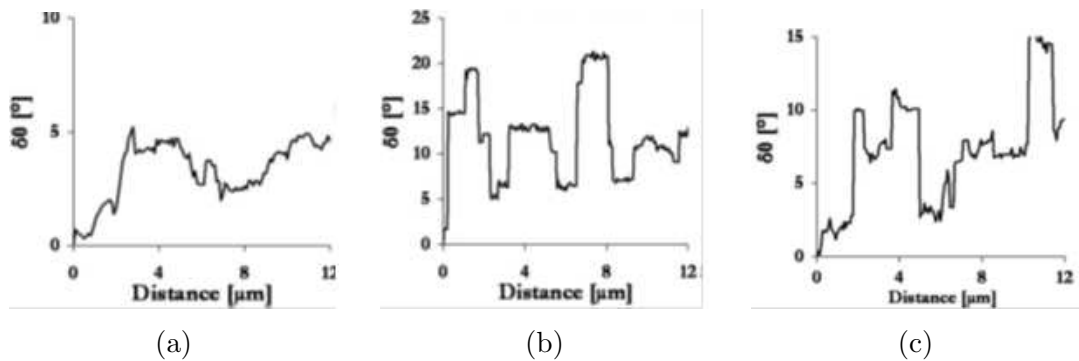


Figure 5.3: Disorientation along a line, with respect to an initial point, in (a) Brass, (b) Goss and (c) S deformed structures presented in Figure 5.2 [6].

The Brass crystal shows a rather uniform spread of orientations around the principal Brass orientation. There is a slight tendency towards bands, but it is not very clearly formed. The mean disorientation with respect to an initially selected point is found to be 3-4°. There was no clear disorientation axis.

The Goss crystal has very clearly formed bands, which have alternating orientations - note the alternating green and purple colours. A scan of disorientations with respect to an initial point shows that the bands are composed of orientations that are typically

5. SIMULATION OF SUBGRAIN GROWTH

displaced by $\pm 10^\circ$ with respect to the principal Goss orientations. The disorientation axis was found to be close to the normal to the rolling plane (ND).

The S crystal also shows bands near the bottom of the structure in Figure 5.2(c), but in the other parts of the structure it is not very clear. The disorientation scan shows plateaus of zones disoriented between 5 and 15° with respect to the initial point. Similar to the case of the Brass crystal, no single disorientation axis was observed.

For the purpose of carrying out simulations of subgrain growth, the Brass and Goss orientations were selected, the S deformation structure being too complicated to reproduce.

5.3.2 Crystal plasticity

Crystal plasticity simulations were carried out with the aim of obtaining a more precise range of disorientation angles and axes for the two selected orientations. For this, the crystal plasticity simulation program `cryplas`, built by Romain Quey on top of the basic crystal plasticity code by Claire Maurice, was used.

The simulations were carried out for an FCC metal with rigid-plastic type of behaviour. A strain tensor corresponding to plane-strain compression (equation 5.4) was imposed and a full constraint Taylor model simulation was carried out.

$$\epsilon = \begin{bmatrix} e & 0 & 0 \\ 0 & 0 & 0 \\ 0 & 0 & -e \end{bmatrix} \quad (5.4)$$

For both Brass and Goss, input orientation lists were created with 1000 crystallographic orientations uniformly spread around the principal orientations and disoriented by at most 2° . The program `cryplas` calculates the grain rotations for each orientation and returns the new orientations in a separate file.

For simulations of plane-strain compression up to a true strain of 2.3, the resulting orientation sets are plotted in the pole figures in Figure 5.4.

It was found that, similar to the experimental results, there was a uniform spread of orientations for the Brass crystal while the Goss crystal showed orientations displaced from the principal orientation by rotations around the normal direction. The maximum disorientation in the case of Goss was also greater than for Brass. The orientation

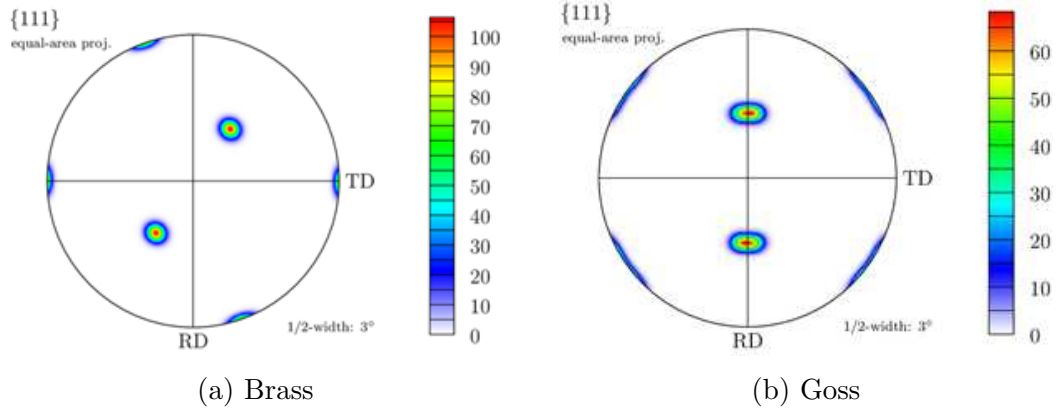


Figure 5.4: $\{111\}$ pole figures of orientation spreads resulting from crystal plasticity simulations of plane-strain compression up to a true strain of 2.3 for (a) Brass and (b) Goss

lists obtained from these crystal plasticity simulations were used for generating the microstructures for input to the vertex simulations.

5.3.3 Input microstructures for the vertex dynamics simulations

5.3.3.1 Parameters for generating input microstructures

Generating the input microstructures for the vertex simulations requires the following parameters:

1. Mean cell size
2. Crystallographic orientation spread - disorientation angles and axes
3. Spatial distribution of orientations

The experimental results give us all three of the above parameters. The results from the crystal plasticity simulations gave similar orientation spreads and the disorientation axes. Therefore, the information at hand at this point was sufficient to generate the deformation microstructures of the Brass and Goss crystals.

5.3.3.2 Colour-coded representation of orientations

In order to distinguish the orientations of different subgrains and grains in a given microstructure, or across separate microstructures, a colour-code is commonly used to

5. SIMULATION OF SUBGRAIN GROWTH

represent the orientations. There exist many conventions for this representation. In these simulations, a colour-code based on Rodrigues' vector of rotation is used.

Rodrigues' vector describes a rotation from one crystallographic orientation to another using a rotation of an angle θ about an axis given by a unit vector \vec{r} . Taking the initial orientation as one in which the crystal's reference frame coincides with the sample's reference frame, the final orientation can be represented unambiguously using the (θ, \vec{r}) pair.

The microstructures from the simulations are generated using the Rodrigues' vector representation of the orientations. For each subgrain, the (θ, \vec{r}) pair corresponding to its orientation is calculated. Next, the vector $\vec{R} = \text{tg}(\theta/2) \vec{r}$ is evaluated. The three components of \vec{R} are scaled to fit in the range of the values representing the red, blue and green channels of the image - 0 to 255 in this case. In this way, each orientation is represented by a unique colour.

Due to the symmetry inherent in the cubic crystal system, there are certain cases in which a single orientation results in several different colours. When such cases are detected, one of the resulting colours is chosen, and the others are replaced by this one.

The orientation calculations and the generation of the images are done using the package `Hermes` developed by Romain Quey.

5.3.3.3 Brass orientation

The Brass deformation microstructure having 5000 subgrains and periodic boundary conditions was generated with a mean cell size of $5 \mu\text{m}$ and a uniform spread of orientations, disoriented by at most 4° from the principal orientation, is given. The resulting microstructure is shown in Figure 5.5.

5.3.3.4 Goss orientation

The Goss deformation microstructure having 5000 subgrains and periodic boundary conditions - identical to the Brass structure in terms of subgrain shapes - was generated with a mean cell size of $5 \mu\text{m}$. Two pools of orientations are created - one with orientations resulting from rotations between $+5$ and $+10^\circ$ around the axis normal to the rolling plane, and the second resulting from rotations between -5 and -10° . The orientations are then assigned depending on the position of the centroid of the cells. In alternating bands of $20 \mu\text{m}$, the orientations are taken from one pool for cells with

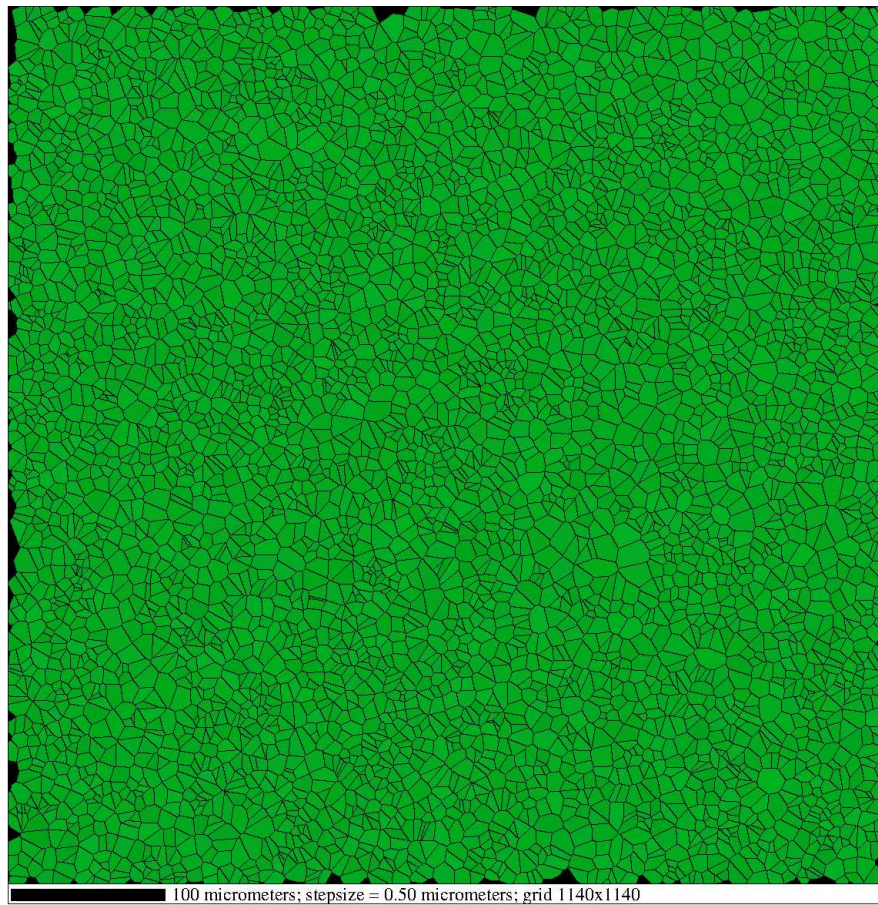


Figure 5.5: Starting microstructure for Brass oriented crystals - 5000 subgrains, periodic boundary conditions, mean subgrain size of $5 \mu\text{m}$, and with a uniform orientation spread of at most 4° from the principal Brass orientation. The subgrain boundaries, shown by the black lines, correspond to boundaries between regions having a disorientation of 0.1° or more.

5. SIMULATION OF SUBGRAIN GROWTH

their centroids lying in one band, and the other pool for the other cells. The resulting microstructure is presented in Figure 5.6.

5.4 Influence of crystallographic orientation on recovery

5.4.1 Brass orientation

The microstructure resulting from the simulation of annealing at 264°C for 34 hours with the Brass oriented crystal is shown in Figure 5.7. It is seen that this microstructure is identical to the one in Figure 5.5. In other words, no subgrain growth is observed.

It should be noted here that at lower values of the activation energy Q , a little subgrain growth is observed. This is attributed to the equilibration of triple junctions. With the activation energy of $Q=136$ kJ/mol at 264°C, the microstructure did not evolve at all.

Since there is very little activity in this structure, the simulation proceeds very rapidly and was completed in approximately one hour.

5.4.2 Goss orientation

The microstructure evolved during the simulation with the Goss oriented crystal. The microstructure at $t = 4003$ s and $t = 34$ hours are shown in Figure 5.8 and Figure 5.9 respectively. Similar to the experimental observations of Albou et al, there is significant subgrain growth. The mean grain area of the Brass and Goss microstructures are plotted against time in Figure 5.10.

Figure 5.8 and Figure 5.9 show that there is a lot of activity in the microstructure, namely movement of subgrain boundaries, topological operations for the disappearance of subgrains. Also, the subgrain boundaries have higher velocities which results in a smaller time step. Consequently, more iterations were required compared to the Brass simulations, to reach the same annealing time.

Therefore, the simulations took a much longer time than for the Brass crystal. This simulation required about 5 days on the same computer that carried out the Brass simulations. In other words, the Goss simulation was found to be 120 times slower than the Brass simulation.

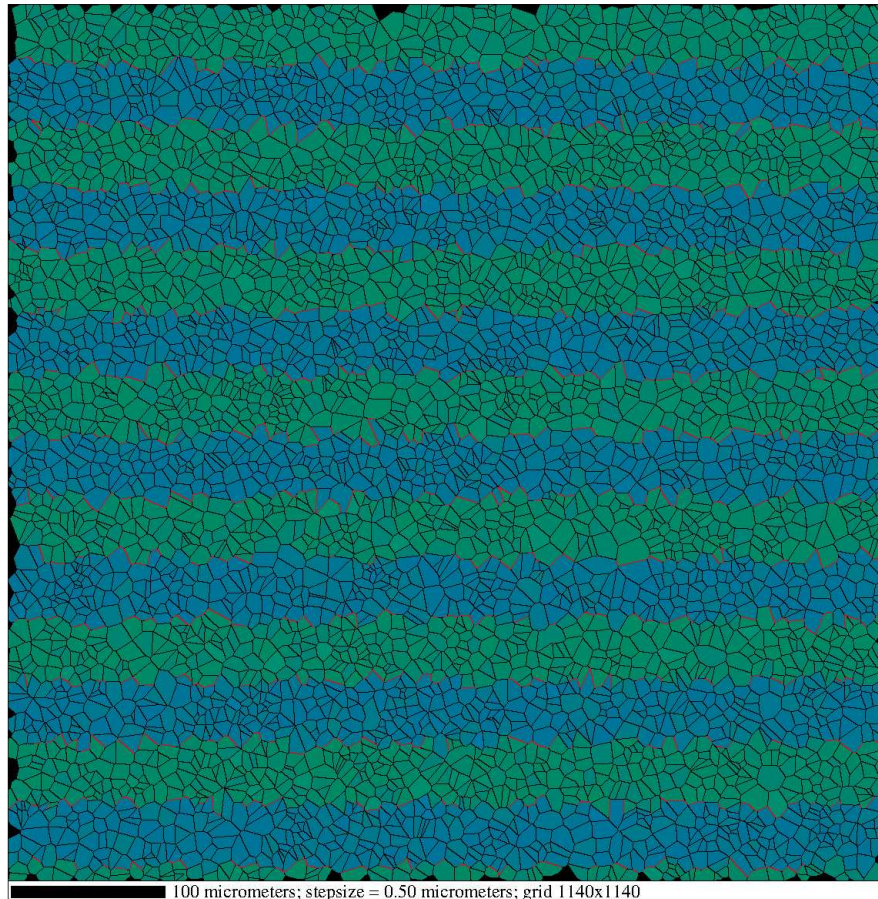


Figure 5.6: Starting microstructure for Goss oriented crystals - 5000 subgrains, periodic boundary conditions, mean subgrain size of $5 \mu\text{m}$, and with bands having orientations rotated from the principal Goss orientation around the axis normal to the rolling plane, and by an angle between $+5$ and $+10^\circ$ for one set of bands and an angle between -5 and -10° for the other set. The subgrain boundaries are shown by the black lines for boundaries between regions disoriented by at least 0.1° , and red lines for disorientations of at least 15° .

5. SIMULATION OF SUBGRAIN GROWTH

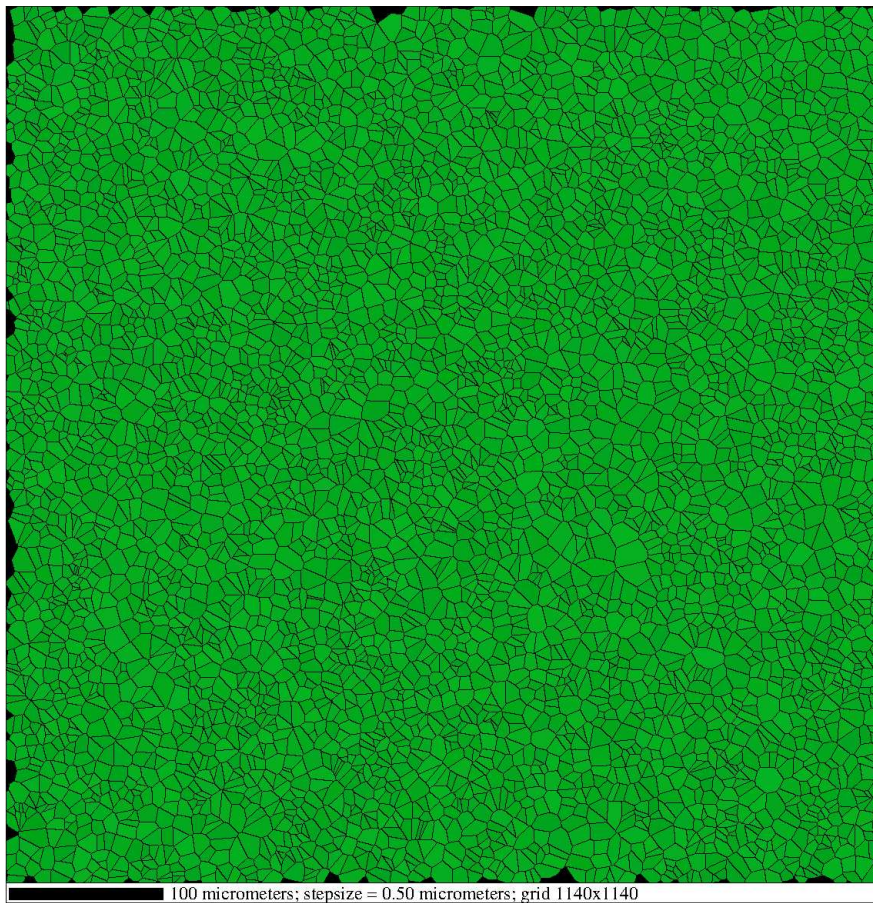


Figure 5.7: Brass microstructure after simulation of annealing at 264°C for $t = 34$ hours. No evolution is observed.

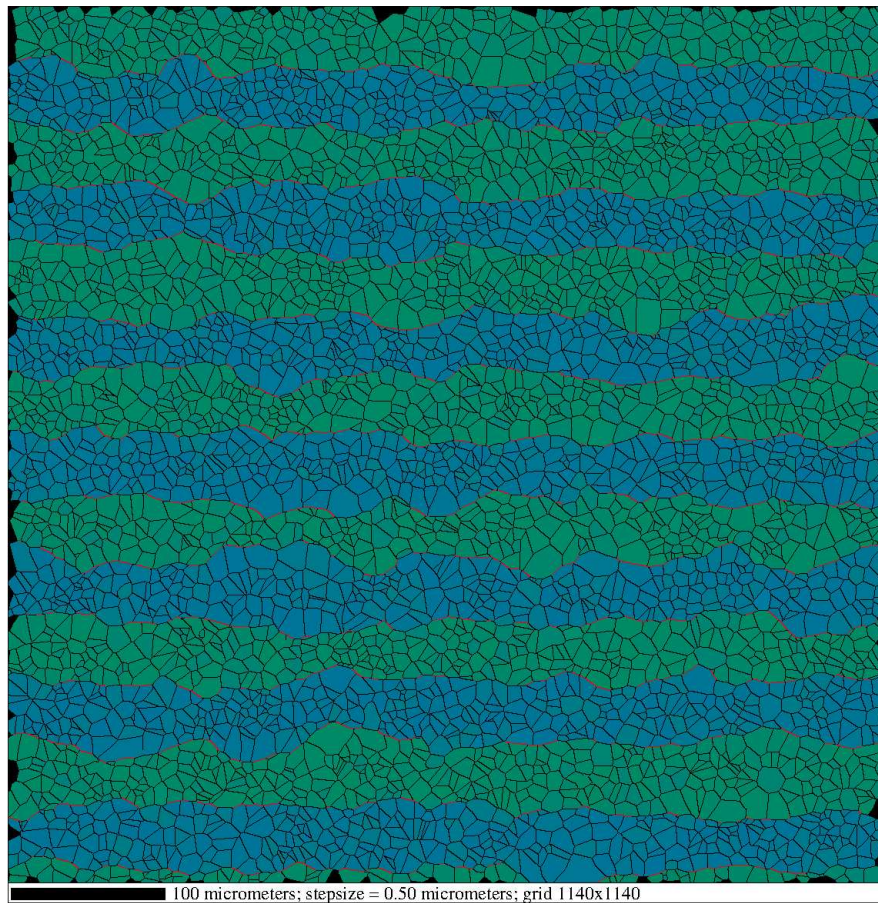


Figure 5.8: Goss microstructure after simulation of annealing at 264°C for $t = 4003$ s. Growth is observed in subgrains located at the interface between bands.

5. SIMULATION OF SUBGRAIN GROWTH

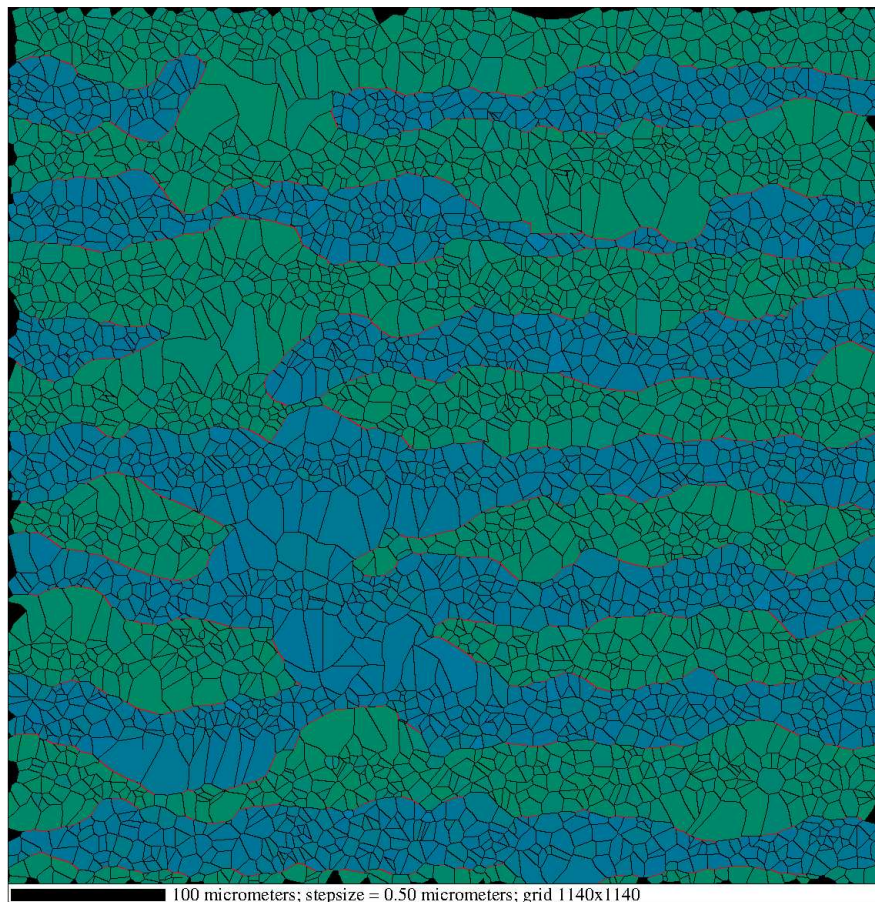


Figure 5.9: Goss microstructure after simulation of annealing at 264°C for 34 hours. Significant subgrain growth is observed. Some of the bands have grown through adjacent bands.

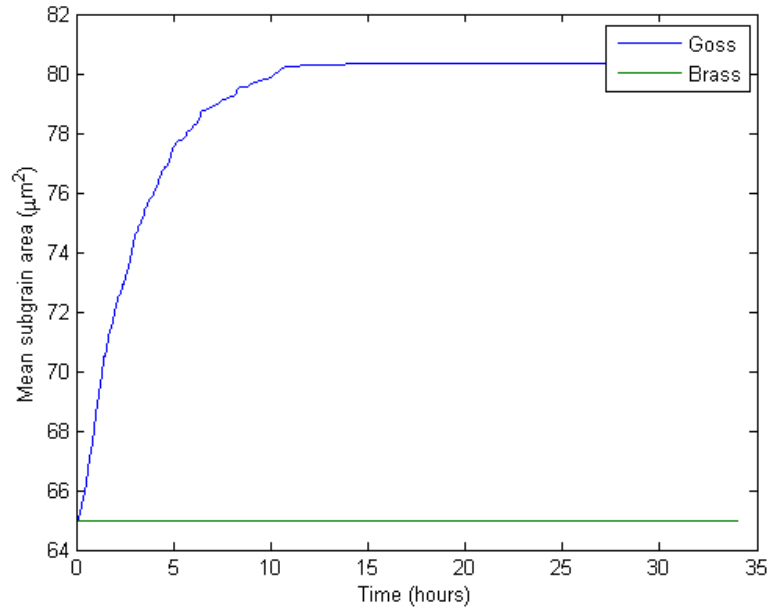


Figure 5.10: Mean subgrain area as a function of time in the Goss and Brass microstructures in the simulation of annealing at 264°C

5.5 Discussion

5.5.1 Rates of recovery in Brass and Goss oriented crystals

Comparing Figure 5.7 and Figure 5.9, and also from Figure 5.10, it is seen that the behaviour in the simulations is very similar to that in the experiments. The Brass structure shows little or no subgrain growth while the Goss structure evolves significantly.

In order to explain the reason for the difference in recovery behaviour, the differences between the two cases are listed:

1. Crystallographic orientation
2. Deformation microstructures

Crystallographic orientation has an effect on the resulting deformation microstructure, but no effect on the recovery kinetics because the orientation appears neither in the kinetic law equation nor in the equation for the migration velocity of subgrain boundaries.

5. SIMULATION OF SUBGRAIN GROWTH

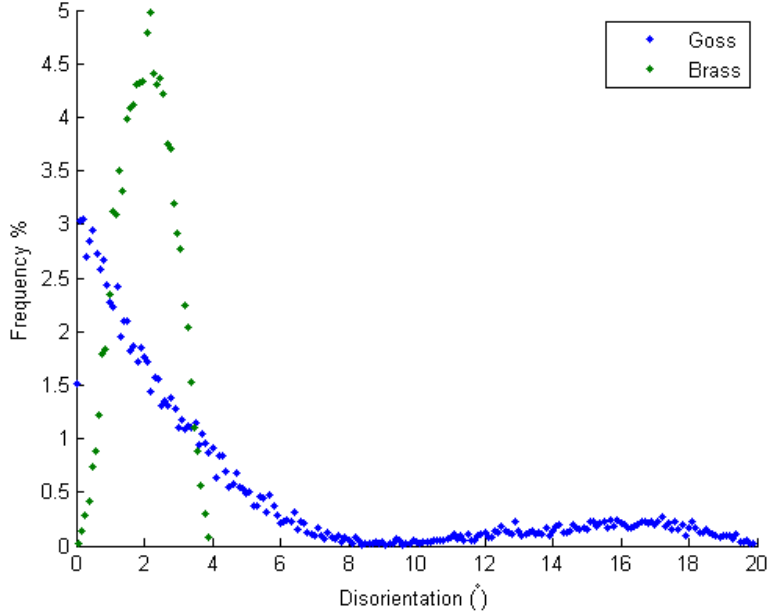


Figure 5.11: Initial disorientation distributions in the Goss and Brass microstructures

The difference in deformation microstructures - uniform distribution of orientations around the principal Brass orientation against bands rotated around the normal to the rolling plane for Goss - gives rise to very different disorientation distributions for the two cases. The disorientation distributions are presented in Figure 5.11.

Figure 5.11 shows that for the Brass structure we have all the sub-grain boundaries with disorientations between 2 and 4°. The Goss disorientation distribution is very different. There are many low-angle boundaries as in the case of Brass, but there are also a few subgrain boundaries having higher disorientation values going up to almost 20°. These boundaries are the ones lying at the interface between two bands.

From equation 5.1, we see that the disorientation angle has a large effect on the subgrain boundary mobility. Figure 5.12 shows the plot of the boundary mobility superimposed on the disorientation distributions. It is clearly seen that the exponential dependence of the mobility on disorientation causes an enormous difference between the mobilities of LAGBs and HAGBs. For example, a subgrain boundary with a disorientation of 1° has a mobility that is 5 orders of magnitude smaller than a boundary having a disorientation of 14°. Since the velocity of a subgrain boundary is directly proportional to the mobility (equation 5.3), the 1° boundary will thus migrate 10^5 times

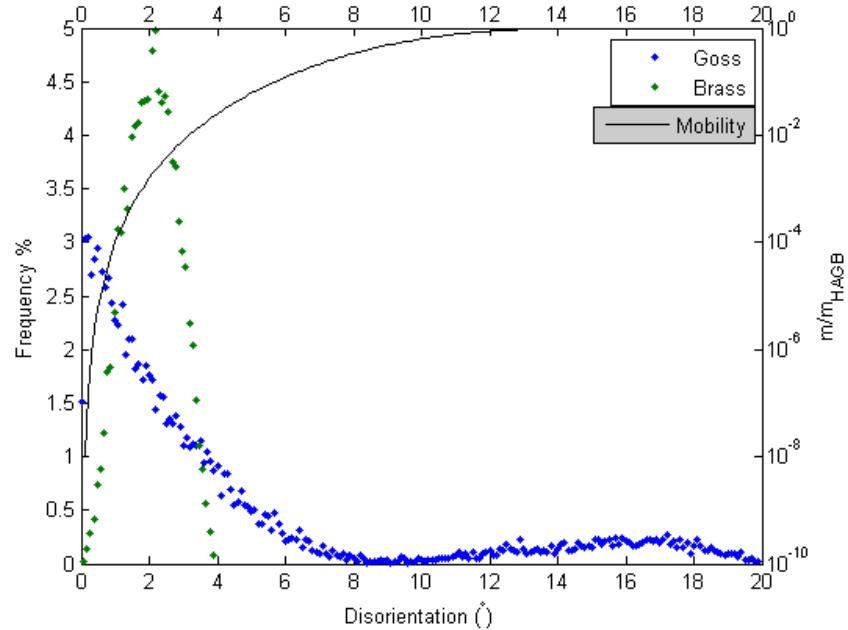


Figure 5.12: Disorientation distributions in Goss and Brass deformation microstructures with subgrain boundary mobility as a function of subgrain boundary disorientation

slower than the 14° boundary.

From the disorientation distributions in Figure 5.12 it is seen that all the subgrain boundaries in the Brass structure, and most of the subgrain boundaries in the Goss structure have extremely low mobilities, and thus very small migration velocities. The Goss structure possesses some subgrain boundaries that have higher disorientation values, and thus mobilities that are much higher compared to the majority of the subgrain boundaries. It is therefore these boundaries that migrate at higher velocities, and thus contribute to subgrain growth.

It is reported in the article by Albou et al. [6] that in the experiments the fraction of low-angle boundaries increases as recovery proceeds. This behaviour is also found in the simulations. The disorientation distributions at the beginning of the simulations and at the end of the simulation of annealing at 34 hours are shown in Figure 5.13. This shift is explained by the fact that the subgrain boundaries with high disorientations, in the range of 10 - 15° , have higher boundary energies according to the Read and Shockley equation. Therefore these boundaries have the highest driving force to be annealed out as this greatly reduces the internal energy of the metal. Indeed, in Figure 5.9, it is

5. SIMULATION OF SUBGRAIN GROWTH

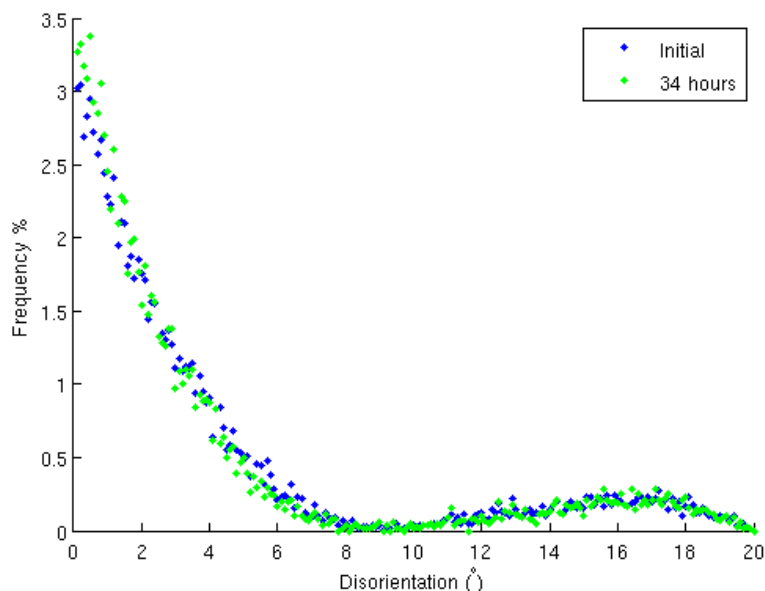


Figure 5.13: Change in disorientation distribution in the Goss microstructure. There is a slight increase in the fraction of low angle subgrain boundaries while the fraction of higher angle boundaries reduces.

observed that few subgrain boundaries with high disorientations remain, and a large number of subgrain boundaries with low disorientation appear within the bands.

The subgrain boundaries with higher disorientations, resulting from the banded deformation microstructure of the Goss crystals, are thus the reason for the high rate of recovery in Goss oriented crystals compared to the Brass oriented crystals.

5.5.2 Activation energy

It has been mentioned earlier that the activation energy of $Q = 190$ kJ/mol resulted in extremely small boundary values, which rendered the structures invariant in simulations representing annealing times of the order of 100 hours at the experimental temperatures of 264°C . In the simulations, a lower activation energy of $Q = 136$ kJ/mol was then used so that the boundaries may have larger migration velocities and thus evolve. A simple calculation shows that between the two activation energies mentioned above, the mobilities - and hence the migration velocities - are 6 orders of magnitude apart with the higher activation energy resulting in lower values. This indicates that the lack of

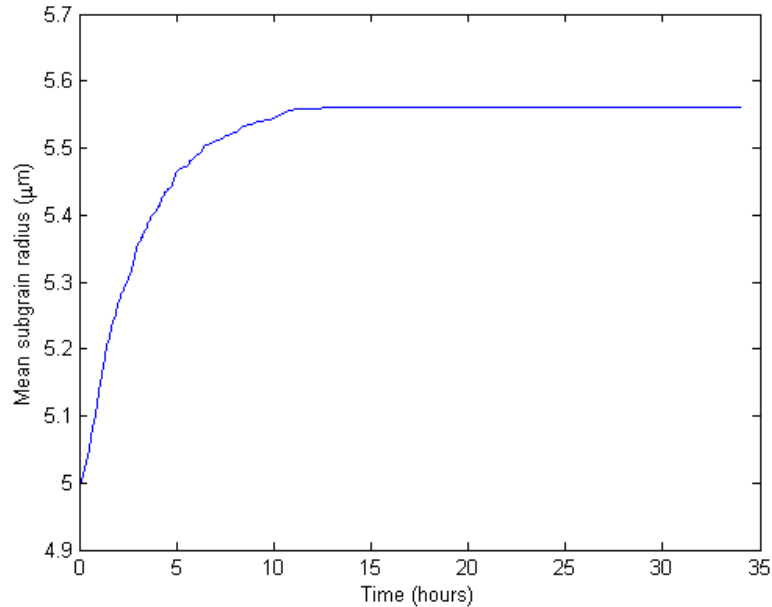


Figure 5.14: Mean subgrain radius in the Goss microstructure simulation plotted against time

microstructural evolution for $Q = 190$ kJ/mol is real and not an artefact due to errors in machine precision as may be suspected.

The lower activation energy may be due to the contribution of dislocation forests that remain. Humphreys and Hatherly [10] have mentioned that the different processes during recovery may take place concurrently. It is possible that these dislocation forests reduce the apparent activation energy as described by Vandermeer and Hansen [9].

5.5.3 Recovery kinetics

In Figure 5.10, it is seen that the rate of subgrain growth in Goss is higher than in Brass, but it slows down after about 12 hours of annealing at 264°C . The corresponding mean grain radius in the Goss crystal is plotted against time in Figure 5.14. The slowing down of recovery, as explained above, is attributed to the removal of the subgrain boundaries with high disorientation.

Using the mean subgrain radius data in the subgrain growth interval up to 10 hours plotted above, a fit of Burke and Turnbull's [14] power law was attempted to estimate the value of the exponent m . The power law is shown in equation 5.5.

5. SIMULATION OF SUBGRAIN GROWTH

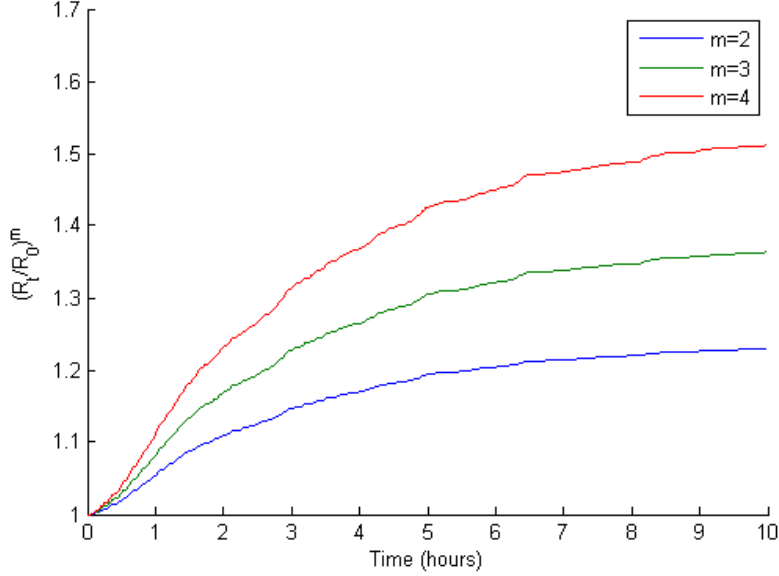


Figure 5.15: Mean subgrain radius in the Goss microstructure simulation plotted against time

$$R_t^m - R_0^m = \frac{M\gamma}{2}t \Rightarrow \left(\frac{R_t}{R_0}\right)^m = 1 + \frac{M\gamma}{2R_0^m}t \quad (5.5)$$

The graphs resulting from $m = 2, 3,$ and 4 are shown in Figure 5.15. A linear graph was not obtained for any of the values of m plotted in the figure, and higher values of m yielded curves that were even less linear. Therefore, it is concluded that power law kinetics are not followed during recovery.

Next, the recovery kinetics proposed by Nes [13] was fit to the simulation data. The data in Figure 5.14 was fit to equation 5.6, used by Barou et al. [3], with C and τ as fitting parameters.

$$\frac{R_0}{R_t} = 1 - C \ln\left(1 + \frac{t}{\tau}\right) \quad (5.6)$$

The result of the fitting is shown in Figure 5.16. A rather satisfactory fit is obtained and the parameters from equation 5.6 are found to be $C = 0.04 \pm 0.00014$ and $\tau = 2858 \pm 234$.

In the analysis by Barou et al, C was found to be 0.002. The higher value of C in the simulations is because of faster subgrain growth in the Goss structure. This is due

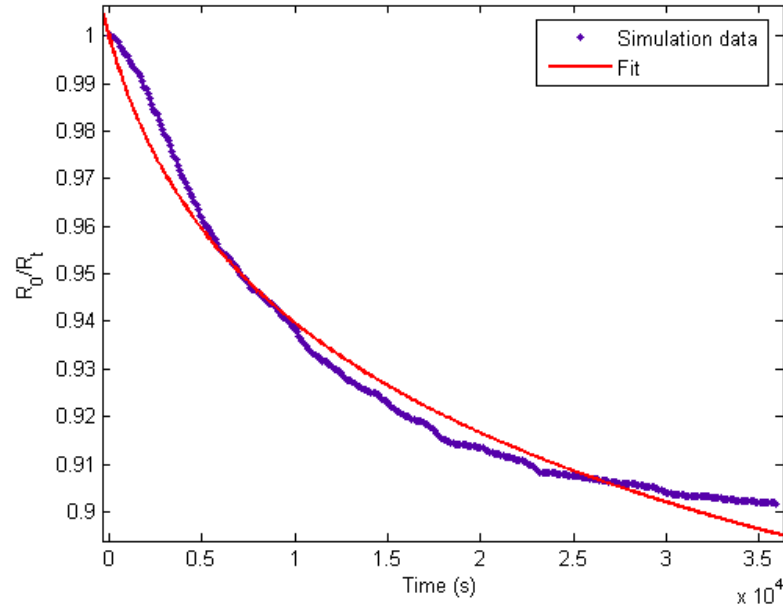


Figure 5.16: Fit of the simulation data to the recovery kinetics equation by Nes [13]

to the presence of certain subgrain boundaries of high disorientation. Taking the value of C from the simulations in the model for estimation of the activation energy would lead to a low value because of the fast growth.

Taking the values of C from Barou et al and τ estimated here, the corresponding activation energy is found to be 203 kJ/mol. This is higher than the energy of 136 kJ/mol provided in the simulations.

The quality of the data fitting shows that the equations for recovery kinetics proposed by Nes [13] is followed in the simulations and, as Barou et al. [3] have shown, in the experiments. However, the calculation of activation energy yields a value different from the one provided in the simulations. This shows that in order to model the kinetics of recovery in deformed single crystals, one must take into account the deformation microstructure with its disorientation distribution in addition to the factors like subgrain size.

5.6 Conclusions

Vertex dynamics simulations were carried out with deformation microstructures similar to those found in Brass and Goss oriented single crystals deformed in plane-strain compression in a channel-die up to a true strain of 2.3. Crystal plasticity simulations were used to verify the spread of orientations resulting from the deformation, and EBSD mapping from the experimental results of Albou et al. [6] were used to determine the spatial distribution of the orientations. Good agreement was obtained between the experimental and simulation results.

The low recovery rate in the Brass crystals is attributed to the presence of subgrain boundaries with low disorientations (at most 4°). The Goss deformation microstructure contains bands, at the interfaces of which there are subgrain boundaries with higher disorientations of $14\text{-}15^\circ$ and up to a maximum of 20° . The exponential dependence of boundary mobility on disorientation causes the boundaries with lower disorientation angles to have migration velocities 5 orders of magnitude lower than those with higher disorientation. This explains the high recovery rate in the deformed Goss crystals compared to the Brass crystals.

The recovery kinetics followed in the simulations was compared to the power law equation of Burke and Turnbull [14] and the kinetic equation proposed by Nes [13]. The power law was not followed by the recovery kinetics in the simulations. The kinetic equation by Nes was found to be more satisfactory but it failed to estimate the activation energy that was provided in the simulations. This demonstrated the need to include factors like disorientation in the development of recovery models if they are to be extended to more general application.

6

Conclusions

6.1 Summary

In Chapter 1, a survey of the current literature on the topic of recovery - the phenomenon, its kinetics, modelling and simulation - was presented. The experiments of Albou et al. [6] on deformed and annealed single crystals of an Al-0.1% Mn model alloy established that recovery rates differ significantly between different crystallographic orientations. They reported that Brass oriented deformed crystals showed no subgrain growth during recovery while Goss and S oriented deformed crystals exhibited subgrain growth and softening during recovery. It was suggested that the difference in recovery rates was the result of differences in the deformation microstructures and consequently the distribution of disorientations. The goal of this work was to investigate this suggestion with the help of simulations of subgrain growth with material parameters representing those of the alloy used. Kinetic laws for recovery have been proposed by Nes [13] and by Vandermeer and Hansen [9]. Nes' kinetic law is based on the subgrain size as the parameter indicating the progress of recovery while the kinetic law proposed by Vandermeer and Hansen involves the stored energy which is indicated by the microhardness of the sample. Accurate identification of subgrain sizes is rather difficult compared to microhardness measurements, which is the reason for the choice of the latter method for the analysis of recovery kinetics in this study. Regarding simulations of subgrain growth during recovery, no examples were found in the literature. It was thus decided to adapt methods that were used for the simulation of grain growth for the case of subgrain growth. Three types of simulations were considered - Vertex

6. CONCLUSIONS

dynamics, Monte Carlo Potts and Phase field. Finally the vertex dynamics simulations were selected because they were simpler to implement compared to the phase field approach, and unlike the Monte Carlo Potts model, vertex dynamics has a well-defined time step that relates directly to real annealing time.

Chapter 2 describes in detail the working of the vertex dynamics simulations. The chapter begins with a description of the Voronoi tessellation used for the generation of the microstructures which will be the input to the simulations. For this, the program `voronoi2d` was written using C++. The microstructures generated have periodic boundary conditions. The program can also generate microstructures representing rolled samples with elongated and flattened grains. Next, the equations for the vertex velocities in the simulation are explained. The velocity of a vertex depends on the mobility and energy of the boundary segment joining it to a neighbouring segment. Both the mobility and energy are taken to be functions of the boundary disorientation. Topological transformations that change the configuration of a boundary segment and which lead to the disappearance of subgrains are then described, followed by the calculation of the time step. All these were assembled to create the simulation program `networkConsole`, written in C++, for carrying out vertex dynamics simulations of subgrain growth in two dimensions. The inputs to the program are the starting microstructure generated using `voronoi2d`, the spatial distribution type of the orientations, and material properties such as mobility, energy and activation energy for recovery. The activation energy is required because in the expression for mobility, it is the term involving the activation energy that brings the dependence of mobility on temperature.

Chapter 3 contains a description of the techniques used in the experiments involving cold-rolling, annealing, and microhardness measurements. The experiments were carried out with the aim of characterizing the progress of recovery in terms of the microhardness of the samples annealed at different temperatures for different durations and subsequently use the model proposed by Vandermeer and Hansen to estimate the activation energy for recovery.

The results of the analysis of recovery kinetics to estimate the activation energy for recovery are presented in Chapter 4. A polycrystalline bar of the Al-0.1%Mn model alloy was deformed by cold rolling to a true strain of 3.96 - or 98% reduction - and then

annealed at four different temperatures for different durations. Microhardness measurements were carried out on these samples and these values were used in the recovery kinetics equation proposed by Vandermeer and Hansen in order to estimate the activation energy. To our knowledge, this work is the first example of the application of this kinetic law outside of the Technical University of Denmark, Risø. The value of activation energy obtained was quite unrealistic. It was also found that though the kinetic equation appears elegant and that the experiments require microhardness measurements that are simpler compared to the determination of subgrain sizes, there are certain practical difficulties when this method is to be applied. At high deformation, the sample sizes become very small. For example, in the present study, the samples were 380 μm thick on the ND-RD face, which was chosen for the microhardness measurements. Therefore, extreme care had to be taken to obtain sets of microhardness data with small standard deviations. The recovery kinetics equation contains exponential terms which amplify the effect of experimental uncertainty. In addition to the above, the equation has two unknowns and its complexity makes the problem impossible to solve analytically. A numerical approach is thus used which introduces further errors. Lastly, the equation assumes a constant scaling term which contributes to the increase in apparent activation energy as the energy stored in the metal is released by recovery. It appears from the analysis by Vandermeer and Hansen that this term is not a constant. In light of the above, it was decided to use the activation energy of 190 kJ/mol estimated by Barou et al. [3] in the vertex simulations which follow.

Chapter 5 presents the results of the vertex dynamics simulations. In our survey of existing literature on the subject, no other examples of the simulation of subgrain growth were found. Therefore, this application of vertex dynamics to simulate subgrain growth is the novel aspect of this work. Two of the three orientations reported by Albou et al. were selected - Brass and Goss - for the simulations. The deformation microstructures for the crystals of the two orientations were reproduced. The Brass microstructure consisted of subgrains with orientations distributed uniformly around the principal Brass orientation, and with a maximum disorientation of 4° . For the Goss orientation, a banded structure with subgrains rotated by an angle between $+5^\circ$ and $+10^\circ$ around the normal to the rolling plane for one set of bands, and by an angle between -5° and -10° for the other set. The disorientation ranges were verified by crystal plasticity simulations of plane-strain compression in a channel-die. The simulations

6. CONCLUSIONS

using the activation energy of 190 kJ/mol, found by Barou et al. [3], resulted in no microstructural evolution even after several hundred thousand iterations representing annealing durations of the order of 100 hours. This was because the mobilities of the subgrain boundaries, and hence the velocities of the vertices were almost zero. Next, a lower value of activation energy - 136 kJ/mol, reported by Lens et al. [35], was used, and this resulted in vertex velocities increased on an average by 10^5 at 264°C. This allowed the simulations to show some microstructural evolution. It was found that the results from the simulations were in good agreement with those from the experiments. The Brass simulation showed no subgrain growth while the Goss simulation showed significant grain growth. It was found that by creating the banded structure in the Goss microstructure, boundaries having high disorientation values in the range of 10° - 20° were introduced at the interface between two bands. The majority of the boundary disorientations remained in the same range for both Brass and Goss structures. The boundary mobility, being an exponential function of the disorientation, varies by 10^5 between boundaries of disorientations 1° and 14° . This rendered all of the subgrain boundaries in Brass and a large majority of the subgrain boundaries in Goss almost immobile. The subgrain boundaries at the interfaces of the bands in Goss, having higher disorientation values, had larger velocities, and they contributed to subgrain growth.

The simulations also showed behaviour similar to the experiments with respect to the evolution of the disorientation distribution. Evidently, the Brass crystal showed no change in disorientation distribution. The Goss crystal showed a rise in the fraction of subgrain boundaries with low disorientation angles. This is explained by the fact that the subgrain boundaries with higher disorientation also contribute more to the energy stored, and thus are more susceptible to be annealed out. In the simulations, their high mobilities and energies give high velocities to vertices lying on them, resulting in more growth of subgrains possessing such boundaries. Some of these subgrains grow while others disappear, and this causes the disorientation distribution in the simulations to follow the trend observed in the experiments. Indeed, when very few of the subgrain boundaries with high disorientation values remained, there was a marked decrease in the rate of subgrain growth in the simulation for the Goss crystal.

The results of the simulations showing the different rates of recovery were presented at the International Conference on the Texture of Materials (ICOTOM) 16 held at Mumbai, India [43].

Chapter 5 also presents an analysis of the recovery kinetics followed in the simulations based on two types of kinetic laws proposed in the literature - the power law kinetics by Burke and Turnbull [14], and the kinetic law by Nes [13] which involves the relative increase in subgrain size as the progress parameter for recovery. No match for the exponent was found for the power law kinetics. The kinetic law by Nes, on the other hand, yielded a very good fit with the curve representing mean subgrain radius with time. However, the activation energy estimated using this fit was found to be higher than the value provided as input to the simulations. It was concluded that in order to construct an accurate model of recovery in deformed single crystals, factors like the deformation microstructure and the disorientation distribution should also be considered.

6.2 Scope of future work

6.2.1 Microstructure

In the present simulations, the microstructure is generated using Voronoi tessellation. This method is widely accepted for the generation of microstructures, in both two and three dimensions. However, these structures are artificial. The simulations may be improved by the possibility of introducing real microstructures as input. This can be done by generating the input microstructure from the output of Subgrain Reconstruction Mapping (SRM), a method developed by Barou [2] for the accurate detection of subgrains in an EBSD mapping.

6.2.2 Alternative mobility and energy laws

The equations used in the simulation program for mobility and energy are functions of the boundary disorientation. There have been other studies that indicate that these two quantities depend on other factors such as the coincidence site lattice (CSL), the inclination and tilt of the boundaries, the axis of disorientation etc. Humphreys and Hatherly [10] have proposed an alternative mobility law for subgrain boundaries having very low disorientations. This law, and others, may be tested in the program for comparison with experimental results.

6. CONCLUSIONS

6.2.3 Parallel computing

The present simulations use a single processor at a time when executed. In light of the long time required for simulations in which vertices have large velocities and where there are frequent topological operations, parallelization of the program is an attractive option that might help reduce the total time of execution. This option was not explored during the thesis.

The parallelization may be achieved by distributing the velocity calculations and the displacement of vertices among the processors. This should not affect the results of the calculations as the velocities and positions required for them are those from the previous iteration. Parallelizing the topological operations will probably be more complicated. In any case, the parallelization of the velocity and vertex displacement should result in some acceleration of the execution of simulation program.

6.2.4 Kinetics of recovery

During this study, an analysis of recovery kinetics was attempted using the kinetic law proposed by Vandermeer and Hansen [9]. This approach was selected because it required relatively simple microhardness measurements for characterizing the progress of recovery. However, several practical difficulties, which have been described earlier in the document, arose when the method was applied and the final estimate of the activation energy for recovery was unsatisfactory.

Barou et al. [3] used the recovery kinetics proposed by Nes [13] and characterized the progress of recovery by the subgrain size. This method was more difficult and time-consuming compared to microhardness measurements, and being dependent on EBSD mapping of the samples, is also difficult to apply to severely deformed samples.

It might be insightful to estimate the activation energy for recovery in a deformed monocrystal, and thus reveal the influence of the distribution of disorientation, if any.

There is a need for the development of a method that would cover the shortcomings of both methods and allow for easy and precise modelling of the kinetics of recovery.

Appendices

Appendix A

Data Structures

This section presents details of the data structures used to represent entities such as vertices, grain boundaries, grains, and finally the polycrystal in the simulations. The description will begin with the smallest element - the vertex - and subsequently move to the larger elements.

The descriptions are given in the form of C++ class definitions. For the sake of brevity, the class definitions are limited to the most important data members and the occasional member function. Detailed documentation of the entire program is also available and can be obtained directly from the author.

A.1 Vertex

A vertex in the simulation is a point lying on a grain boundary or at a triple point. A vertex located at a triple point is connected to three other vertices and is called a *real* vertex, while one located on a grain boundary is connected to two others and is called a *virtual* vertex.

The data structure used to represent a vertex is the class called `Vertex2d`. The same class is used for both real and virtual vertices. It is defined as follows:

```
class Vertex2d
{
    // Time increment
    double dt;

    // Position vector
    Point2d p;
```

A. DATA STRUCTURES

```
// Velocity in previous iteration
Velocity2d v2t;

// Velocity in present iteration
Velocity2d v2tpdt;
}
```

An object of the class `Vertex2d` therefore stores its time increment, position and velocities from the present and previous iterations.

It will be shown later in the definition of the class `Network` that the simulation contains a global list of vertices stored in an array, with various data structures storing an integer index corresponding to the position of the required vertex in the array.

Each real vertex is a triple point, and the indices of the three grain boundaries are stored in an instance of the class `Connect`, which contains only the three indices. All the instances of the class `Connect` are stored in a global list, the ordering of which is identical to the global list of vertices. The virtual vertices are part of the grain boundary segments and are referenced by the data structure dealing with them.

A.2 Segment

The next higher entities in the simulations are the segments of a grain boundary. A segment is the straight line joining two vertices. Segments are represented by the class `Seg` which is defined as follows:

```
class Seg
{
    // Index of the vertex in the global vertex list
    int numV;

    // Periodic index for the segment
    int q;

    // Pointer to the previous segment on the grain boundary
    Seg* prior;

    // Pointer to the next segment on the grain boundary
    Seg* next;
}
```

The pointers `prior` and `next` give the location in memory of the previous and next segments on the grain boundary. For the first and last segments of a grain boundary, the pointers `prior` and `next` are set to `NULL`, respectively. This allows easy identification of the ends of a boundary.

Unlike the vertices, there is no global list of segments. This is because there is considerable reshuffling of the segments due to the topological operations. For each segment, space is reserved in memory and a pointer to its location is stored in the `prior` and `next` fields of its neighbours. Pointers to segments at the ends of a grain boundary are stored in the grain boundary class described in section A.3.

A.3 Grain Boundary

In the simulations, a grain boundary is discretized into several straight segments, each of which is represented by an object of type `Seg`. A grain boundary in the simulation is defined in the class `Bound` as follows:

```
class Bound
{
    // Integer index of the grain on one side
    int ig1;

    // Integer index of the grain on the other side
    int ig2;

    // Pointers to the first and last segments
    Seg* real[2];

    // Grain boundary disorientation
    double theta;

    // Grain boundary energy
    double energy;

    // Grain boundary mobility
    double mobility;

    // Iterations since the last topological operation
    int swit;
}
```

A. DATA STRUCTURES

An object of the type `Bound` thus stores indices of the grains on either side. These indices correspond to positions in a global list of grains that is maintained in the simulations. Pointers to the first and last segments allow quick bi-directional access to all the segments lying on this boundary.

From the orientations of the two grains indicated by `ig1` and `ig2`, the grain boundary disorientation `theta` is calculated. The quantities `energy` and `mobility` are obtained using the equations 2.6 and 2.7 respectively [12, 29].

The integer `swit` counts the number of iterations since the last topological operation. This is required in order to prevent segments from undergoing topological operations at every iteration as this may lead to flip-flop situations where a segment keeps oscillating between two unstable positions until an external influence changes the neighbourhood sufficiently for it to stop.

A global list of grain boundaries is maintained, and objects in this list are accessed using indices that correspond to their positions in the list.

A.4 List of grain boundaries

In the simulations, each grain is defined by a cyclic list of grain boundaries, and its orientation. The cyclic list is stored in objects of the class `Grain`, defined as follows:

```
class Grain
{
    // Index of the grain boundary in the global list
    int numGB;

    // Periodic index of the grain boundary
    int qGB;

    // Pointer to the previous grain boundary
    Grain* prior;

    // Pointer to the next grain boundary
    Grain* next;
}
```

The list of grain boundaries is cyclic, i.e., the pointers `prior` and `next` do not take the value `NULL` at any time.

Since each grain boundary is shared by two grains, it appears in two instances of objects of type **Grain**. For several operations, especially topological operations, it is necessary to be able to identify which side of the boundary one is on. For this, the member `numGB` takes a positive value in one grain and a negative value on the other. For example, consider the grain boundary at position 42 in the global grain boundary list. In one of the grains that contains this boundary, `numGB=42` while the in the other grain `numGB=-42`. This way, it easy to identify which side one is on while at the same time accessing the same grain boundary stored in memory using the absolute value of the index `numGB`.

A.5 Grain

A grain in the simulations is represented by the class **Polycrystal** defined as follows:

```
class Polycrystal
{
    // Integer index for this grain in the global grain list
    int index;

    // Euler angles (Bunge's notation) of the orientation
    double phi[3];

    // Pointer to the first grain boundary
    Grain* firstG;
}
```

Each grain is defined as a cyclic list of grain boundaries, and a certain crystallographic orientation. The first grain boundary is indicated by the pointer `firstG`.

A global list of grains is maintained, and the integer `index` indicates the position of each grain in this list.

A.6 Master class for the simulation

All data of the simulations reside within an instance of the master class called **Network**. This class contains many data fields and member functions. Only the most important ones are shown in its definition below:

```
class Network
{
```

A. DATA STRUCTURES

```
private:
// Total simulation time
double totalTime;

// Time increment in each iteration
double globalTimeIncrement;

// Pointer to the global list of polycrystals
Polycrystal* poly;

// Pointer to the global list of grain boundaries
Bound* GB;

// Pointer to the global list of vertices
Vertex2d* V;

// Pointer to the global list of connections
Connect* c;

public:
// Public member functions
// Initialize the simulation parameters
bool initializeParameters (char* parFileName);

// Initialize the microstructure
bool initStructure ();

// Start and manage the simulation
void startSimulation ();

private:
// Private member functions
// Calculate the vertex velocities
void velocities ();

// Calculate the time increment
double timeIncrement ();

// Check for topological operations and carry them out if necessary
void checkTopology ();

// Flip a short segment
// @param s0 Index of the segment to be flipped
```

```

// @param losePlus Index of the grain on the positive side
// @param loseMinus Index of the grain on the negative side
void flipSegment (int s0, int losePlus, int loseMinus);

// Eliminate a small triangular grain
// @param small3 Index of the triangular grain
void killTriangle (int small3);

// Eliminate a small lenticular grain
// @param small2 Index of the lenticular grain
void killLozenge (int small2);

// Move all the vertices
void moveAllTheNodes ();

// Treat the fast vertices
void treatTheFastMoving ();
}

```

When the program is launched, the parameters and microstructure are initialized by calls to the functions `initializeParameters ()` and `initStructure ()`. Once both these functions execute successfully, the function `startSimulation ()` is called, which starts the simulation and manages the iterations. The function calls within the iterations follow the flowchart in Figure 2.3 and are in the following order:

- `velocities ()`
- `timeIncrement ()`
- `moveAllTheNodes ()`
- `checkTopology ()`
- `treatTheFastMoving ()`

The velocities of the vertices are calculated using the equations given in section 2.3.3, and the time increment using the method described in section 2.3.5.2. The topological operations are briefly described in section 2.3.4; for more details, see Appendix B.

A. DATA STRUCTURES

Appendix B

Topological transformations

B.1 Introduction

In the vertex dynamics simulations, events like the disappearance of a small grain and the recombination of triple points are implemented through functions classed as *topological transformations*. These events are triggered when a grain boundary becomes shorter than the critical length e defined by equations 2.10-2.12.

There are three topological transformations defined in the vertex dynamics simulations corresponding to the following events:

- recombination of triple points
- disappearance of a triangular grain
- disappearance of a lenticular grain

These events are shown in Figure 2.8.

B.2 Checking for topological transformations

In the simulations, the function `checkTopology ()` is called in every iteration¹ to check the entire microstructure for topological transformations.

¹For details of the iterations, see Appendix A.

B. TOPOLOGICAL TRANSFORMATIONS

B.2.1 Marking grain boundaries for topological transformations

The function scans through the global list of grain boundaries (member `GB` in the class `Network`; see sections A.3 and A.6 for details). Grain boundaries containing virtual vertices are ignored because they are too long to undergo topological transformations. Grain boundaries that have undergone a topological operation less than 3 iterations ago are also ignored in order to prevent situations in which it keeps oscillating between two unstable positions. Of the remaining grain boundaries, those that are shorter than the critical length e are marked for topological transformations.

B.2.2 Identifying the topological transformations

Once a grain boundary is marked for a topological operation, the next step is to identify which of the three transformations is to be triggered. In order to do this, we need to know the number of sides in each of the two grains that are separated by the grain boundary. The values `ig1` and `ig2` indicate the two grains. Three possible cases are identified for the number of sides of each grain:

- $n = 2 \Rightarrow$ lenticular grain
- $n = 3 \Rightarrow$ triangular grain
- $n \geq 4 \Rightarrow$ other grain with at least one short boundary

The first two cases correspond to the elimination of a small grain, while the third one implies a recombination of triple points. The corresponding functions that are called are:

- `killLozenge (small12)`
- `killTriangle (small13)`
- `flipSegment (s0, losePlus, loseMinus)`

After carrying out each topological operation, the limiting length e is recalculated.

B.3 Removal of a lenticular grain

In order to remove a lenticular grain, the function `killLozenge` (`small2`) is called with the argument `small2` representing the index of the grain to be removed. What happens in this function is shown in Figure B.1. The grain to be removed is shown in blue.



Figure B.1: Removing a lenticular grain using the function `killLozenge`

Note that in the figure, the grain is drawn as a visible ellipse only for the purpose of clarity. In the simulations, such a grain is extremely small and the two grain boundaries PQ and QP are indistinguishable from each other. This is because as the boundary length becomes shorter than the critical length e , the virtual vertices on it are removed, thus making the boundary a straight line.

The sequence of events in the function is as follows:

1. Update values
 - (a) All virtual vertices are removed from the grain boundary AP .
 - (b) The grain boundary AP is modified to become AB .
 - (c) Virtual vertices are introduced on to the boundary AB .
 - (d) The pointers `prior` and `next` in the grain boundary lists of the larger grains on either side are updated so that the boundaries AB , PQ (or QP on the other side), and QB are replaced with the new boundary AB .
 - (e) Re-calculate the critical length.
2. Cleanup
 - (a) Remove the vertices P and Q from the global vertex list¹.

¹In order to avoid extensive re-indexing, no entry is actually removed from the global lists. Instead, the value of the removed entity or its neighbours is set such that it indicates the fact that it has been removed. For example, the position vector of a removed vertex is set to a value far outside the simulation box. For grain boundaries, the previous and next boundaries are made to point to each other in their `next` and `prior` pointers respectively, thus removing reference to the removed grain boundary. For grains, the pointer to the first grain boundary - `firstG` - is set to `NULL`.

B. TOPOLOGICAL TRANSFORMATIONS

- (b) Set the connection indices for the vertices P and Q to 0.
- (c) Delete the segments lying on the removed grain boundaries, and free the memory occupied by them¹.
- (d) Remove the small lenticular grain from the global list of grains.

B.4 Removal of a triangular grain

In order to remove a triangular grain, the function `killTriangle` (`small3`) is called with the argument `small3` representing the index of the grain to be removed. What happens in this function is shown in Figure B.2.

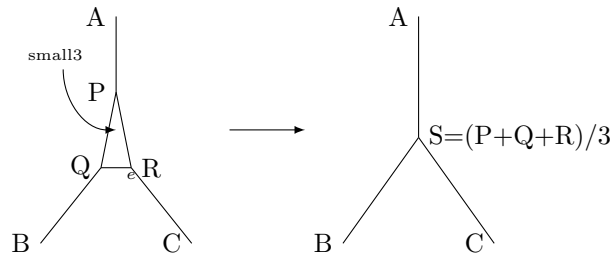


Figure B.2: Removing a triangular grain using the function `killTriangle`

The ΔPQR is the small triangular grain that is to be removed. It is replaced by a single vertex S , the position of which is simply the average of the position vectors of the three vertices P , Q and R . The sequence of events in the function is as follows:

1. Update values
 - (a) A new vertex S is created, the position of which is the average of the position vectors of the vertices P , Q and R .
 - (b) The grain boundaries AP , BQ and CR are modified to become AS , BS and CS , respectively.
 - (c) The `prior` and `next` in the grain boundary lists of the three neighbouring grains are updated to eliminate the boundaries PQ , QR and RP .

¹Segments are not maintained in a global list, so no re-indexing is necessary. Memory is allocated for them as required and the positions are referenced by pointers in the grain boundaries to which they belong. Once a grain boundary is removed, there is no need for its segments and their memory can be freed.

(d) Re-calculate the critical length.

2. Cleanup

(a) Remove the vertices P , Q and R from the global vertex list.

(b) Set the connection indices for the vertices P , Q and R to 0.

(c) Delete the segments lying on the removed grain boundaries, and free the memory occupied by them.

(d) Remove the small triangular grain from the global list of grains.

B.5 Recombination of triple points

The recombination of triple points is carried out when a grain boundary segment belonging to a grain with more than three sides becomes shorter than the critical length e . It is implemented by the function `flipSegment` (`s0`, `losePlus`, `loseMinus`) which accepts the grain boundary index `s0`, and the indices of the neighbouring grains `losePlus` and `loseMinus` as arguments.

The recombination is shown in Figure B.3.

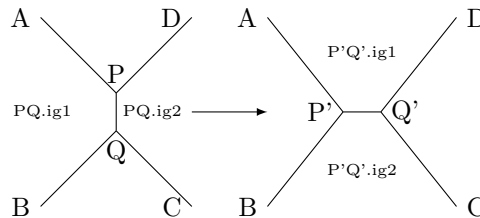


Figure B.3: Recombination of triple points using the function `flipSegment`

The sequence of steps in the function is as follows:

1. Update values

(a) Identify the vertices P and Q of the segment indicated by the argument `s0`.

(b) From the positions of P and Q , calculate the positions P' and Q' such that:

- $P'Q' = PQ$, and
- $P'Q'$ is the perpendicular bisector of PQ .

(c) Modify the grain boundaries by creating segments so that:

B. TOPOLOGICAL TRANSFORMATIONS

- $AP \rightarrow AP'$
 - $BQ \rightarrow BP'$
 - $CQ \rightarrow CQ'$
 - $DP \rightarrow DQ'$
- (d) Identify the grain that had the boundaries AP and PD , and assign it as a neighbour to the new boundary $P'Q'$.
- (e) Identify the grain that had the boundaries BQ and QC , and assign it as a neighbour to the new boundary $P'Q'$.
- (f) Modify the grain boundary lists of the grains `losePlus` and `loseMinus` (shown as $PQ.ig1$ and $PQ.ig2$ in Figure B.3) so that the new segments appear on them in the correct order.
- (g) Calculate the disorientation, mobility and energy of the new grain boundary $P'Q'$.
- (h) Re-calculate the critical length.
2. Cleanup
- (a) Update the connections for the vertices P' and Q' to the appropriate values.
- (b) Delete the segments that connected the old vertices P and Q , and free the memory occupied by them.

References

- [1] H G SCHWARZ. **Aluminum Production and Energy**. In C J CLEVELAND, editor, *Encyclopedia of Energy*, pages 81–95. Elsevier, New York, 2004. 1
- [2] F BAROU. *Étude de la croissance des sous-grains dans des alliages binaires aluminium manganèse*. PhD thesis, Ecole Nationale Supérieure des Mines de Saint-Etienne, 2009. 2, 12, 13, 53, 107
- [3] F BAROU, C MAURICE, J-M FEPPON, AND J H DRIVER. **Sub-Boundary Mobilities during Recovery of Binary Al-Mn Alloys**. *Materials Science Forum*, **715-716**:725–731, April 2012. 2, 29, 61, 75, 76, 79, 82, 100, 101, 105, 106, 108
- [4] Q XING, X HUANG, AND N HANSEN. **Recovery of Heavily Cold-Rolled Aluminum : Effect of Local Texture**. *Metallurgical and Materials Transactions A*, **37A**(April):1311–1322, 2006. 2, 13, 81
- [5] A ALBOU. *Influence de l'orientation cristalline sur les microstructures de déformation et l'adoucissement d'alliages Al-Mn*. PhD thesis, Ecole Nationale Supérieure des Mines de Saint-Etienne, 2010. 2, 53
- [6] A ALBOU, A BORBELY, C MAURICE, AND J H DRIVER. **Orientation-dependent recovery in strongly deformed Al0.1% Mn crystals**. *Philosophical Magazine*, **91**(31):3981–4000, November 2011. 2, 13, 14, 15, 29, 61, 75, 81, 83, 85, 97, 102, 103
- [7] C MAURICE AND F J HUMPHREYS. **2- and 3-D curvature driven vertex simulations of grain growth**. In H WEILAND, B L ADAMS, AND A D ROLLETT, editors, *Grain Growth in Polycrystalline Materials III*, pages 81–90, 1998. 3, 21

REFERENCES

- [8] D WEYGAND, Y BRÉCHET, AND J LÉPINOUX. **A vertex dynamics simulation of grain growth in two dimensions.** *Philosophical Magazine Part B*, **78**(4):329–352, October 1998. 3, 21, 34, 36, 42, 43, 45
- [9] R A VANDERMEER AND N HANSEN. **Recovery kinetics of nanostructured aluminum: Model and experiment.** *Acta Materialia*, **56**(19):5719–5727, November 2008. 3, 17, 18, 29, 61, 67, 72, 76, 77, 82, 99, 103, 108
- [10] F J HUMPHREYS AND M HATHERLY. *Recrystallization and Related Annealing Phenomena, 2nd Edition.* Elsevier, 2004. 5, 7, 8, 11, 16, 40, 42, 61, 78, 81, 99, 107
- [11] J P HIRTH AND J LOTHE. *Theory of dislocations.* John Wiley & Sons, 2nd ed. edition, 1982. 6
- [12] W T READ AND W SHOCKLEY. **Dislocation models of crystal grain boundaries.** *Physical Review*, **78**:275–289, 1950. 6, 39, 83, 114
- [13] E NES. **Recovery revisited.** *Acta Metallurgica et Materialia*, **43**(6):2189–2207, October 1995. 7, 10, 19, 75, 76, 82, 100, 101, 102, 103, 107, 108
- [14] J E BURKE AND D TURNBULL. **Recrystallization and grain growth.** *Progress in Metal Physics*, **3**:220–292, 1952. 13, 49, 99, 102, 107
- [15] Y HUANG, F J HUMPHREYS, AND M FERRY. **The annealing behaviour of deformed cube-oriented aluminium single crystals.** *Acta Materialia*, **48**(10):2543–2556, June 2000. 13
- [16] T FURU, R ORSUND, AND E NES. **Subgrain growth in heavily deformed Aluminium - Experimental investigation and modelling treatment.** *Acta Metallurgica et Materialia*, **43**(6):2209–2232, 1995. 17, 82
- [17] D KUHLMANN-WILSDORF, G MASING, AND J RAFFELSIEPER. **Zur theorie der erholung.** *Zeitschrift fur Metallkunde*, **40**:241–246, 1949. 17, 67
- [18] G BORELIUS, S BERGLUND, AND S SJOBERG. **Measurements on the evolution of heat during the recovery of cold-worked metals.** *Arkiv Fysik*, **6**:143–149, 1952. 17, 67

-
- [19] T YU. *Recovery and recrystallization of nanostructured metals - mechanisms and kinetics*. PhD thesis, Technical University of Denmark, 2011. 19, 68, 72, 76, 77, 78
- [20] Y HUANG AND F J HUMPHREYS. **Subgrain growth and low angle boundary mobility in aluminium crystals of orientation $\{110\}001$** . *Acta Materialia*, **48**(8):2017–2030, May 2000. 20
- [21] M A MIODOWNIK. **A review of microstructural computer models used to simulate grain growth and recrystallisation in aluminium alloys**. *Journal of Light Metals*, **2**(3):125–135, August 2002. 20, 21, 25
- [22] K KAWASAKI, T NAGAI, AND K NAKASHIMA. **Vertex models for two-dimensional grain growth**. *Philosophical Magazine Part B*, **60**(3):399–421, September 1989. 21, 34
- [23] D WEYGAND, Y BRÉCHET, J LÉPINOUX, AND W GUST. **Three-dimensional grain growth: A vertex dynamics simulation**. *Philosophical Magazine Part B*, **79**(5):703–716, May 1999. 21
- [24] L A BARRALES MORA. **2D vertex modeling for the simulation of grain growth and related phenomena**. *Mathematics and Computers in Simulation*, **80**(7):1411–1427, March 2010. 21, 22
- [25] L A BARRALES MORA, G GOTTSTEIN, AND L S SHVINDLERMAN. **Three-dimensional grain growth: Analytical approaches and computer simulations**. *Acta Materialia*, **56**(20):5915–5926, December 2008. 21, 22, 23
- [26] G COUTURIER. *Contribution à l'étude de la dynamique du Zener pinning: Simulations numériques par éléments finis*. PhD thesis, Ecole Nationale Supérieure des Mines de Saint-Etienne, 2003. 21, 22
- [27] G COUTURIER, C MAURICE, AND R FORTUNIER. **Three-dimensional finite-element simulation of Zener pinning dynamics**. *Philosophical Magazine*, **83**(30):3387–3405, 2003. 21
- [28] M FERRY AND F J HUMPHREYS. **Discontinuous subgrain growth in deformed and annealed $\{110\}001$; Aluminium single crystals**. *Acta Materialia*, **44**(4):1293–1308, 1996. 22

REFERENCES

- [29] F J HUMPHREYS. **A unified theory of recovery, recrystallization and grain growth, based on the stability and growth of cellular microstructuresI. The basic model.** *Acta Materialia*, **45**(10):4231–4240, October 1997. 22, 40, 114
- [30] D WEYGAND, M VERDIER, AND J LÉPINOUX. **Grain growth in Damascene interconnects.** *Modelling and Simulation in Materials Science and Engineering*, **17**(6):064005, September 2009. 22, 24
- [31] M A MIODOWNNIK, A CEREZO, AND J W MARTIN. **Mesoscale simulations of particle pinning.** *Philosophical Magazine A*, **79**:203, 1999. 25, 26
- [32] E FJELDBERG AND K MARTHINSEN. **A 3D Monte Carlo study of the effect of grain boundary anisotropy and particles on the size distribution of grains after recrystallisation and grain growth.** *Computational Materials Science*, **48**(2):267–281, April 2010. 25, 26
- [33] D FAN AND L-Q CHEN. **Computer simulation of grain growth using a continuum field model.** *Acta Materialia*, **45**(2):611–622, February 1997. 25, 27, 28
- [34] M BERNACKI, Y CHASTEL, T COUPEZ, AND R E LOGÉ. **Level set framework for the numerical modelling of primary recrystallization in polycrystalline materials.** *Scripta Materialia*, **58**(12):1129–1132, June 2008. 27
- [35] A LENS, C MAURICE, AND J H DRIVER. **Grain boundary mobilities during recrystallization of Al–Mn alloys as measured by in situ annealing experiments.** *Materials Science and Engineering A*, **403**:144–153, 2005. 29, 82, 83, 84, 106
- [36] R QUEY. **Orilib: A collection of routines for orientation manipulation,** 2008. 36
- [37] G GOTTSTEIN AND L S SHVINDLERMAN. *Grain Boundary Migration in Metals.* CRC Press, 1999. 39
- [38] D M KIRCH, E JANNOT, L A BARRALES MORA, AND G GOTTSTEIN. **Inclination dependence of grain boundary energy and its impact on the**

-
- faceting and kinetics of tilt grain boundaries in aluminum.** *Acta Materialia*, **56**(18):4998–5011, 2008. 39
- [39] M WINNING, A D ROLLETT, G GOTTSTEIN, D J J SROLOVITZ, A LIM, AND L S SHVINDLERMAN. **Mobility of low-angle grain boundaries in pure metals.** *Philosophical Magazine*, **90**(22):3107–3128, July 2010. 41
- [40] R QUEY. *Suivi de microtextures dans l'Aluminium en grande déformation à chaud.* PhD thesis, Ecole Nationale Supérieure des Mines de Saint-Etienne, 2009. 53, 54
- [41] V RANDLE. **Theoretical framework for electron backscatter diffraction.** In A J SCHWARTZ, M KUMAR, AND B L ADAMS, editors, *Electron backscatter diffraction in materials science*, pages 19–30. Kluwer Academic/Plenum Publishers, 2000. 59
- [42] S I WRIGHT. **Fundamentals of automated EBSD.** In A J SCHWARTZ, M KUMAR, AND B L ADAMS, editors, *Electron backscatter diffraction in materials science*, pages 51–64. Kluwer Academic/Plenum Publishers, 2000. 60
- [43] A MAJUMDAR, C MAURICE, AND J H DRIVER. **Vertex dynamics simulations of orientation dependent recovery in deformed Aluminium single crystals.** *Materials Science Forum*, **703**:639–642, 2012. 106

NNT : 2013 EMSE 0689

Adhish MAJUMDAR

SIMULATIONS VERTEX DE LA CROISSANCE DE SOUS-GRAINS DANS
L'ALLIAGE BINAIRE AL-0,1%Mn : EFFET DE L'ORIENTATION
CRISTALLOGRAPHIQUE

Spécialité: Sciences et génie des matériaux

Mots clefs : Aluminium, restauration, croissance des sous-grains, vertex dynamics, simulations, cinétique de la restauration

Résumé :

Le but de ce travail est d'utiliser les simulations du type « vertex dynamics » afin d'étudier l'effet de l'orientation cristallographique sur la cinétique de restauration d'alliage binaire Al-0,1%Mn.

La caractérisation de la cinétique de restauration d'un polycristal déformé par laminage à froid a été faite à l'aide de mesures de microdureté sur les échantillons recuits à quatre températures pendant différentes durées. Le modèle de restauration, développé par Vandermeer et Hansen a été appliqué pour estimer l'énergie d'activation de la restauration. Plusieurs problèmes ont été rencontrés pendant l'application du modèle, à cause de la complexité de ses équations, et également l'augmentation de l'incertitude des mesures expérimentales par les termes exponentiels qui figurent dans le modèle.

Les simulations de la croissance des sous-grains ont été faites avec les propriétés du matériau trouvées dans la littérature. Les microstructures de déformation des monocristaux orientés Brass et Goss ont été reproduites dans les simulations. Les résultats des simulations sont en bon accord avec les résultats expérimentaux d'Albou et al. Le faible taux de la croissance des sous-grains dans la microstructure Brass s'explique par la présence des sous-joints de faible désorientation. La microstructure Goss contient des bandes avec des sous-joints de fortes désorientations, et en conséquent, fortes mobilités, qui entraînent la croissance des sous-grains dans cette structure. Ainsi, il a été établi que l'orientation cristallographique influence la microstructure de déformation, et donc la distribution des désorientations des sous-joints.

NNT : 2013 EMSE 0689

Adhish MAJUMDAR

VERTEX DYNAMICS SIMULATIONS OF SUBGRAIN GROWTH IN
AL-0.1%Mn BINARY ALLOYS : EFFECT OF CRYSTALLOGRAPHIC
ORIENTATION

Speciality : Materials Science

Keywords : Aluminium, recovery, subgrain growth, vertex dynamics, simulation, kinetics of recovery

Abstract :

The present study aims to investigate the effect of crystallographic orientation on the kinetics of recovery in deformed samples of the Al-0.1%Mn binary alloy using vertex dynamics simulations of subgrain growth.

In order to characterize the recovery kinetics experimentally, a polycrystalline bar of the alloy was cold rolled to a true strain of 3.96. Samples extracted from the rolled bar were subjected to isothermal annealing at four temperatures for different durations. Microhardness measurements were made on each sample and the activation energy for recovery was estimated using these measurements and the recovery kinetics model developed by Vandermeer and Hansen. Several practical difficulties were encountered when using this model, most notably due to the complexity of the model equations and the amplification of experimental uncertainty by exponential functions in the model. The activation energy found was therefore not reliable.

Using the material properties mentioned in the literature, vertex dynamics simulations of subgrain growth were carried out. Deformation microstructures of monocrystals having Brass and Goss orientations were reproduced in the simulations. Good agreement with the experimental results of Albou et al. was achieved. The low rate of recovery in Brass crystals was due to the presence of subgrain boundaries of low disorientations. The Goss deformation microstructure consists of bands with subgrain boundaries of high disorientations which lead to high mobilities boundaries and this led to subgrain growth in the Goss crystal. Thus the effect of crystallographic orientation is related to the deformation microstructure, the subgrain boundaries and the distribution of their disorientations.